

**Development of a nanomechanical biosensor
integrated with an optical interferometric transducer**

(光干渉トランスデューサを融合したナノメカニカルバイオセンサの開発)

January 2021

Doctor of Philosophy (Engineering)

Toshiaki Takahashi

高橋 利昌

Toyohashi University of Technology

Date of Submission (month, day, year): January 8th, 2021

Department of Electrical and Electronic Information Engineering		Student ID Number	D143242	Supervisors	Kazuaki Sawada
Applicant's name	Toshiaki Takahashi				Kazuhiro Takahashi

Abstract (Doctor)

Title of Thesis	Development of a nanomechanical biosensor integrated with an optical interferometric transducer
-----------------	---

Approx. 800 words

When a human being is infected by viruses or cells are exposed to stress, various molecules are released as a molecular pattern from the lesion site to the dendrites and macrophages, and their concentrations gradually change. The comprehensive detection of these biomarkers would enable patients with brain dysfunction and infections to be treated appropriately according to the progression of the disease and the probability of mortality and sequelae would reduce. A sensor that can detect a variety of molecules, from small molecules to macromolecules, regardless of molecular size, should be developed to detect these molecular patterns. Although various conventional semiconductor sensors have been developed, a sensor which can comprehensively detect molecules of various sizes in a biological environment without extending the Debye length has not been realized. The micro-electro-mechanical system (MEMS) optical interferometric surface-stress sensor proposed by our laboratory can comprehensively detect low-concentration and small molecules, which have been difficult to detect using conventional surface-stress sensors, as well as macromolecules exceeding the Debye length by optimizing the wavelength selectivity and geometry parameters of the interferometer. Therefore, for a highly sensitive detection of target molecules of various sizes, interferometers with metal half-mirror and cavity-sealed structures with optimized geometry parameters, which can improve the detection performance of the sensor, were fabricated and bio-interfaces for adsorbing molecules on the sensor were constructed. Through the above tasks, this thesis presents the development of the sensor for a label-free and comprehensive detection of proteins and neurotransmitters in liquids and gas molecules in air.

First, the MEMS interferometer with metal half-mirrors structure was studied. Assuming this device is used for blood inspection, Au was selected as the half-mirror material because it has a superior transparent characteristic in the near-infrared wavelength region, where the absorption coefficient of blood components is small. Subsequently, we fabricated a MEMS interferometer with Au half-mirrors and constructed a bio-interface onto the interferometer to immobilize the albumin antibodies. The chip was immersed in the solution and the response of the sensor was obtained when the sample containing the albumin antigen molecule was added at a final concentration of 10 ng/mL and when other proteins were added. As a result, only the former exhibited the deflection of the membrane, suggesting the possibility of selective detection of macromolecular proteins using the antigen-antibody reactions. Based on the results of this study, our research group constructed a MEMS interferometer with optimized geometry parameters and evaluated the concentration dependence and limit of detection (LOD) for macromolecular proteins. The results indicated that the sensor reacted in a low concentration range of 100 ag/mL-1 ng/mL, and the LOD was observed to be 100 ag/mL-1 fg/mL. The results indicated that this is the most sensitive detection of macromolecular proteins in label-free semiconductor biosensors.

In the early interferometers with metallic half-mirrors structure, the sealing of the interferometer was incomplete because of the constraints of the fabrication process. Therefore, a new interferometer with a cavity-sealed structure was studied. Considering the application of this sensor to the detection of both proteins in liquids and gas molecules, we proposed to use the polymeric material used as the

molecular adsorption layer of the proteins as a gas-reactive layer. Optical and finite element analyses of the newly proposed sensor were performed and an interferometer with optimized various parameters was fabricated. Subsequently, a polymer that functioned as a gas-reactive film was deposited on the interferometer, and the concentration dependence and minimum detection limits for volatile ethanol were evaluated. We observed that the linear response was acquired in the concentration range of 5–110 ppm, and the LOD was 5 ppm. The result indicates that the sensitivity of the sensor was comparable to semiconductor-based sensors, which have the highest sensitivity for measuring ethanol at room temperature; this suggested the feasibility of the sensor that can detect ethanol concentrations of sub-ppm by optimizing the geometry parameters of the interferometer.

Finally, to demonstrate the detectability of small molecules in the liquid, we studied the use of a molecularly imprinted polymer (MIP) as a molecular adsorption layer that can adsorb neurotransmitters. Considering the integration with the sensor, we used electrochemical polymerization to enable the selective formation of the MIP with the template of dopamine (DA), which is well known as a neurotransmitter, on a conductive material in liquid, and formed the MIP film. Subsequently, the sensor was immersed in phosphate buffered saline (PBS) and the time course of the reflection spectrum was acquired when the DA was added into PBS to bring the final concentration to 1 μM . As a result, the deformation of the deformable membrane was observed only in the presence of DA, and the spectral response owing to the adsorption of DA was acquired, suggesting the feasibility of detecting neurotransmitters.

In this study, we realized the label-free detection of proteins and neurotransmitters in liquids and gas molecules in air using the proposed sensor and demonstrated the feasibility of a sensor that can detect molecules of various sizes. We expect that the realization of the device that has no restriction on the size of detectable molecules and can measure the adsorption process of target molecules in real-time will become an innovative basic technology in medical research.

Contents

Chapter 1. Introduction	1
1.1 The importance of biomolecular detection in disease diagnosis	1
1.2 Methods used for biomolecular analysis	3
1.2.1 High performance liquid chromatography	3
1.2.2 Enzyme-linked immuno-sorbent assay	5
1.3 Label-free biosensors using ELISA	7
1.3.1 Quartz crystal microbalance	7
1.3.2 Surface plasmon resonance	8
1.3.3 Field effect transistor	11
1.3.4 Surface stress sensor	14
1.3.4.1 Optical type	15
1.3.4.2 Capacitive type	17
1.3.4.3 Piezoresistive type	18
1.3.4.4 Optical interferometric type	22
1.4 Current status and challenges of biosensors in biomarker detection	26
1.5 Factors determining the deflection amount of the deformable membrane in optical interferometric surface stress sensor	27
1.6 Factors determining the limit of detection in optical interferometric surface stress sensor	28
1.7 Proposal for improvement of wavelength selectivity by metal half-mirrors structure	31
1.8 Purpose of this study	34
1.9 Outline	34
Chapter 2. Investigation of metal half-mirrors structure for MEMS interferometer with high wavelength selectivity	37
2.1 Preface	37
2.2 Aiming for detection of macromolecular biomarker	37
2.3 Design of the MEMS interferometer	39
2.3.1 Optical design	39
2.3.2 Mechanical simulation	41
2.3.3 Analysis of transmittance change to deflection of deformable membrane in liquid.	43

2.4	Fabrication procedure	45
2.5	Fabrication Results	50
2.5.1	Structure and geometry evaluation	50
2.5.2	Evaluation of wavelength selectivity	51
2.5.3	Impact of change in temperature	54
2.6	Conclusion	55
Chapter 3.	Acquisition of sensor response for detecting proteins in liquid ..	56
3.1	Preface	56
3.2	Consulting bio-interface onto top Au mirror	56
3.2.1	Molecule modification method using self-assembled monolayer	56
3.2.2	Formation of SAM and evaluation of surface condition of sensor	58
3.3	Acquisition of the response by antigen–antibody reaction	61
3.3.1	Evaluation of deflection amount by spectroscopic measurement	61
3.3.2	Selective detection of antigen molecule	64
3.4	Acquisition of sensor output in the cavity-sealed MEMS interferometer with high surface stress sensitivity.	66
3.4.1	Antibody molecules immobilization onto sensor.....	66
3.4.2	Selectivity of sensor.....	67
3.4.3	Concentration dependence and limit of detection	68
3.5	Conclusion	70
Chapter 4.	Investigation of cavity-sealed MEMS interferometer with high surface stress sensitivity	71
4.1	Preface	71
4.2	Aiming for the detection of volatile organic compounds in the breath.....	71
4.3	Design of the MEMS interferometer	74
4.3.1	Analysis of the spectral shift associated with deflection of deformable membrane	75
4.3.2	Analysis of surface stress sensitivity of deformable membrane	75
4.4	Fabrication procedure	77
4.5	Fabrication result.....	79
4.6	Conclusion	80

Chapter 5. Acquisition of sensor response for detecting gas molecules in the air	81
5.1 Preface	81
5.2 Improvement of spectral response by narrowing the air gap length of the interferometer.....	81
5.3 Impact of changes in relative humidity and temperature.....	85
5.4 Concentration dependence and LOD	86
5.5 Improvement of LOD by optimizing geometry parameters	88
5.6 Conclusion	90
Chapter 6. Neurotransmitter detection by MEMS interferometer with molecularly imprinted polymer	91
6.1 Preface	91
6.2 Aiming for the detection of neurotransmitters.....	91
6.3 Introduction of molecularly imprinted polymers.....	93
6.4 Fabrication procedure	94
6.5 Fabrication results	96
6.6 Acquisition of sensor response to neurotransmitter	97
6.7 Conclusion	101
Chapter 7. Overall conclusion	102
7.1 Summary.....	102
7.2 Prospects	105
References	107
Acknowledgements	115
List of Publications & Awards.....	116
Appendix A Process chart for MEMS interferometer with Au half-mirrors	119
Appendix B Process chart for cavity-sealed MEMS interferometer with gas reactive-layer	127
Appendix C Process chart cavity-sealed MEMS interferometer with a molecular imprinted polymer film	130
Appendix D Python program for smoothing spectra data	134
Appendix E Python program for extraction of Q points from spectra data	141
Appendix F Python program for smoothing Raman spectrum data	145

Chapter 1. Introduction

1.1 Importance of biomolecular detection in disease diagnosis

Because of recent advances in medical technology, lower mortality rates, and longer life expectancy, the population of seniors aged 65 and older in Japan is expected to increase rapidly to 37.16 million, or approximately 30% of the total population, by 2030 according to estimates by the National Institute of Population and Social Security Research [1]. According to the Ministry of Finance's social security budget allocation for the 2020 fiscal year, medical care expenditure was 12,154.6 billion yen, equivalent to approximately 34% of the total budget, which continues to increase each year with a rapidly ageing society. Diseases must be detected early before they become critical to reduce ever-increasing health care costs. Considering cancer as an example, which accounts for approximately 30% of deaths in Japan, the five-year survival rate for stage 1 colorectal cancer is 97.7%, whereas the rate for stage 4 colorectal cancer decreases to 43.9%. Similarly, for lung cancer, the rate is 87.3% in stage 1 conditions, but is known to decrease to 17.7% in stage 4 [2]. Therefore, the early detection of a condition before it becomes severe is essential to reducing health care costs. However, since the early stages of cancer onset do not exhibit subjective symptoms, detecting it at an early stage is often difficult because it is often only discovered after a physical condition is noticed.

The blood concentration of biomolecules, which increase because of certain diseases contained in the blood, can be measured as an index to identify the existence and degree of progression of various diseases at an earlier stage. The biomolecules related to these diseases are called biomarkers, and if these biomarkers can be detected from a minimal trace of specimens without labelling, diseases can be diagnosed easily, rapidly, and inexpensively in areas with few medical staff and small clinics. The demand for such point-of-care testing (POCT) devices is escalating, and since the global market for POCT devices is expected to increase to 46.7 billion dollars by 2024 [3], such device development has been attracting increasing interest.

When a human being is infected with viruses or cells are exposed to stress, various molecules are released as a molecular pattern from the lesion site to the dendrites and macrophages (Fig. 1.1), and their concentrations gradually change [4]. Therefore, the comprehensive detection of these biomarkers would enable

patients with brain dysfunctions and infections to be treated appropriately with the progression of the disease and the probability of mortality and sequelae would be reduced. A sensor that can detect molecules of various sizes should be developed to detect these molecular patterns.

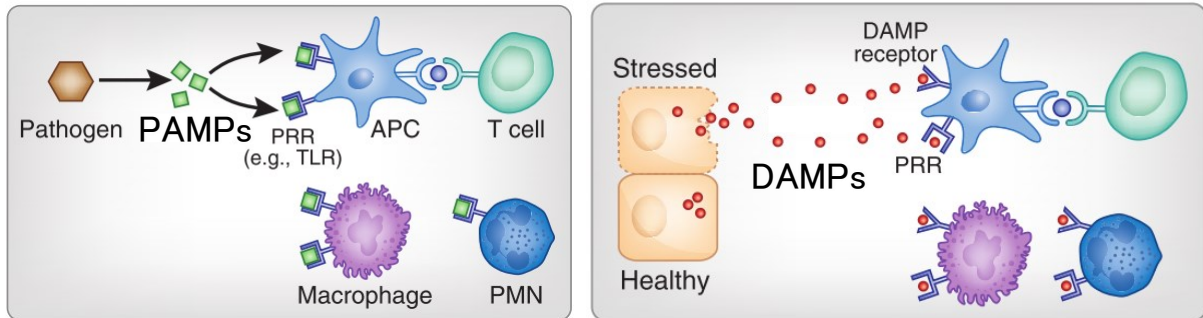


Figure 1.1: Schematic diagram of the molecular patterns released when a pathogen enters the body (left) and when cells are exposed to localized stress (right) [4]

1.2 Methods used for biomolecular analysis

Methods to detect target molecules in a sample by separating and analysing each component of a sample or by specifically adsorbing target molecules to a sensor have been devised. In this section, we introduce the common methods used to separate or adsorb target biomolecules from a sample.

1.2.1 High-performance liquid chromatography

High-performance liquid chromatography (HPLC) is an analytical method of identifying components in a sample based on the time response of the sample solution to component-by-component separation and the arrival of the sample at the detector. As shown in Fig. 1.2, an eluent is pumped through the pump at a constant flow rate. Additionally, a component separation layer of silica gel or synthetic resin packing material of a few μm to a few dozen μm in size, called a column, elutes the mixture containing the sample over time. Since a time lag exists between the eluted components reaching the detector (Fig. 1.3), the concentration of each component can be measured after separating the components contained in the sample by acquiring the time response of the component-derived signals. Common detectors include mass spectrometers that ionize the separated components to obtain the mass-to-charge ratio of the ionized components, ultraviolet (UV)/visible detectors that can measure substances with absorbing components in the UV region, and fluorescence detectors that detect the fluorescence produced by irradiating the sample with excitation light, etc. Additionally, the appropriate detector must be selected based on the analyte used. In 2018, according to a report, two diode array detectors and electrochemical detectors were incorporated into HPLC: tryptophan (TRP), an essential amino acid present in plasma, and kynurenic acid (KYA), which has been linked to several diseases such as cardiovascular disease, Alzheimer's disease, and dementia; they were detected at concentrations of 1–10 and 0.02–1 $\mu\text{g}/\text{mL}$, respectively, and their limits of detection (LODs) were reported to be 5 and 4 ng/mL , respectively [5]. While it has been widely studied as a high-performance analyser capable of detecting multiple target molecules, there are problems when detecting several types of molecules: the temporal resolution is reduced from a few minutes to several tens of minutes; the real-time response is lost; the appropriate eluent, column, and detector must be selected for each detection target; and the entire system is large and not portable.

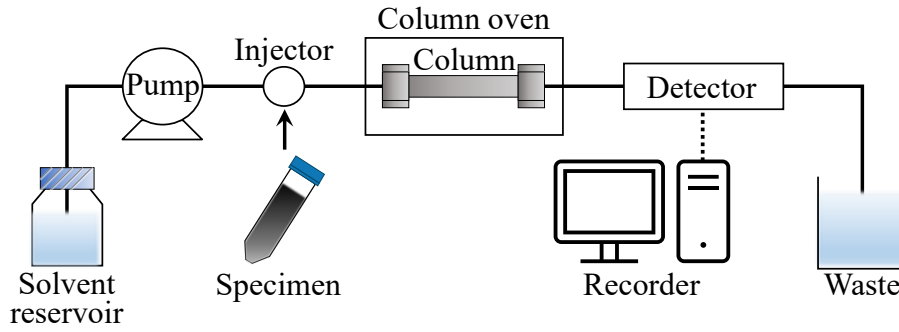


Figure 1.2: Schematic diagram of HPLC

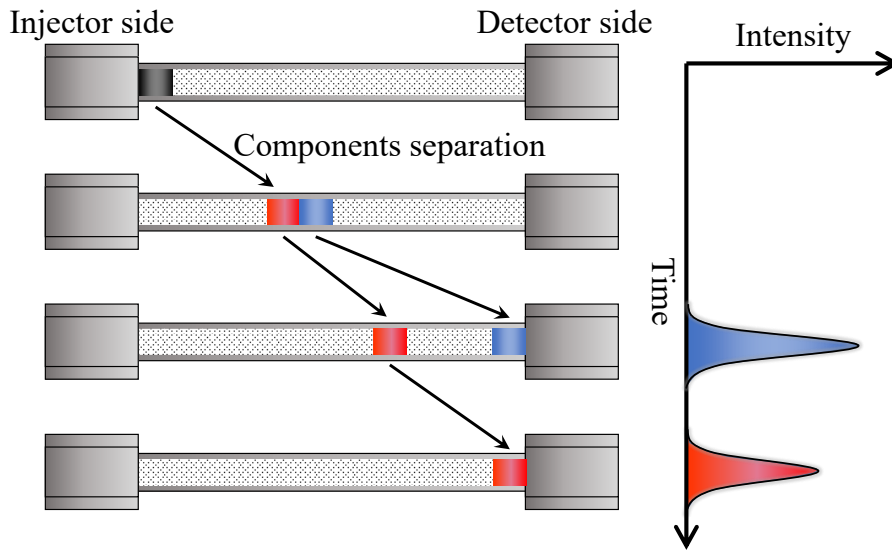


Figure 1.3: Schematic diagram of the time response of the components to be separated in a column. In a sample with two components mixed in, two signals of component origin are output in the time response waveform.

1.2.2 Enzyme-linked immuno-sorbent assay

The enzyme-linked immuno-sorbent assay (ELISA) is a technique to measure the absorbance of light produced by adsorbing enzyme-labelled antibodies to an antibody bound to an antigen molecule, and then a solution of chromogenic substrates (a substance that emits colour by reacting with an enzyme) is added. The most widely used technique to detect target molecules using the sandwich method is shown in Fig. 1.4. With this technique, the target molecules are bound to pre-immobilized antibody molecules on a well microplate and then adsorbed with secondary antibodies labelled with the enzyme. Dropping a solution containing the chromogenic substrate into this solution causes an enzymatic reaction, which changes the pigments of the chromogenic substrate. The concentration of the target molecule can be measured by the shading of this dye using an absorbance meter. The volume per chamber of a typical well microplate is approximately a few μL , and the target molecules that enter this chamber are measured. Therefore, lower concentrations of target molecules can be detected if the volume of the chamber is designed to be as narrow as possible to limit the number of molecules that can enter the chamber to a single molecule. This concept is called the digital ELISA the signal is counted as 1 when a colour change occurs in the chamber and 0 when it does not (Fig. 1.5). In the digital ELISA developed by Kim *et al.* at the University of Tokyo in 2012, in a device narrowing the volume per chamber to 1 fL (Fig. 1.6), the prostate specific antigen (PSA), a known biomarker for prostate cancer was successfully detected with a LOD of 60 ag/mL [6]. While the detector succeeded in detecting biomarkers with the highest sensitivity among existing biomarker detectors, it had several problems: a labelling agent had to be applied to many samples, a proficient technician was required during the detection process, the device was large and expensive, and the real-time response of adsorbed target molecules (adhesion process) could not be obtained.

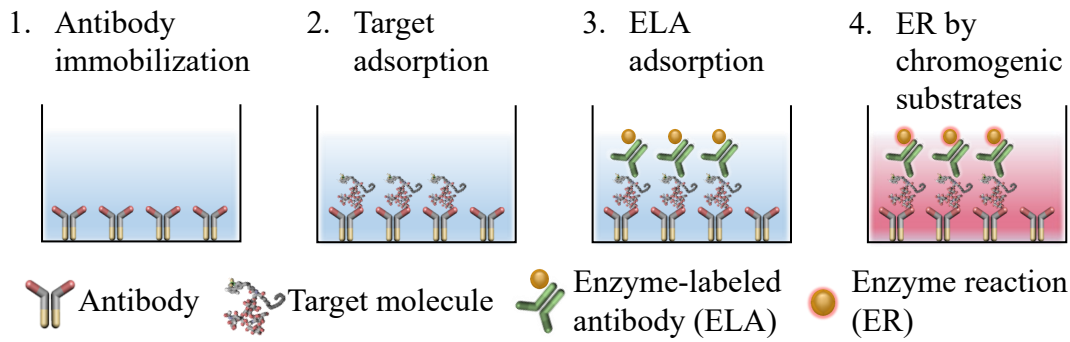


Figure 1.4: Detection principle of target molecules by ELISA. The figure shows a schematic diagram of the case using the sandwich method.

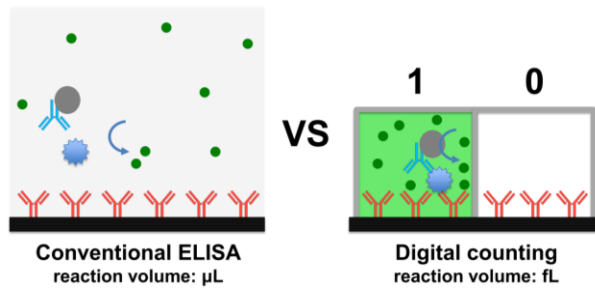


Figure 1.5: A digital ELISA concept that enables single-molecule detection by limiting the chamber volume of the well plate compared to conventional ELISA methods [7].

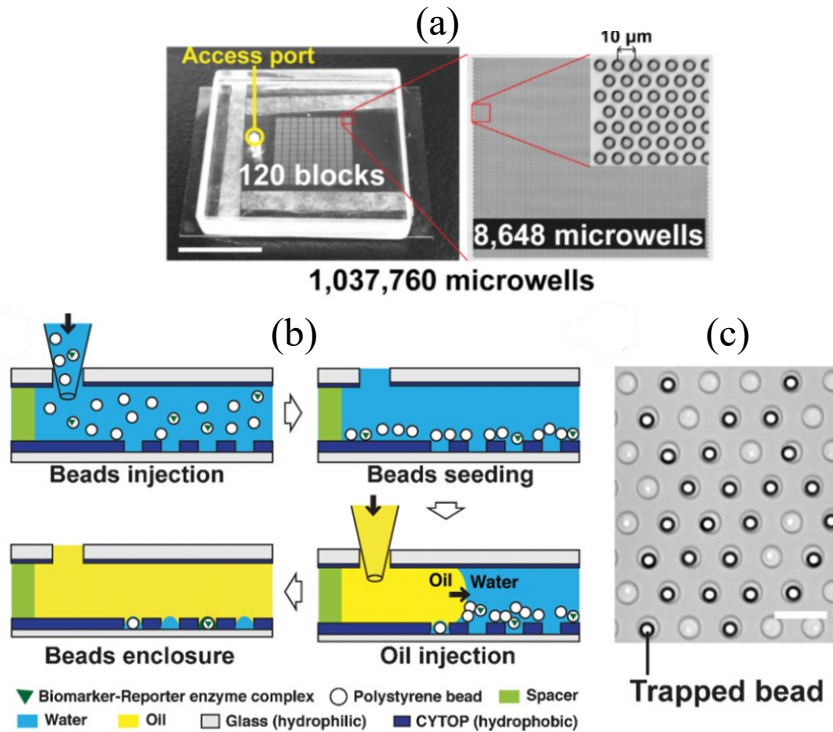


Figure 1.6: Digital ELISA device that narrows the volume per chamber to 1 fL. (a) Photograph of the device and (b) schematic diagram of the cross-sectional structure and (c) microscope image when the beads were captured by chamber [6].

1.3 Label-free biosensors using ELISA

Conventional HPLC and detection methods using labelling agents through ELISA have several problems: the equipment is very expensive, a proficient technician is required in the detection process, and the response of the adsorption process of the target molecule cannot be acquired in real-time. Therefore, we introduce the detection methods and research trends of various devices, using ELISA-based label-free biosensors as an example, which are currently being developed as devices that can easily detect target molecules.

1.3.1 Quartz crystal microbalance

A quartz crystal microbalance (QCM) is a mass-change sensing device that detects the tiny mass changes that occur uniformly on the surface of electrodes formed on a crystal owing to the resonance frequency changes caused by the inverse piezoelectric effect; it is widely used for gases and liquids. When a substance is adsorbed on the surface of a quartz crystal vibrating at a resonant frequency, the resonant frequency decreases with its mass and increases with desorption. The relationship between this resonance frequency and the mass of the adsorbed material was described in 1959 as Sauerbrey's equation [8]:

$$\Delta f = -\frac{2f_0^2}{A\sqrt{\rho_p\mu_q}}\Delta m = -\frac{f_0^2}{0.442 \times 10^6 A}\Delta m \quad (1.1)$$

where f_0 is the fundamental resonant frequency (Hz) and A is the effective surface area (cm^2) of the crystal. With respect to the electrochemical measurement device, referring to the QCM manufactured by BAS, which is widely developed, manufactured, and sold in Japan, the f_0 is 7.995 MHz and A is 0.196 cm^2 ; thus, the frequency change of 1 Hz corresponds to approximately 1.4 ng. This detection method can add detection selectivity to the sensor by changing the sensitive film on the surface of the electrodes, and many applications to biosensors as well as chemical sensors have been reported [9]–[15]. In 2008, a biosensor integrated with a flow path on top of a QCM sensor was developed and reported to successfully detect illegal drugs such as vaporized cocaine ecstasy (Fig. 1.7) [14]. In 2009, it was reported to successfully detect C-reactive protein (CRP), a biomarker for cardiovascular disease, with a minimum detection limit of 0.130 ng/mL [9]. Additionally, as an example of virus detection, a 2013 study detected the bird flu virus H5N1 within 30 min [15]. It is already available on the market as a high-performance sensor because of its versatility. Although the sensor

performance can be improved by reducing the effective surface area of the quartz crystal, reducing the size and array of the crystal is difficult because it is a bulky device.

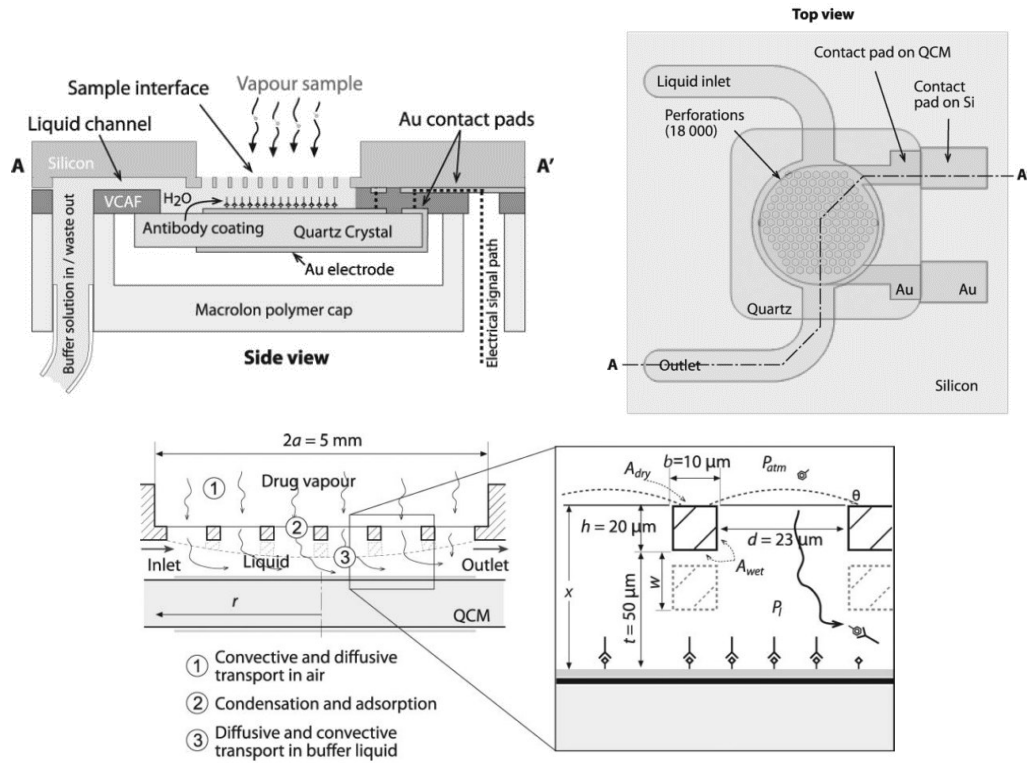


Figure 1.7: Cross-sectional and top view of the QCM biosensor with integrated flow path (top) and schematic diagram of molecular adsorption and desorption on the sensing area (bottom) [14].

1.3.2 Surface plasmon resonance

The surface plasmon resonance (SPR) method detects the response of a molecule to the adsorption on a sensor chip as a change in the angle of loss of reflected light caused by surface plasmon resonance. When light is irradiated on media with different refractive indices, if the angle of incidence is greater than the critical angle, total reflection occurs at the interface between the mediums and evanescent waves, which are electromagnetic waves, are generated on the surface of the medium with low refractive indices. Evanescent waves are standing waves whose intensity decays exponentially with the distance to the interface, and they stay only near the interface, making them an effective tool for measuring physical phenomena occurring at the interface of a medium in real-time. As a sensor that resonates with surface plasmons excited on the metal surface using

this evanescent wave, a Kretschmann configuration with a prism in close contact with gold (molecular adsorption layer) is used as shown in Fig. 1.8. By placing a thin layer of gold between the prism and the liquid, the gold surface plasmons react strongly to light and generate surface plasmon waves. In scenarios where the incident light is totally reflected (when the wavenumbers of the two surface waves coincide), it resonates in combination with the evanescent wave, and part of the energy of the incident light is used to excite the SPR, thus reducing the amount of light detected as reflected light. Since the angle at which the SPR is excited (the resonance angle) depends on the refractive index on the metal film, the antibody molecules on the gold film capture the antigen molecules and the refractive index of the interface changes, which changes the resonance angle. The amount of change in the resonance angle varies with the concentration of the target antigen molecule, facilitating the quantitative assessment of any antigen molecule from the sample solution.

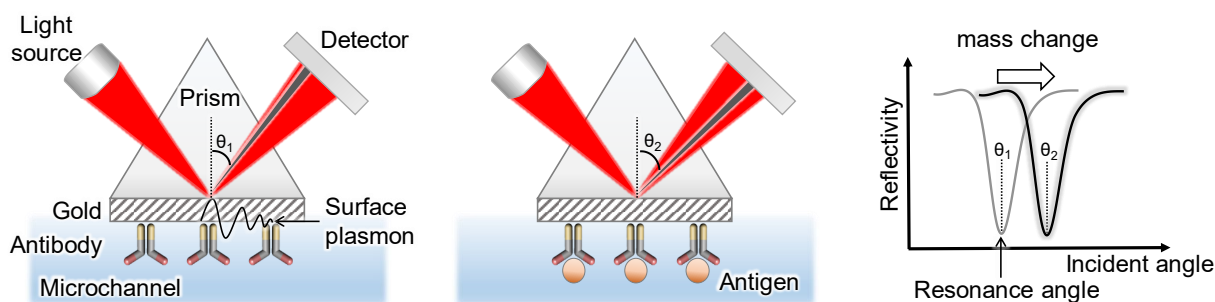


Figure 1.8: A detection method using surface plasmon resonance. Schematic cross-sectional structure of the sensor before (left) and after (centre) antigen adsorption and the angular change in surface plasmon resonance due to the antigen–antibody reaction (right).

Biomarker detection using this method was reported from 2004 to 2008 with LODs of 0.15–10 ng/mL for PSA, a well-known cancer marker [16]–[21]. In 2007, a biosensor that integrates microfluidic channels using poly(dimethylsiloxane) (PDMS) on a glass substrate and images the spatial phase variation of SPR on-chip was reported (Fig. 1.9) [17]. With this sensor, rabbit IgG was successfully detected at a concentration of 0.5 $\mu\text{g/mL}$. Furthermore, in 2012, a smartphone-based SPR detection device successfully detected anti-human β 2-microglobulin in serum and its LOD was 0.1 $\mu\text{g/mL}$ [22].

The advantages of these detection methods are that the light does not pass through the sample solution; therefore, it is not easily affected by the presence of opaque liquids or bubbles, and only the properties of the medium within $1\ \mu\text{m}$ from the surface of the sensor contribute to the SPR; thus, the amount of sample solution used is very small. However, in smartphone-based methods, since the pixel pitch and pixel design of the screen is different in each smartphone and the design value of the PDMS coupler must be changed each time to adjust the light-gathering angle, it lacks versatility. In addition, the prism-based method uses an optical system that requires detailed alignment, such as a laser or position sensitive detector (PSD) for the detection system, which makes the equipment large and difficult to achieve at a low cost. With these detection methods, optical elements such as bulk prisms and PDMS couplers focus the incident light on a localized area, which limits the number of biomarkers that can be measured in one measurement and detecting multiple biomarkers simultaneously difficult.

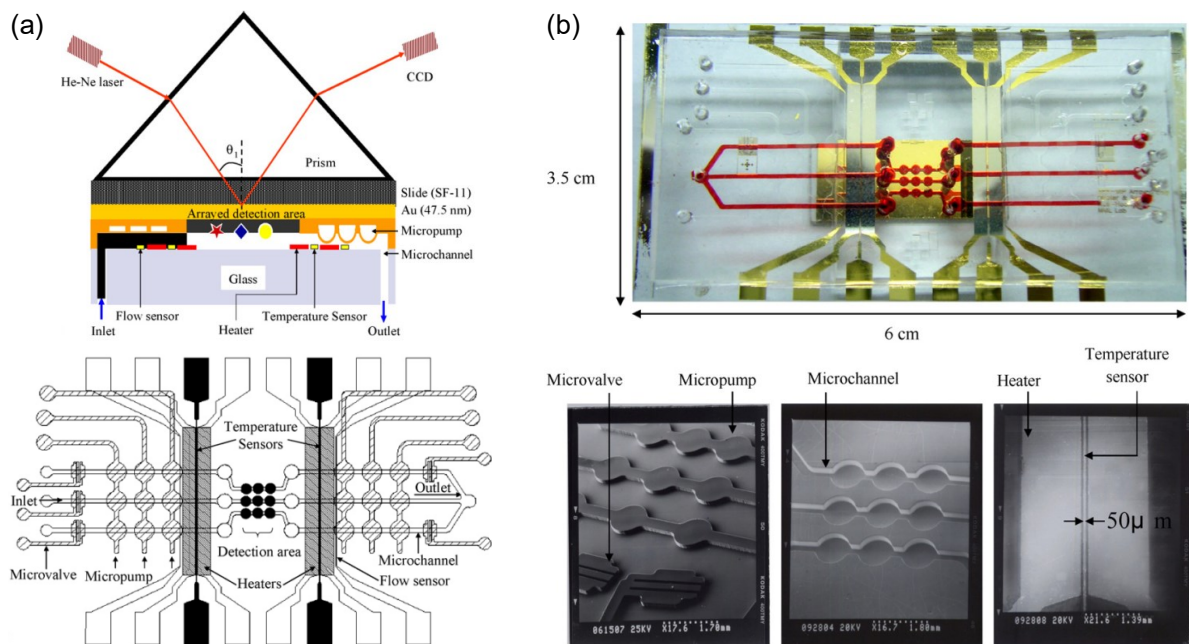


Figure 1.9: A two-dimensional array SPR phase imaging device using surface plasmon resonance[17]. (a) Schematic diagram of the sensor structure and (b) fabricated device photograph.

1.3.3 Field-effect transistor

An insulated-gate field-effect transistor (IGFET) is a device that detects changes in channel electron density caused by changes in charge density at the gate dielectric surface as the drain current changes. As shown in Fig. 1.10, during measurement, the probe DNA is immobilized beforehand on the gate insulator film of the IGFET and immersed with the reference electrode in the sample solution. In this state, with the substrate side connected to ground, current flows from the source to the drain of the IGFET. Since the electron density of the channel near the substrate surface depends on the voltage applied to the reference electrode as well as the charge of the DNA on the gate insulator, the change in charge density owing to hybridization can be detected using the electric field effect.

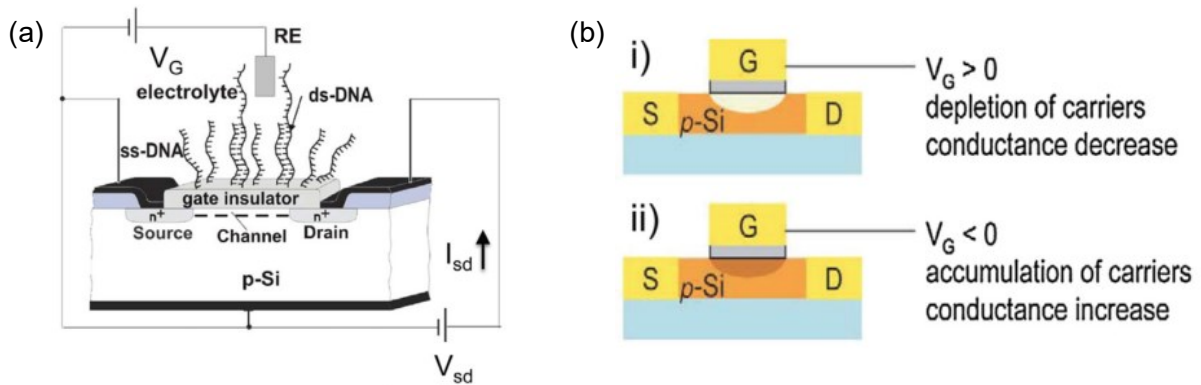


Figure 1.10: DNA detection method using planar field-effect transistors. (a) Schematic diagram of the sensor and (b) Charge density change by DNA hybridization. [23].

This method detects the charge change in the Debye length, which is formed in a region of several nanometres from the semiconductor surface, and the Debye length in the solution can be calculated using the following formula [24]:

$$\lambda_D = \frac{1}{\sqrt{4\pi l_B \sum_i \rho_i z_i^2}} \quad (1.2)$$

where l_B is the Bjerrum length ($= 0.7$ nm), ρ_i is the molar concentration per unit volume of ionic species (mol/L), and z_i is the ionic valence. The Debye length in a typical phosphate-buffered saline (PBS) corresponds to 0.7–2.2 nm at 1–10 times dilution of salt concentration. Therefore, it is useful for measuring substances with molecular sizes typically below 2 nm, such as DNA and RNA. However, in methods using antigen–antibody reactions for biomarker detection,

the typical size of antibody molecules is greater than 10 nm, which causes the antigen molecules to bind in a region beyond the Debye length. In other words, detecting large molecules is difficult because of the antigen–antibody reactions [25]. This is because antibody molecules are typically larger than 10 nm, causing the antigen to bind in a region beyond the Debye length. Therefore, as shown in Fig. 1.11, methods of forming nanostructures smaller than the Debye length on the sensor-sensitive membrane and modifying the side of the nanostructures [26] or using fragment antibodies or small aptamers isolated only from the adsorption site of the antibodies as receptors [27] have been reported. In addition to these techniques, in a 2017 study, the Debye length was extended to 7 nm by diluting the salt concentration in PBS 100-fold in silicon nanowire field-effect transistor (SiNW-FET) and PSA was detected with a LOD of 23 fg/mL (Fig. 1.12) [28]. While it has been widely studied as a high-performance sensor, the salt concentration in the buffer solution must be diluted more than 100 times to extend the Debye length, which makes measuring in an actual biological environment difficult. Therefore, it is expected to be applied as an effective tool for the detection of DNA and neurotransmitters that do not require Debye-length extension for measurements in a biological environment.

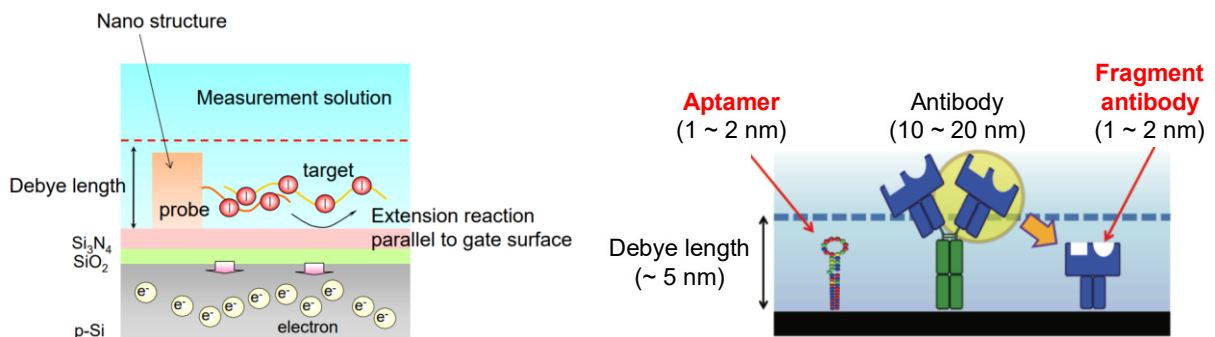


Figure 1.11: Methods for detecting charge density changes within the Debye length on a FET sensor. Method using the sidewalls of nanostructures [29] and method using aptamers and fragment antibodies [30].

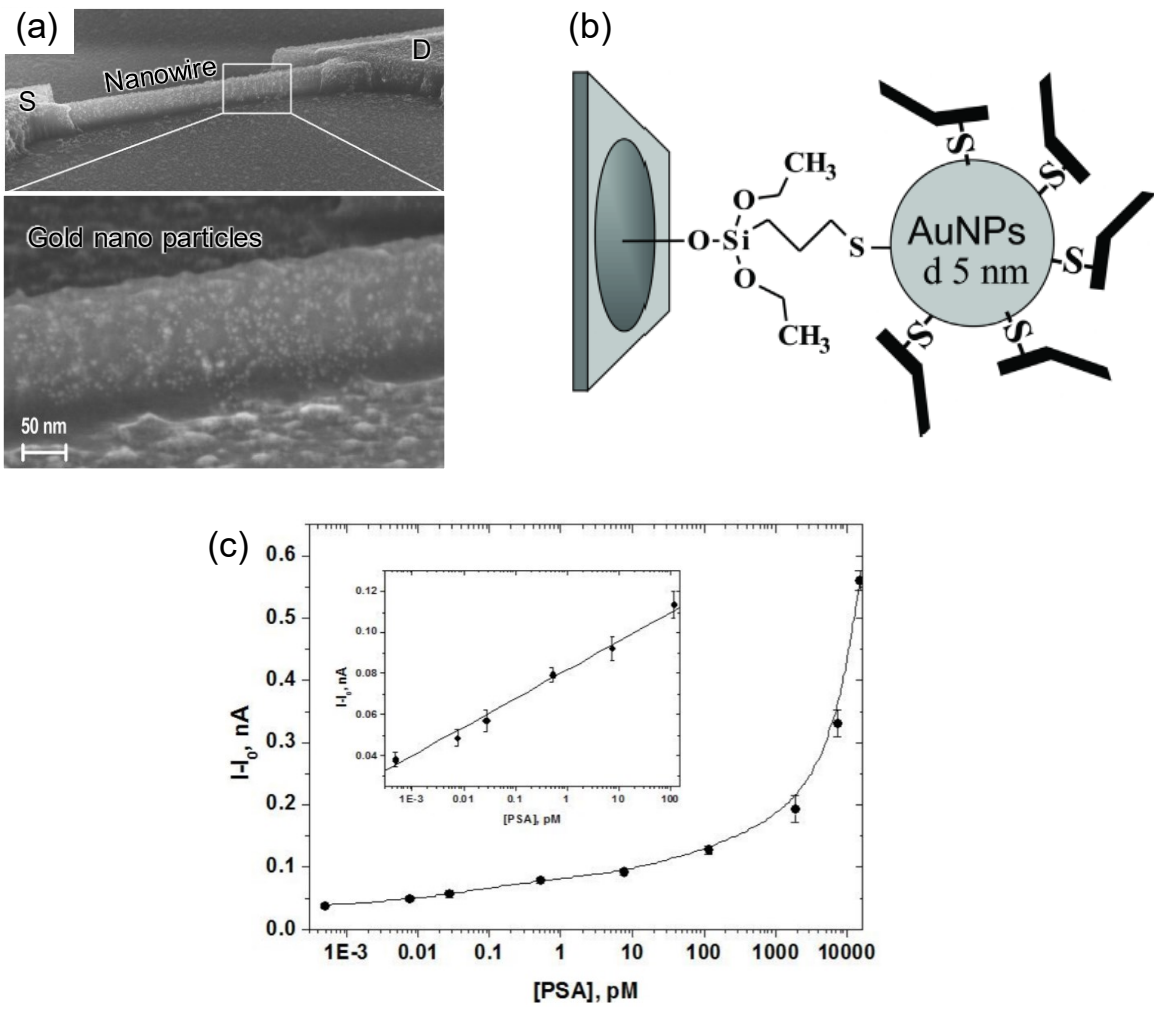


Figure 1.12: Detection method using SiNW-FET [28]. (a) SEM image of the fabricated device. (b) Schematic diagram of the molecularly modified interface using gold nanoparticles and fragment antibodies. (c) Relationship between PSA concentration and output current.

1.3.4 Surface-stress sensor

A surface-stress sensor is a sensor that detects small changes in adsorption on a structure with a non-substrate area, such as a cantilever or bridge structure. The surface of the cantilever has a layer of receptors that adsorb target molecules, such as antibodies that capture them; when the molecules are adsorbed, stress is applied to the surface of the cantilever because of molecular interactions, causing deflection. Two methods are used for this: one to detect the static deformation of the cantilever at the time of molecular adsorption [31], and the other to detect the change in resonance frequency due to the change in mass at the time of molecular adsorption [32]; the former is called the static mode and the latter the dynamic mode (Fig. 1.13). In the dynamic mode, miniaturizing the system is difficult because a circuit is required to excite the molecules for detection, and the Q-value of the resonance is reduced in liquids, which degrades the performance. Thus, for the real-time detection of molecular adsorption in liquids, the static mode is preferable. In this section, we present detection methods and the performance of reflection angle displacement sensors, capacitive readout sensors, piezoresistive sensors, and optical interferometric sensors for the detection of cantilever deflection in the static mode.

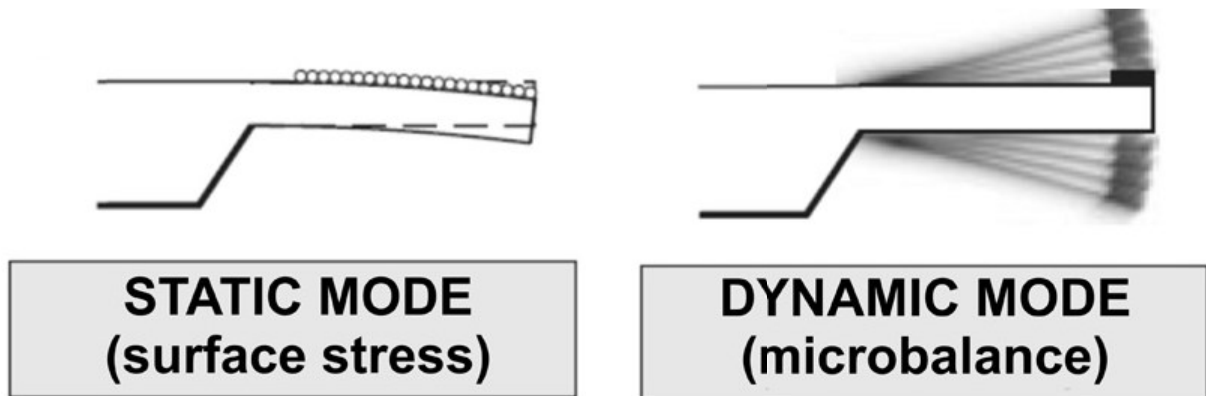


Figure 1.13: Cantilever-based surface stress sensors [33]. A method to detect static displacement (left) and a method to detect resonance frequency change based on mass change (right) during molecular adsorption.

1.3.4.1 Optical type

An optical readout sensor is a sensor for the optical detection of the deflection of a cantilever because of molecular adsorption. The deflection due to molecular adsorption is detected as the angular change of the reflected light while the cantilever is irradiated by a laser beam [34]–[39]. An example of biomarker detection using this method was reported in 2001, where PSA concentrations from 0.2 ng/mL to 60 $\mu\text{g/mL}$ were detected, demonstrating a wide dynamic range (Fig. 1.14) [34]. In a 2005 study, by using single fragment antibodies to fix the antibodies on a cantilever, the amount of deflection during the antigen–antibody reaction was increased and a biomarker with a LOD of 15 nM was successfully detected in 10 min [39]. Furthermore, in 2014, PSA was successfully detected with a LOD of 0.1 fg/mL using a method that combines the static and dynamic modes (Fig. 1.15) [40].

Each of the above-mentioned detection methods provides high sensitivity for biomarker detection as well as shorter detection times and higher detection reliability. However, the problems are the high cost because of optics requiring accurate alignment, the difficulty of miniaturization, and the difficulty of measuring in opaque liquids such as blood. Therefore, sensors developed to solve these problems are introduced in the next section.

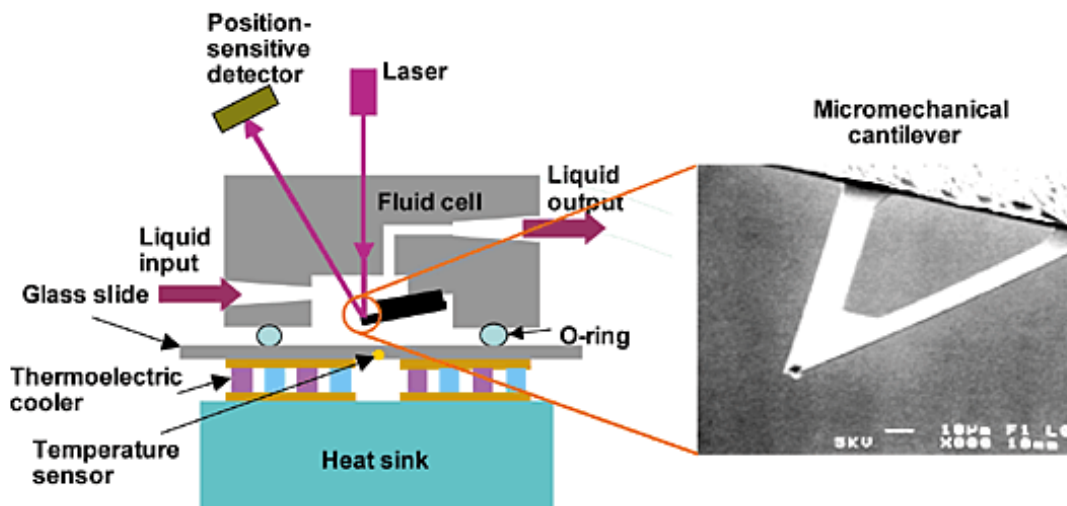


Figure 1.14: Reflection angle displacement detection system during laser irradiation [34].

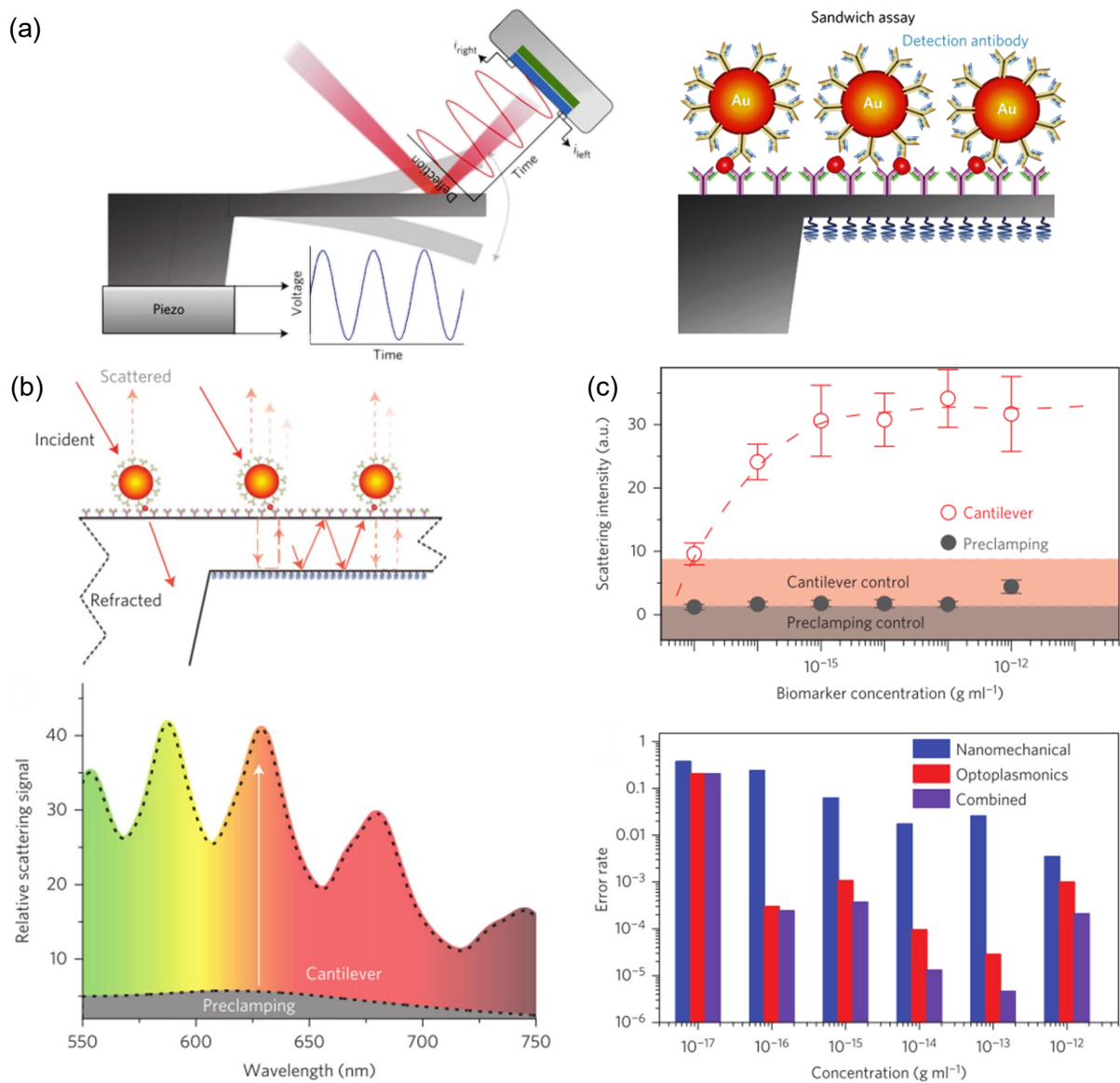


Figure 1.15: Detection method that combines static mode and dynamic mode [40]. (a) Schematic diagram of molecular modification on a cantilever using a reflective angular displacement detection system and gold nanoparticles during resonant driving of a device. (b) Enhancement of wavelength selectivity of scattered light using internal reflection of the cantilever and its spectral distribution. (c) Relationship between scattered light intensity and biomarker concentration and error probability for each detection method.

1.3.4.2 Capacitive type

A capacitance readout sensor is a sensor in which a cavity on Si is encapsulated by a polymer material with a low modulus of elasticity, and electrodes are placed at the top and bottom of the polymer material to detect the change in capacitance between the electrodes corresponding to the deformation of the film upon molecular adsorption. Conventional surface-stress sensors with a cantilever structure have the problem of decreasing the amount of deformation when molecules are nonspecifically adsorbed on the backside of the cantilever [41], but by selecting a dome structure (Fig. 1.16), which prevents nonspecific adsorption on the backside, and by selecting a low modulus polymer material as a deformable film, the deformation of the sensor can be improved [42]. The main parameters that determine the detection performance of the sensor are the molecular adsorption layer and the coverage of the gold electrode used as the top electrode to the polymer material and the air-gap length between the capacitor electrodes. Since the gold film on top of the polymer material determines the stiffness of the film, the reduction in membrane deformation can be minimised by decreasing the coverage ratio. However, since the capacitor capacity is proportional to the area of the electrode, there is a trade-off relationship with the amount of membrane deformation. Similarly, the shorter the air-gap length between the capacitor electrodes, the greater the capacitance, but the adhesion of the polymer material to the lower electrode during the formation of the hollow structure can result in device failure. Therefore, in 2006, the above parameters were optimized and a capacitive readout sensor using parylene C as the polymer material was reported to successfully detect organic vapour molecules including isopropyl alcohol (IPA) and toluene entering a nitrogen atmosphere [43]. However, the capacitance change due to membrane deformation is approximately 0.15 pF at most, which makes the detection performance low compared with other surface-stress sensors and their practical use difficult. Surface stress sensors have been reported to successfully detect *Staphylococcus aureus* by targeting bacteria that are larger than gas molecules because the amount of deflection that occurs increases with the size of the adsorbed object (i.e. the greater the amount of charge of the object to be measured) [44][45]. In this report, the use of PDMS, which has a modulus three orders of magnitude smaller than that of parylene C, in the polymer material shown in Fig. 1.17, resulted in a change in the inverse volume of $4.275 \times 10^{-2} \text{ pF}^{-1} \text{ bac/mL}$. It achieved a performance approximately 10 times higher than

conventional capacitive readout sensors. Since the cavity of this sensor is not yet sealed and the sensor is still in its unfinished state, it is hoped that the sealing process can be established in the future to prevent non-specific adsorption on the backside of the deformable membrane and make the sensor more convenient for bacterial detection.

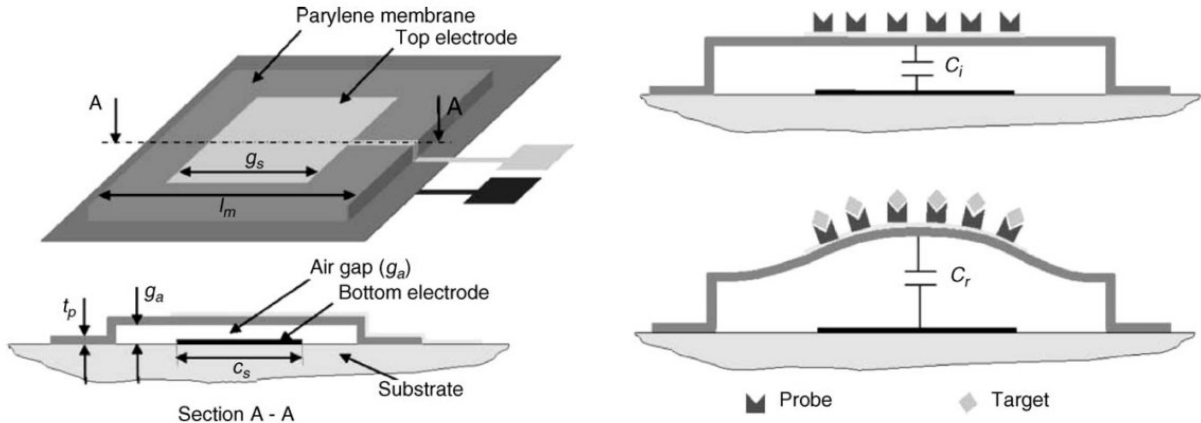


Figure 1.16: Schematic diagram of device structure and capacitance change due to molecular adsorption in capacitive readout type sensor [43].

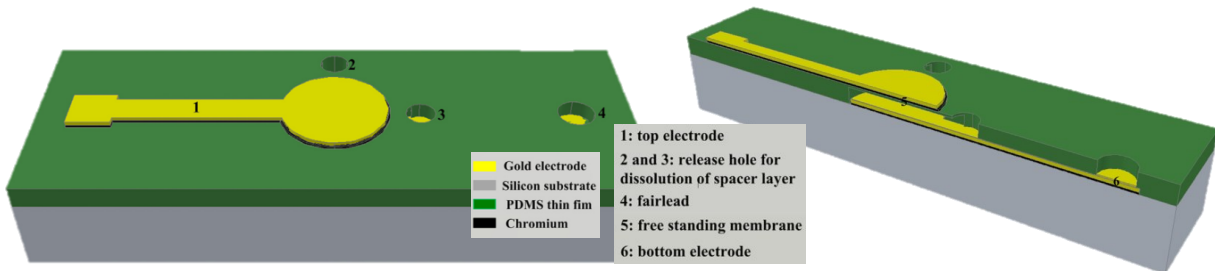


Figure 1.17: Proposed sensor design and cross-sectional structure in capacitive readout type sensor using PDMS [44], [45].

1.3.4.3 Piezoresistive type

A piezoresistive sensor is a sensor that detects the change in electrical resistance by implanting impurities such as B into Si, which causes the band structure to change when a stress or strain is applied to the impurity-implanted region. A Wheatstone bridge circuit is used to detect the piezo-resistance change (Fig. 1.18). The bridge circuit consists of a cantilever to be measured and a cantilever without a molecular adsorption layer as a reference. When a DC power supply (V_s) is applied to the bridge circuit, current flows in the diagonal ground direction; thus, a potential of V_1 is determined by the resistance ratio of the measuring and reference cantilevers. As the piezoresistance of the measurement

cantilever changes because of molecular adsorption, this resistance ratio changes; thus, V_1 changes. By measuring the potential difference between V_1 and V_2 , the amount of deflection of the cantilever can be calculated. As an example of biomarker detection using this method, a study detected PSA and CRP at a concentration of 10 ng/mL each in 2005 [46]. The method does not require optics; therefore, it has a low cost, is easy to miniaturize, does not require laser alignment, does not require metal reflective coatings, and can be used in opaque liquids, among many other advantages. Since this method was developed, it has increased the stress sensitivity to 5.7 mN/m by applying parylene C, which has a Young's modulus two orders of magnitude lower than that of Si, to the cantilever material to improve the surface-stress sensitivity of the sensor [47]. However, to support the piezoresistive region, parylene C must be designed with a thickness of a few micrometres, which makes reducing its thickness difficult, and many researchers attempted to improve the performance of piezoresistive sensors, but only a 10% was achieved. However, in 2011, Yoshikawa developed the membrane-type surface-stress sensor (MSS), which achieved a performance comparable to that of an optical readout sensor [48]. Yoshikawa reviewed the conventional cantilever structure and proposed a stress-concentrated structure by forming a small knot at the fixed end of the cantilever (Fig. 1.19) and proposed a membrane-type structure with four fixed end stress sensing parts to improve the performance. In 2012, she developed a second-generation MSS that optimized the film shape and stressed parts, realized two-dimensional arrays, and improved the sensitivity of surface stress to 0.1 mN/m, which was three to four times higher than the first-generation MSS [49]. Since this report, a structure that concentrates stress on the piezoresistive part by a similar method has been proposed, and in 2014, the nanomechanical membrane (NMM) sensor (Fig. 1.20) developed by Omidi *et al.* could detect PSA with a LOD of 0.6 ng/mL [50]. However, since the diameter of the membrane was extended to approximately 800 μm to increase detection sensitivity, the degree of integration per unit area is low, which results in a decrease in throughput.

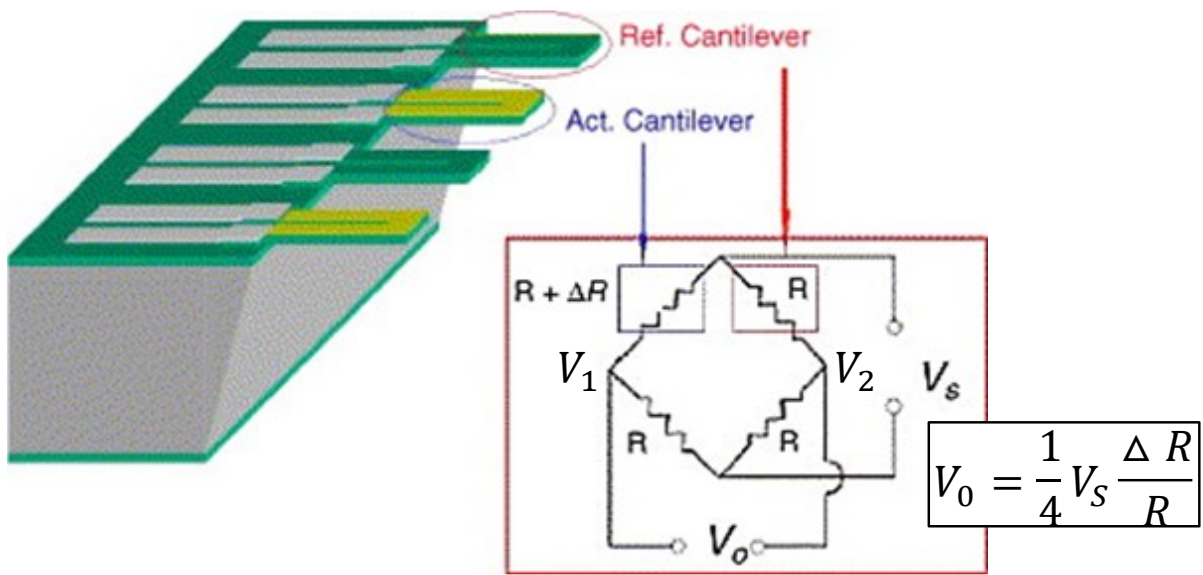


Figure 1.18: Detection method using piezoresistive change [46].

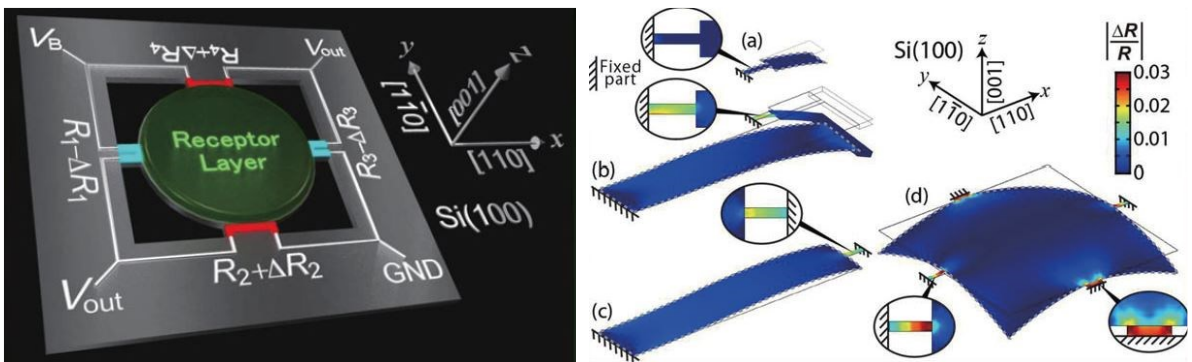


Figure 1.19: Membrane-type surface-stress sensor using piezoresistive change [48]. They proposed a structure that concentrates the stresses near the fixed end.

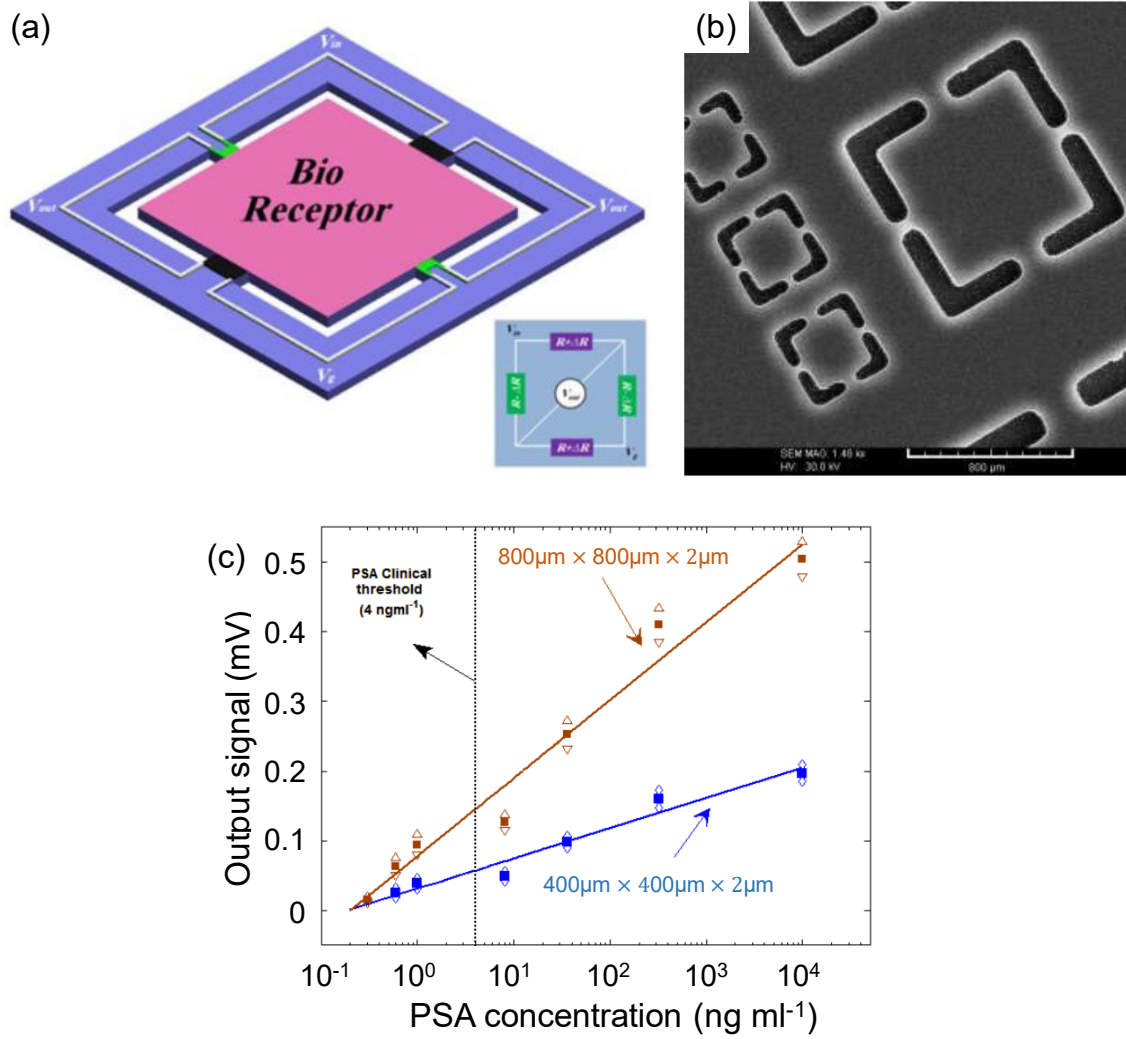


Figure 1.20: (a) Schematic diagram and (b) SEM image of the fabricated device and (c) PSA concentration vs. output voltage [50].

1.3.4.4 Optical interferometric type

The optical interferometric sensor proposed by our laboratory uses the Fabry–Perot interferometer, which transmits only light of arbitrary wavelengths from irradiated light containing various wavelengths, to detect target molecules adsorbed on the interferometer by outputting the nonlinear change in intensity of the incident light as a photocurrent using a photodiode. As shown in Fig. 1.21(a), two reflection mirrors (reflectance r , transmittance t) are placed parallel to each other at a distance of d . When the light E_I is injected into these mirrors at an angle θ from the perpendicular component, multiple reflections occur between the mirrors. The light passing through the mirror (E_T) will be a superposition of each component wavefront transmitted after receiving an even number of reflections. The transmitted light is maximal when there is no phase difference between each component wavefronts, and at other wavelengths cancelling interference occurs between each transmitted component wavefronts and the transmitted light is reduced. If the film is sufficiently thin such that the effect of light interference in the reflecting mirror is negligible, the wavelength transmittance (T) of the transmitted light is expressed as

$$T = \frac{1}{1 + \left[\frac{4r \sin^2\left(\frac{\delta}{2}\right)}{(1-r)^2} \right]}, \quad \delta = \frac{4\pi m d \cos\theta}{\lambda} \quad (m : \text{integer numbers}) \quad (1.3)$$

where δ represents the phase difference between adjacent transmitted light. The relationship between transmittance and wavelength is shown in Fig. 1.21(b), where the transmittance is greatest for a phase difference of $\sin(\delta/2)=0$. Additionally, the higher the reflectivity of the mirror, the better the wavelength selectivity of the transmitted light.

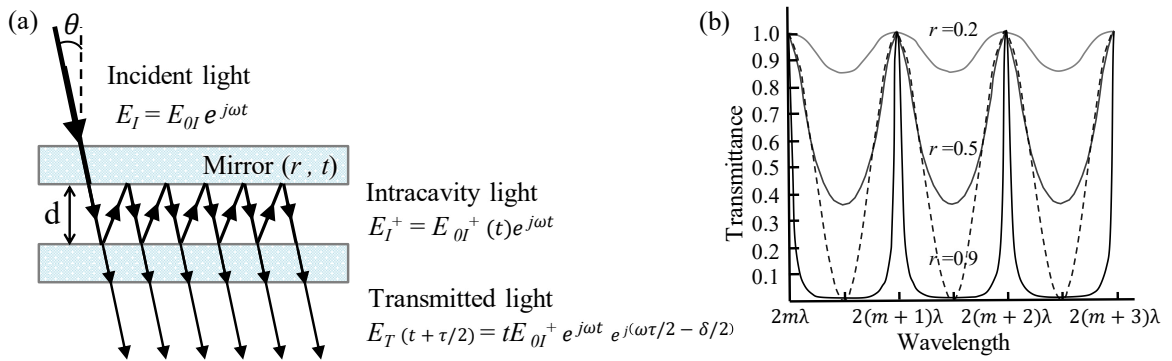


Figure 1.21: (a) Schematic diagram of principle of multiple reflections and (b) characteristics of transmission wavelength in Fabry-Perot interferometer.

This sensor employs a deformable membrane above a silicon photodiode, which flexibly deforms owing to surface stress. The Fabry–Perot interferometer comprises a deformable film, an air gap, and a silicon dioxide layer for passivation of the photodiode (Fig. 1.22). Surface stress caused by repulsion between antigen molecules adsorbed to antibody molecules on the deformable membrane causes the central portion of the membrane to deflect upward (①–②). This mechanical displacement is converted to a change in the transmittance of the interference spectrum (③) and output as a photocurrent by a photodiode (④), which enables us to convert the small amount of displacement of the deformable membrane caused by the adsorption of the target molecules into a photocurrent. Since this surface-stress sensor can use parylene C with a thin film of approximately 100 nm as the deformable membrane material, the surface-stress sensitivity can be expected to increase by more than two orders of magnitude compared with the piezoresistive sensor using parylene C as a cantilever material [47], [51], [52].

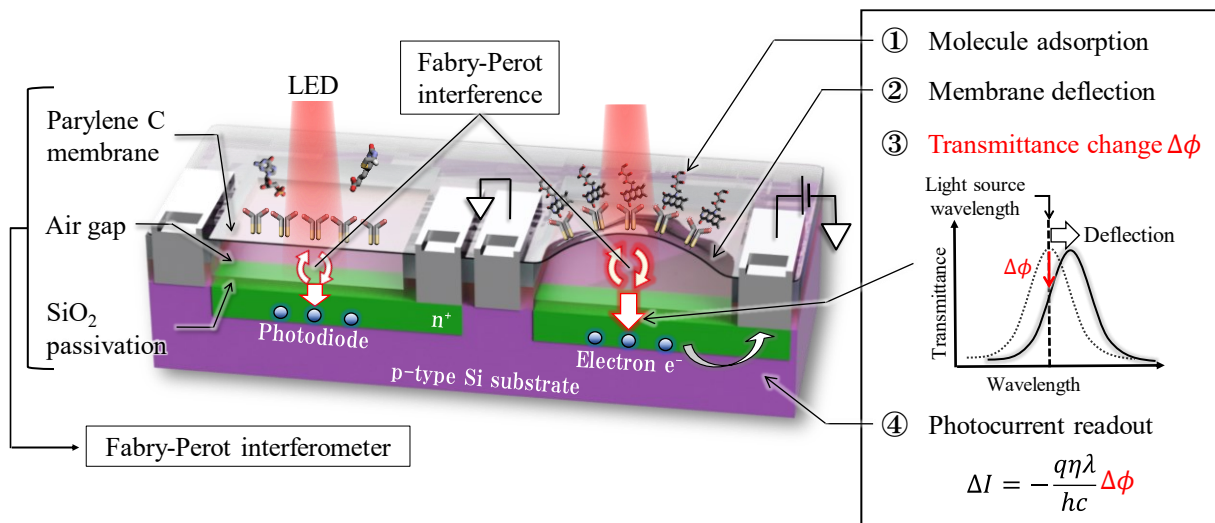


Figure 1.22: Schematic diagram and detection principle of the surface stress sensor based on a MEMS Fabry–Perot interferometer [52].

In our laboratory, we developed a device that integrates microfluidic channels on a MEMS interferometer which can reduce the time required for the antigen–antibody reaction by concentrating the antigen in a narrow space between antibodies. As shown in Fig. 1.23, the specimen is pumped from the inlet by a syringe pump and the target molecule included in the specimen is adsorbed on the sensor via microfluidic channels. When PBS and bovine serum albumin antibody

(anti-BSA) at a concentration of 100 ng/mL were pumped into this microfluidic channel at 1 $\mu\text{L}/\text{min}$, the photocurrent response (Fig. 1.24), in which the deformable membrane sinks downward because of liquid pressure and deflects upward because of changes in surface stress at the time of antibody molecule adsorption, suggests the feasibility of biosensing in liquids in this sensor [53]. At this stage, the sensor has not yet obtained an output response because of the antigen–antibody reaction; therefore, establishing an interface to adsorb antigen molecules onto the sensor will enable arbitrary molecular detection using the antigen–antibody reaction.

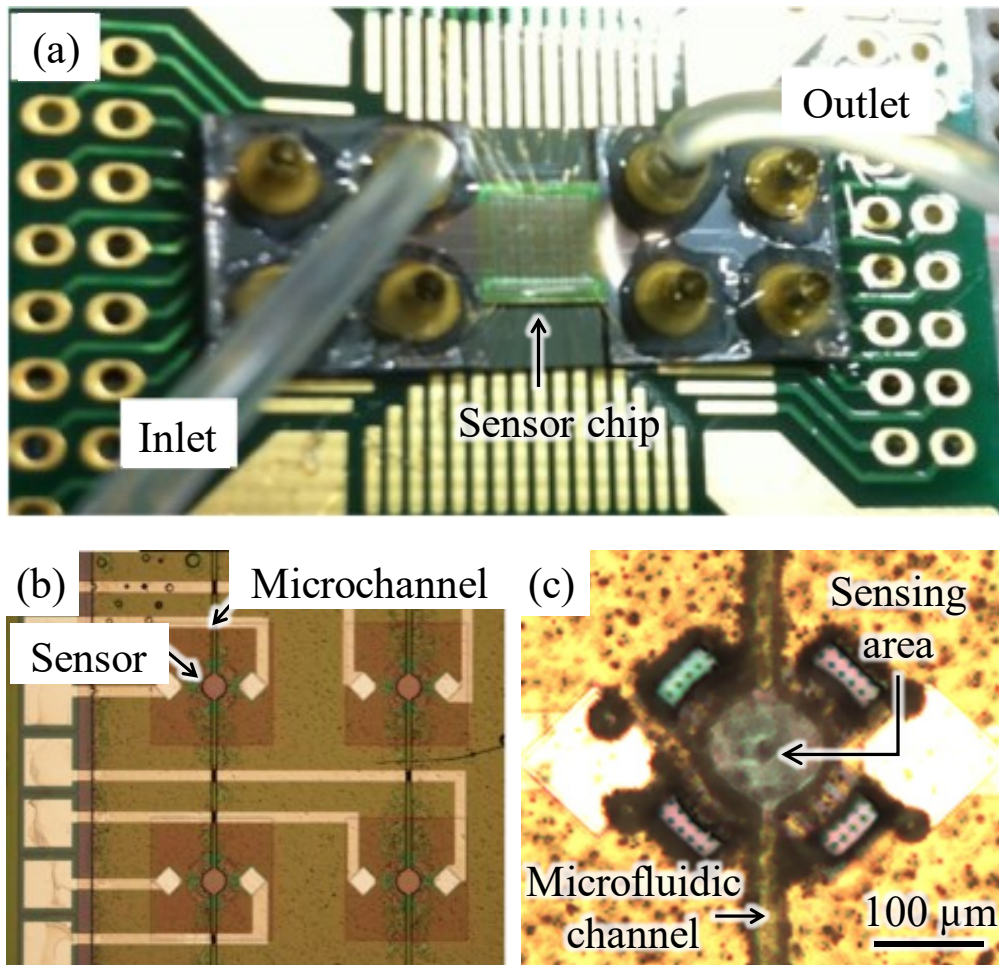


Figure 1.23: MEMS optical interferometric surface stress sensor integrated with microfluidic channel [53]. (a) Photograph of the device and (b) an optical microscope image and (c) a magnified view of the sensor.

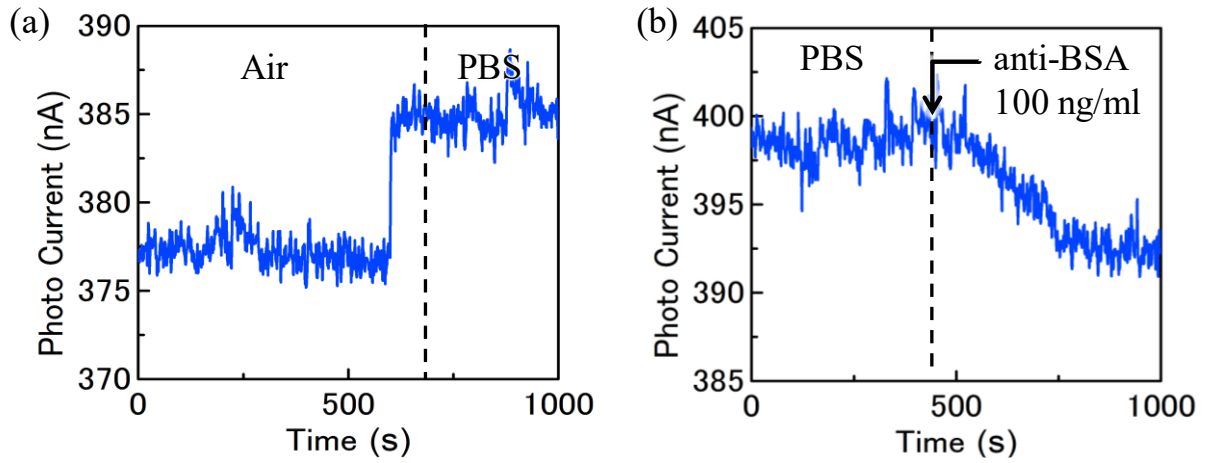


Figure 1.24: (a) Pressure response to PBS and (b) surface stress response to anti-BSA [53]

1.4 Current status and challenges of biosensors in biomarker detection

Table 1.1 summarizes the characteristics of the biosensors described until the previous section. Assuming the application to the screening of diseases by detecting biomarkers, a sensor, which has a small area per single element and is capable of multi-biomarker detection, is required. SPR and QCM sensors, which use bulk prisms and crystals and require detailed alignment optics, also have some problems: difficulty in simultaneously measuring multiple markers on a single sensor element and the amount of antibody reagents required for a single measurement increases, making it difficult to achieve at low cost. Therefore, detection methods through FET and MEMS surface-stress sensors are considered to be suitable for biomarker detection.

Table 1.1 Summary of pros and cons in each biosensor

Sensor type	Sensing area (μm^2)	Multi-biomarker detection	Note	Ref.
QCM	6.4×10^7	Difficult	Detection performance decreases in liquid measurement	[9]
SPR	N/A	Difficult	Require detailed alignment optics (Difficult to miniaturize)	[17,18]
FET	6	Possible	Difficult to detect macromolecules exceeding Debye length	[28]
Surface Stress Sensor (Piezoresistive type)	6.4×10^5	Possible	Difficult to detect small molecules. Integration per unit area is low.	[54]
Surface Stress Sensor (This study)	7.9×10^3	Possible	Detection performance can be improved without expanding sensing area	N/A

Fig. 1.25 shows the size and type of molecules that each sensor is suitable for detecting using FET and MEMS surface-stress sensors. FET sensors are suitable for the detection of small neurotransmitters and gas molecules because the size of detectable molecules is limited to a few nm owing to the Debye length limitation. However, the mechanical displacement caused by the repulsive Coulomb force between adsorbing molecules is limited by the material properties of the MEMS surface-stress sensor, which makes detecting small displacements of small molecules difficult. Thus, the MEMS surface-stress sensor is suitable for detecting high concentrations of gas molecules and macromolecules. Therefore,

the sensor, which can comprehensively detect a variety of molecules from small to large ones in a biological environment without extending the Debye length, has not been realized.

The proposed MEMS optical interferometric surface-stress sensor is expected to improve the sensitivity of surface stress by two orders of magnitude or more compared with conventional MEMS surface-stress sensors, and it can detect small changes in surface stress. In other words, the high sensitivity of the sensor is expected to enable it to detect small molecules that have been difficult to detect using conventional surface-stress sensors. We expect that the realization of the device with no restriction on the size of detectable molecules and can measure the adsorption process of target molecules in a biological environment in real-time will become an innovative basic technology in medical research. Such a sensor can be achieved by improving the detection sensitivity of the sensor.

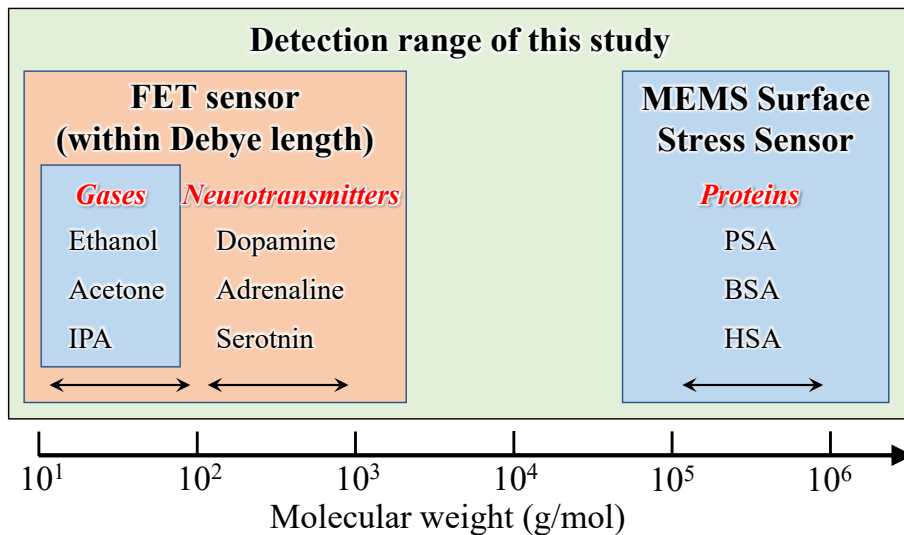


Figure 1.25: Detectable molecular size in FET and MEMS surface stress sensors

1.5 Factors determining the deflection amount of the deformable membrane in the optical interferometric surface-stress sensor

In a surface-stress sensor, the amount of deflection of the moving part that occurs during molecule adsorption (Fig. 1.26) is expressed by the following equation [51]:

$$\Delta z \propto \frac{l^2(1-\nu)}{Et^2} \Delta\sigma \quad (1.4)$$

where z is the displacement, l^2 is the area of the movable part, ν is the Poisson's ratio, E is the Young's modulus, t is the thickness of the deformable part, and σ is the applied surface stress. The parameters that contribute significantly to the amount of deformation are Young's modulus, area, and thickness, which are derived from the material at a deformable part. Therefore, by reducing the Young's modulus and thickness, and expanding the deformable membrane's area, the amount of deflection during molecular adsorption can be increased. However, if molecules are non-specifically adsorbed on the backside of the deformable membrane, the amount of deformation is reduced because the surface stress in the direction prevents the deflection caused by the target molecules adsorbed on the top surface of the membrane. Therefore, to prevent molecules from adsorbing on the backside of the membrane, researchers formed a dome-shaped structure to seal the interior [43] or applied a special blocking treatment to the backside [55].

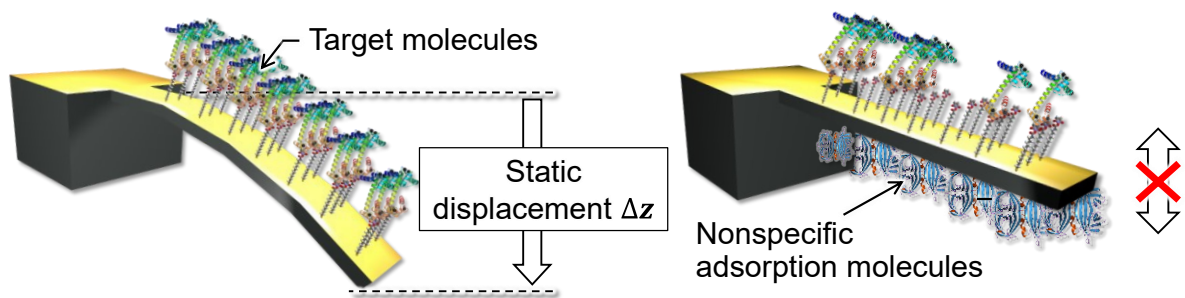


Figure 1.26: Schematic diagram of MEMS surface stress sensor when molecules adsorption. Static displacement when target molecules adsorption (left) and reducing the amount of deflection by non-specific adsorption (right).

1.6 Factors determining the limit of detection in the optical interferometric surface-stress sensor

The proposed interferometric surface-stress sensor outputs the amount of deflection of the deformable membrane as a current response of the photodiode, which is caused by the transfer of the Coulomb repulsive force acting between the adsorbing molecules to the membrane as surface stress. Since the charge of a molecule in a liquid depends on the pH of the solution, the charge density in the microdomain increases as the molecule is adsorbed on the sensor, and the Coulomb repulsion force acting between the adsorbed molecules increases accordingly. As shown in Fig. 1.27, when the immobilization density of the antibody molecules is kept constant, the Coulomb repulsion force increases, and large deflection occurs

when the concentration of the target molecule is high. However, at low concentrations, the charge density and Coulomb repulsive force within the microdomain on the sensor are reduced, resulting in a decrease in the surface stress transferred to the membrane and a decrease in the amount of deflection, i.e. a decrease in the output current. Therefore, if the photocurrent change corresponding to the deflection of the membrane becomes difficult to detect because it is buried in the dark current, that value will be the smallest (LOD) at which the surface stress change can be measured.

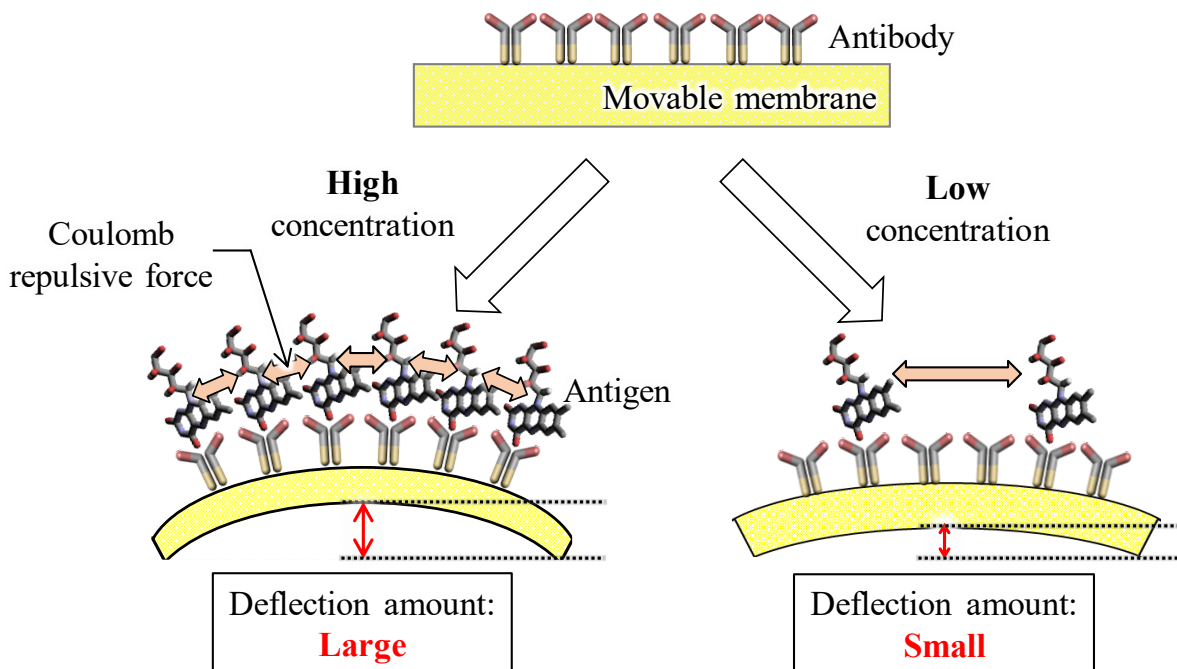


Figure 1.27: Effect of difference in concentration of target molecules on the amount of deflection if the immobilization density of antibody molecules is constant

In a previous study, to improve the LOD of a sensor by reducing the dark current of the photodiode, we attempted to increase the photosensitivity of a photodiode in Si by extending the width of the depletion layer between the impurity region and substrate and forming a photodiode in a p-type substrate with an n-well layer with a lower impurity concentration than the conventional n⁺ layer [56]. By adopting this method, we succeeded in reducing the dark current from 573 to 200 pA using a light source with an intensity of 10 μ W and a wavelength of 650 nm (Fig. 1.28a). Based on the measured values, we obtained the amount of deflection using the finite element method and the change in transmittance during deflection

by optical analysis, and we calculated the LOD, which was estimated to be less than 0.1 mN/m (Fig. 1.28b).

However, when a small change occurs in the surface stress near the LOD owing to the adsorption of low-concentration molecules, the amount of change in the transmitted light intensity to convert this change into a current is low, and the amount of change in current output is very small (several tens of pA), making it difficult to obtain a high signal-to-noise ratio for dark current values. To increase the amount of output current for small surface-stress changes, the wavelength selectivity of the interferometer must be improved. This problem can be solved by increasing the gradient of the transmission spectrum of the Fabry–Perot interferometer, resulting in increasing the amount of change in the transmitted light intensity at the time of membrane deformation. That is, by designing the wavelength selectivity of the interferometer, the degree of freedom to control the signal conversion efficiency is obtained. Therefore, the techniques to improve wavelength selectivity will be introduced in the next section.

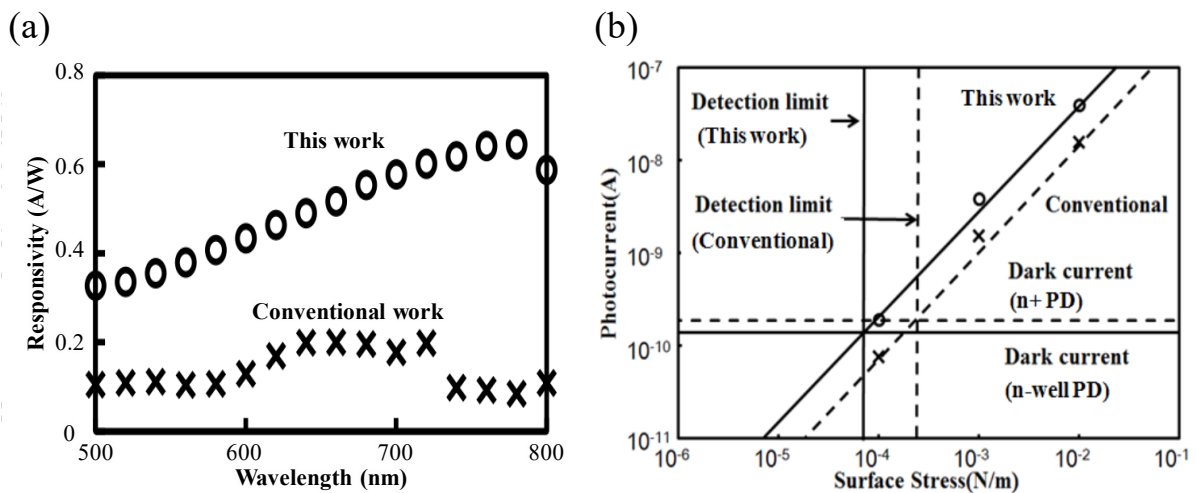


Figure 1.28: Relationship between (a) photosensitivity and (b) surface stress change and photocurrent output in an optical interferometric surface stress sensor [56]. The photodiode's dark current value determines the minimum detectable surface stress value.

1.7 Increasing wavelength selectivity using a metal half-mirror structure

For techniques to increase wavelength selectivity in structures based on optical interference, reports on the introduction of dielectric multilayers and thin metal films into half-mirror materials are available [57]–[60]. The former uses the glancing angle deposition (GLAD) method, in which materials are deposited from different angles onto a glass substrate, and a Fabry–Perot interferometer with refractive index periodicity and high reflectance spectrum is constructed by stacking high refractive index semiconductor material Ti with nanometre periodicity (Fig. 1.29). The incident light on the interferometer is multiply reflected by layers of Ti thin films stacked at nanometre intervals, and the wavelength selectivity is increased by selectively transmitting light of the same phase, and the full width at half maximum (FWHM) in the infrared region is successfully narrowed to 2.56 nm.

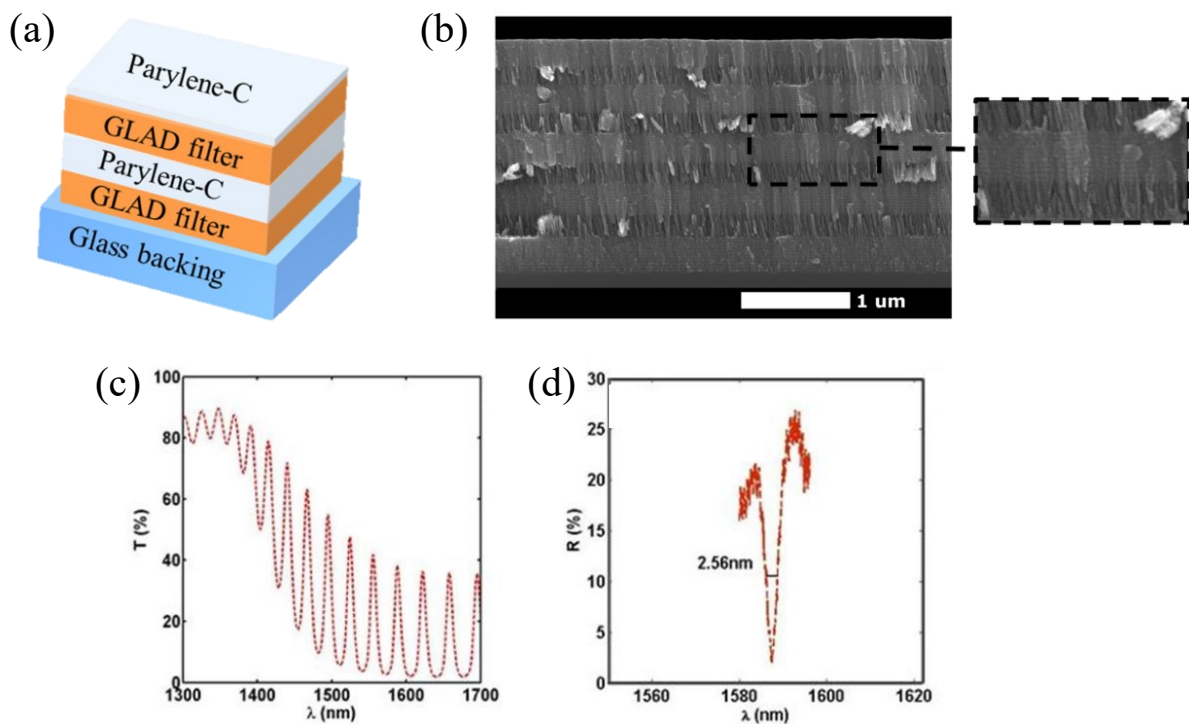


Figure 1.29: Fabry-Perot Interferometer with dielectric multilayers ^[41]. (a) Schematic diagram of the four-layered structure using GLAD and Parylene C and (b) cross-sectional SEM image. (c) Transmission spectrum and (d) reflected spectrum for one period in the infrared band.

In contrast, the latter method proposes Fabry–Perot variable colour filters with 20-nm Au and Ag half-mirror materials deposited at the top and bottom via SiO₂ spacers on a glass substrate for application to transmissive displays in the visible light wavelength range [60] (Fig. 1.30). Half-mirrors deposited above and below the interferometer increase the multiple reflections of the light incident on the interferometer and improve the wavelength selectivity of the transmitted light. Furthermore, by applying a bias between the mirrors, the electrostatic force causes the movable mirrors to be in contact with the spacers and obtains an interference colour of the optical path length determined by the thickness of the spacers. By adopting an Ag mirror with high reflectivity and low absorption in the visible region, the reproducibility of pixels displaying red and blue is increased to 22% and 63%, respectively.

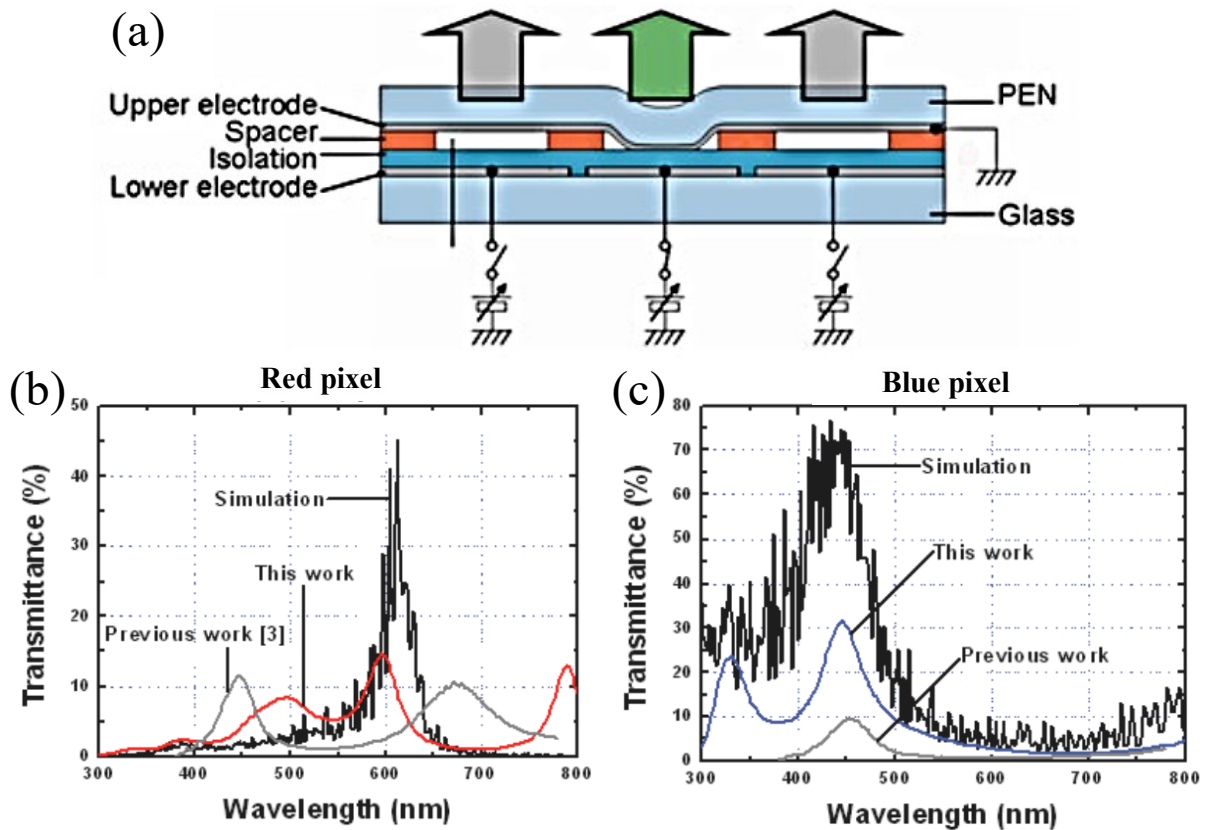


Figure 1.30: Variable Fabry-Perot filter using Au and Ag in the half-mirror material [60]. (a) the proposed transmissive Fabry-Perot structure and (b) transmission characteristics in the red and (c) blue wavelength ranges.

Assuming that the optical interferometric surface-stress sensor proposed by our laboratory is used in blood inspection, light with low absorbance wavelengths

should be used for haemoglobin, water, and proteins in the blood. In the UV region, the protein's structure is destroyed by light irradiation [61], [62], and in the near-infrared region after 1100 nm, light absorption occurs because of the use of light energy for the vibrational transitions when the OH and CH bonds of the protein are irradiated to light [63]. In contrast, in the near-infrared region of 800–1100 nm, the higher harmonics and electronic absorption of the protein's CH, OH, and NH bonds are very weak, and its permeability is excellent, making it suitable for non-destructive and non-invasive analysis. Since this wavelength region is also the region of high photosensitivity of Si photodiodes, constructing a Fabry–Perot interferometer that transmits near-infrared light at 800–1100 nm is desirable. In optical interferometers, parylene C as a deformable membrane and SiO₂ as a protective film on the photodiode serve as the half-mirrors of the interferometer, but these materials have less than 10% reflectance in the near-infrared wavelength region; thus, the wavelength selectivity of transmitted light is poor (Fig. 1.31a). This can be solved by introducing a metal with high reflectivity in the near-infrared wavelength region into the half-mirror material (Fig. 1.31b). Although the intensity of the transmitted light is reduced by the introduction of a highly reflective metal, the reduction in intensity can be compensated for without affecting the target molecule by adjusting the irradiation intensity using a highly transmissive light with a wavelength of 800–1100 nm as the incident light. Therefore, the optimization of the sensor structure and materials for the realization of an interferometer with metal half-mirrors was studied to improve the wavelength selectivity of the interferometer.

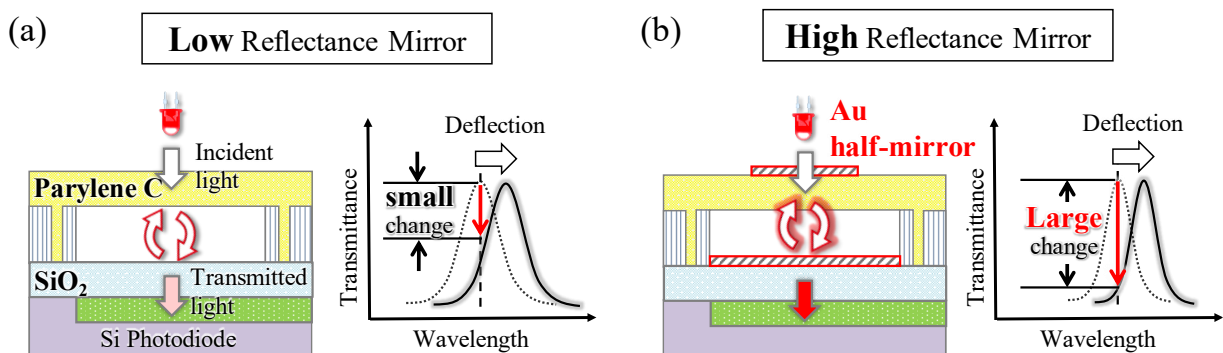


Figure 1.31: Schematic diagram of the cross-sectional structure and interference characteristics of an optical interferometric surface stress sensor with (a) a conventional structure and (b) a newly proposed metal half-mirrors with high reflectivity in the near-infrared region.

1.8 Aim of this study

In this study, we aimed to develop a sensor that can detect molecules of various sizes without extending the Debye length. The MEMS optical interferometric surface-stress sensor proposed by our laboratory can comprehensively detect low-concentration molecules and small molecules, which have been difficult to detect using conventional surface-stress sensors as well as large molecules exceeding the Debye length by optimizing the wavelength selectivity and geometry parameters of the interferometer. Therefore, for a highly sensitive detection of target molecules of various sizes, we fabricated interferometers with metal half-mirrors structure and cavity-sealed structure with optimized geometry parameters, which can improve the detection performance of the sensor and constructed bio-interfaces to adsorb molecules on the sensor. Through these tasks, we aimed to develop a sensor for a label-free and comprehensive detection of proteins and neurotransmitters in liquids and gas molecules in air.

1.9 Outline

In this thesis, we develop a MEMS sensor which can detect proteins and neurotransmitters in liquids and gas molecules in air for a label-free detection of a variety of molecules from small molecules to large molecules. We evaluate the effectiveness of the sensor by constructing a bio-interface on which each target molecule can be adsorbed and obtaining the response of the adsorption of target molecules. The outlines of each chapter are as follows:

Chapter 1

As a background, we describe the importance of detecting various biomarkers ranging from small to large molecules and present the research trends and challenges of conventional biosensors that have been successfully used for biomarker detection. Additionally, several solutions to improving the detection performance of the proposed optical interferometric MEMS surface-stress sensor for the detection of low-concentration and small molecules that have been difficult to detect using conventional MEMS surface-stress sensors are introduced.

Chapter 2

The optical design of a MEMS interferometer with a metal half-mirror structure and optimization of the structure and thickness conditions is introduced, as well as fabrication of the device based on these findings to confirm the improvement in wavelength selectivity.

Chapter 3

The construction of a bio-interface onto the interferometer with metal half-mirrors for detecting macromolecular is introduced. After immobilization of antibody molecules, the feasibility of biosensing using the antigen–antibody reaction of this sensor is demonstrated by the acquisition of the reaction in which the deformable membrane deflects upward because of the change in surface stress at the time of antigen molecule adsorption. By calculating the difference in the amount of deflection between selective and non-specific adsorption, the selective detection of macromolecule is achievable. Furthermore, recent results, in which a novel interferometer fabricated by our laboratory, that the concentration dependence and LOD of protein are introduced.

Chapter 4

A cavity-sealed MEMS interferometer with high surface-stress sensitivity is proposed to suppress the decrease in the surface-stress sensitivity and non-specific adsorption on the backside of the deformable membrane, which have been problems for interferometers with metal half-mirrors structures. The shape parameters in the proposed structure are analysed, and the fabrication of the device based on the knowledge obtained in the analysis is discussed. Considering the application to the detection of gas molecules in the air in the fabricated sensor, a polymer membrane which can be used for the detection of gas molecules in the air and proteins in liquids is proposed.

Chapter 5

The membrane which has the characteristic of contraction or expansion upon absorption of gas molecules is formed on the cavity-sealed interferometer. A response dependent on the air-gap length of the interferometer upon exposure of volatile ethanol gas to this interferometer was obtained. Furthermore, the concentration dependence and LOD to volatile ethanol gas is evaluated.

Chapter 6

The construction of a bio-interface onto the interferometer with a cavity-sealed structure for detecting neurotransmitter is discussed. A molecularly imprinted polymer (MIP) film, which can impart the same specificity to the sensor as well as the antibody molecules, were constructed by forming the template of target molecules. The composition of this MIP film and the formation of the neurotransmitter template are evaluated. Using the MIP film which confirmed the template formation, the detectability of neurotransmitters is mentioned by comparing the sensor response because of the presence or absence of neurotransmitters.

Chapter 7

The results obtained by this study and future prospects are summarized.

Chapter 2. Investigation of metal half-mirror structure for a MEMS interferometer with high wavelength selectivity

2.1 Preface

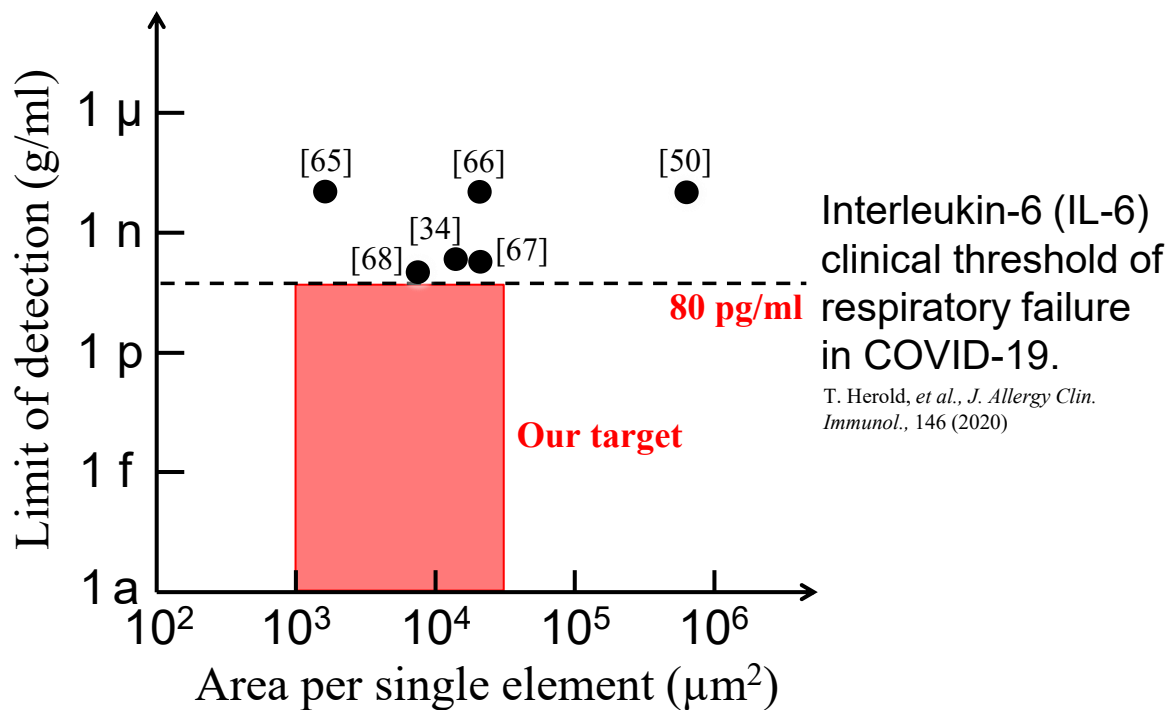
In the MEMS interferometric surface-stress sensor, the LOD is defined as the point at which photocurrent change corresponding to the deflection of the membrane becomes difficult to detect because it is buried in the dark current. When a small change in the surface stress near this LOD occurs, obtaining a high signal-to-noise ratio for dark current values becomes difficult. This can be solved by increasing the wavelength selectivity of the MEMS interferometer. By increasing the amount of intensity change of the transmitted light caused by small deflection of the membrane by improving wavelength selectivity, the output response at low concentrations of the adsorbed target molecules is expected to increase.

This chapter presents the selection of the mirror material and the optical design of the interferometer for the realization of a metal half-mirrors structure, the investigation of the coverage to suppress the decrease in the surface-stress sensitivity of the sensor because of the mirror on the membrane, and the comparison of the transmission intensity change with and without mirrors when a small deflection occurs to improve the wavelength selectivity of the MEMS interferometer. Finally, the fabrication process of the MEMS interferometer that reflects the findings of these designs, and the results of the evaluation of the fabricated interferometer's geometry and wavelength selectivity are presented.

2.2 Aiming for the detection of macromolecular biomarker

Various biomarkers exist for macromolecular proteins secreted by cells. As an example, among patients infected with COVID-19, one of the common features of patients who suffer respiratory failure and become severely ill is that the concentration of interleukin-6 (IL-6) exceeds 80 pg/mL, which has been reported to be highly correlated with severe illness [64]. Therefore, by achieving a detection sensitivity of 80 pg/mL, it can be used for the screening of patients with severe diseases. Various surface-stress sensors have been developed, and their

detection limits and area per single element are summarized in Fig. 2.1. Assuming the application to a simple Internet of Things (IoT) sensor, a sensor with a small area per single element and a detection limit of low concentration are desirable. The most sensitive one among conventional surface-stress sensors has an LOD of 0.1 ng/mL in the size of 10^3 – 10^4 μm^2 per single element. However, a surface-stress sensor with an LOD less than 80 pg/mL has not been reported. Although surface-stress sensors can increase the amount of deformation depending on the area of the detection part, increasing the sensitivity while maintaining the degree of integration is difficult since the increase in sensitivity results in a decrease in the degree of integration. However, our proposed optical interferometric surface-stress sensor can increase the sensitivity without expanding the area owing to the design of the wavelength selectivity of the interferometer. Therefore, we aimed to realize a sensor with a detection limit of less than 80 pg/mL in an area of approximately 10^3 – 10^4 μm^2 , which is equivalent to the area of conventional devices.



[34] G. Wu, *et al.*, *Nat. Biotechnol.*, 19 (2001)

[66] M. G. Von, *et al.*, *Anal. Chem.*, 82 (2010)

[50] M. Omid, *et al.*, *Procedia Eng.*, 87 (2014)

[67] M. Yue, *et al.*, *Nano Lett.*, 8 (2008)

[65] J. Bausells, *et al.*, *Microele. Eng.*, 145 (2015)

[68] K. S. Hwang, *et al.*, *J. Appl. Phys.*, 8 (2009)

Figure 2.1: Comparison of area per single element and LOD in each surface stress sensor [34], [50], [65]–[68].

2.3 Design of the MEMS interferometer

2.3.1 Optical design

Fig. 2.2 shows the proposed cross-sectional structure of the MEMS optical interferometer with high wavelength selectivity. Parylene C, the Young's modulus of which is two orders of magnitude less than that of silicon, was used for the movable membrane material, and a thin metal half-mirror was implemented as the top and bottom part of the interferometer. Assuming this device is used for blood inspection, a metal with high reflectivity is required in the near-infrared wavelength region, where the absorption coefficient of haemoglobin and water in blood is small and the responsivity of the photodiode formed in silicon is sufficient. Fig. 2.3 shows the result of the rigorous coupled-wave analysis (RCWA) of the relationship between the FWHM of the transmission wavelength spectrum and the film thickness of Au/Ti, Ag, and Al which are generally used in the semiconductor process. The film thickness of the mirror and the FWHM of the transmission wavelength spectrum indicated an inversely proportional relationship. Although the change in transmitted light intensity with the addition of a mirror when the deformable membrane was displaced by 10 nm became 3.1% smaller than the scenario without a mirror, the decrease in intensity without affecting the molecule to be measured could be compensated for by utilizing light with excellent transmittance at 800–1100 nm as the incident light. When the film thickness of each mirror material was 50 nm, we observed that the FWHM was 5.2, 10.2, and 12.8 nm for Ag, Au/Ti, and Al, respectively. The analysis results indicated that the sharpest interference spectrum can be contained when Ag was selected as the half-mirror material, but several problems were encountered in terms of tolerance to the etching gas at the release process, resulting in a decreasing reflectance of the mirror. Additionally, the surface of the Ag was oxidized during the dry-etching, which made immobilizing antibody molecules on the Ag mirror impossible. Therefore, Au was selected as the half-mirror material for process compatibility, although its wavelength selectivity is inferior to that of Ag.

Based on the above conditions of half-mirror materials and thickness, Fig. 2.4 shows the optical analysis results for the change in the transmitted light intensity for the 50 nm-thick Au mirror and no mirror scenarios. Comparing the two structures, we observed that the spectral gradient increased in the proposed

structure, and we estimated that the wavelength selectivity could be increased by 10.7-fold with the integration of Au mirrors.

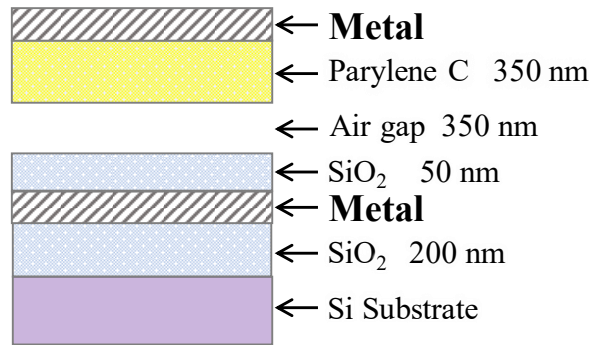


Figure 2.2: Cross-sectional structure of the MEMS optical interferometer with high wavelength selectivity.

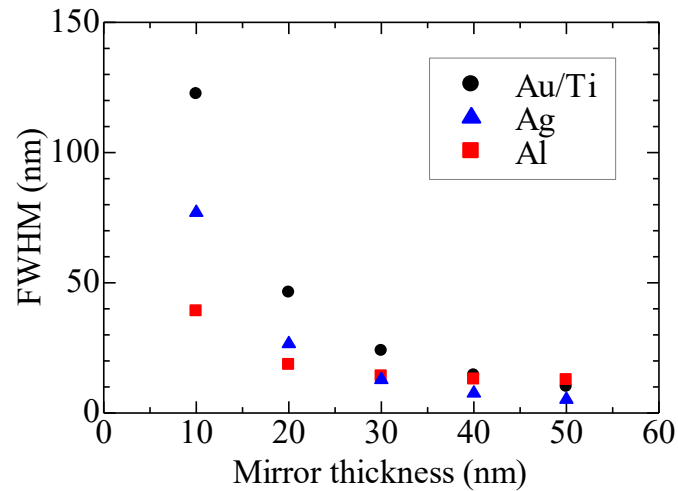
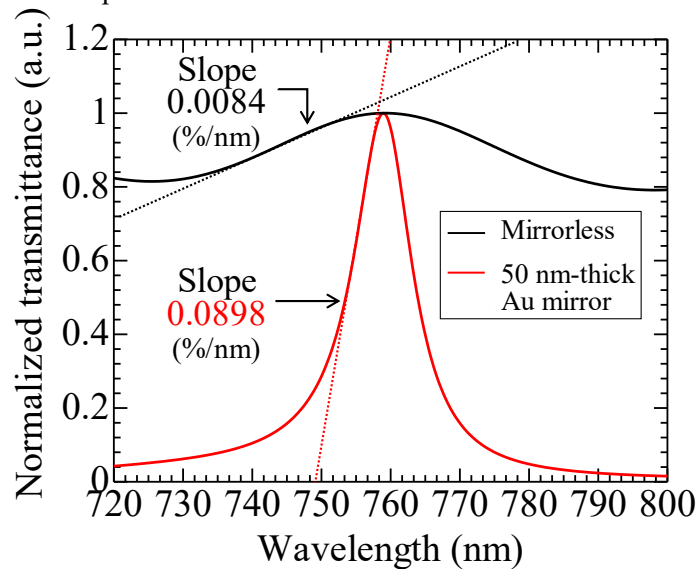


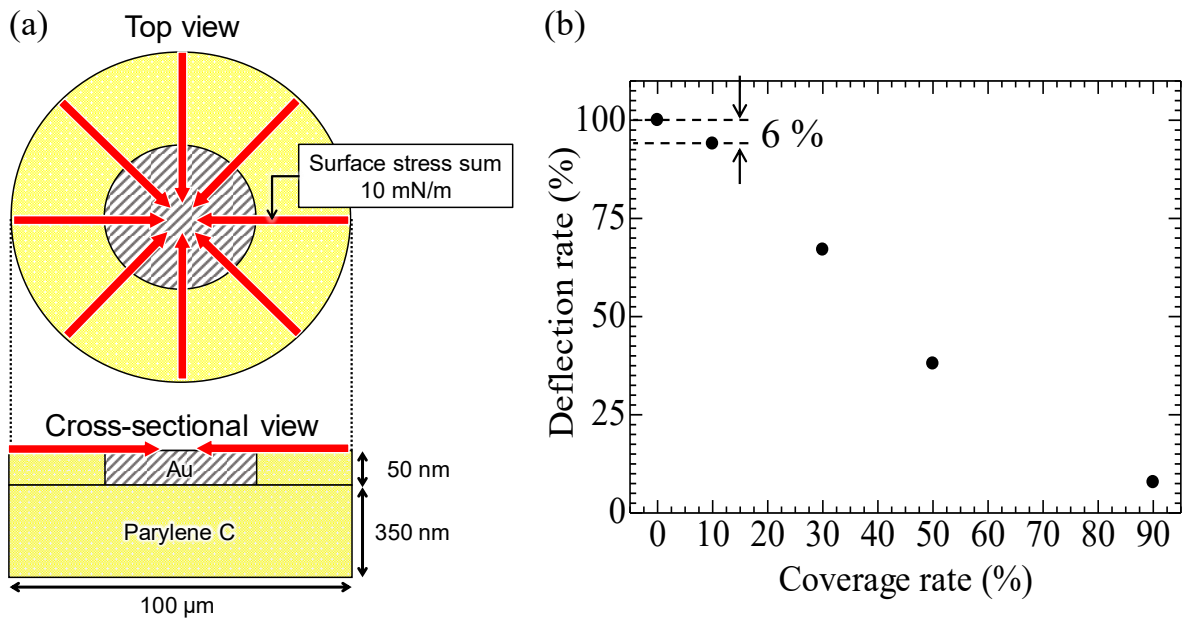
Figure 2.3: Relationship between thickness of each mirror material and FWHM.



Figures 2.4: Optical analysis results for the change in the transmitted light intensity with the 50 nm-thick Au mirror and no mirror. The wavelength selectivity is improved by a factor of 10.7 when comparing the spectral gradient.

2.3.2 Mechanical simulation

We assumed that the stiffness of the movable film increases by adding the half-mirror to the upper part of the deformable membrane and the surface-stress sensitivity decreases. Therefore, we simulated the surface-stress sensitivity associated with the coverage ratio of the upper half-mirror through finite element method analysis using the software ANSYS. Figs. 2.5a and 2.5b show the analysis model using ANSYS and results of the change in deflection of the deformable membrane as a function of coverage of the 50 nm-thick Au half-mirror on the parylene C deformable membrane. The analysis model had a sensing area diameter of 100 μm , and the thicknesses of the parylene C and Au films were 350 and 50 nm, respectively. Surface stress was applied to in-plane direction from the upper edge of the parylene C film with reference to Yoshikawa's report [48]. Therefore, surface stress was applied to the whole membrane, and when the Au half-mirror was formed with a coverage of 10% on the sensing area, the decrease in the deflection amount could be suppressed to approximately 6%. For example, this decrease in the surface-stress sensitivity could constitute a sensor with a sensitivity equivalent to the initial sensitivity by reducing the film thickness of parylene C by 10 nm. Thus, by appropriately designing the coverage ratio of the upper half-mirror, only the wavelength selectivity can be increased without decreasing the surface-stress sensitivity. Conversely, as the sensor size decreases, forming a half-mirror with a small coverage rate becomes increasingly difficult; thus, the MEMS optical interferometer was designed such that the coverage rate of the upper half-mirror was 25%. This is because the decrease in surface-stress sensitivity in this scenario can be suppressed to be approximately 20%. Considering the area of Au to connect to the electrodes, the coverage is 34%, and the decrease in the amount of deflection in this scenario is approximately 35%. The simultaneous increase in surface-stress sensitivity and wavelength selectivity can be achieved by searching for process conditions that increase the patterning resolution of Au mirrors on parylene C.

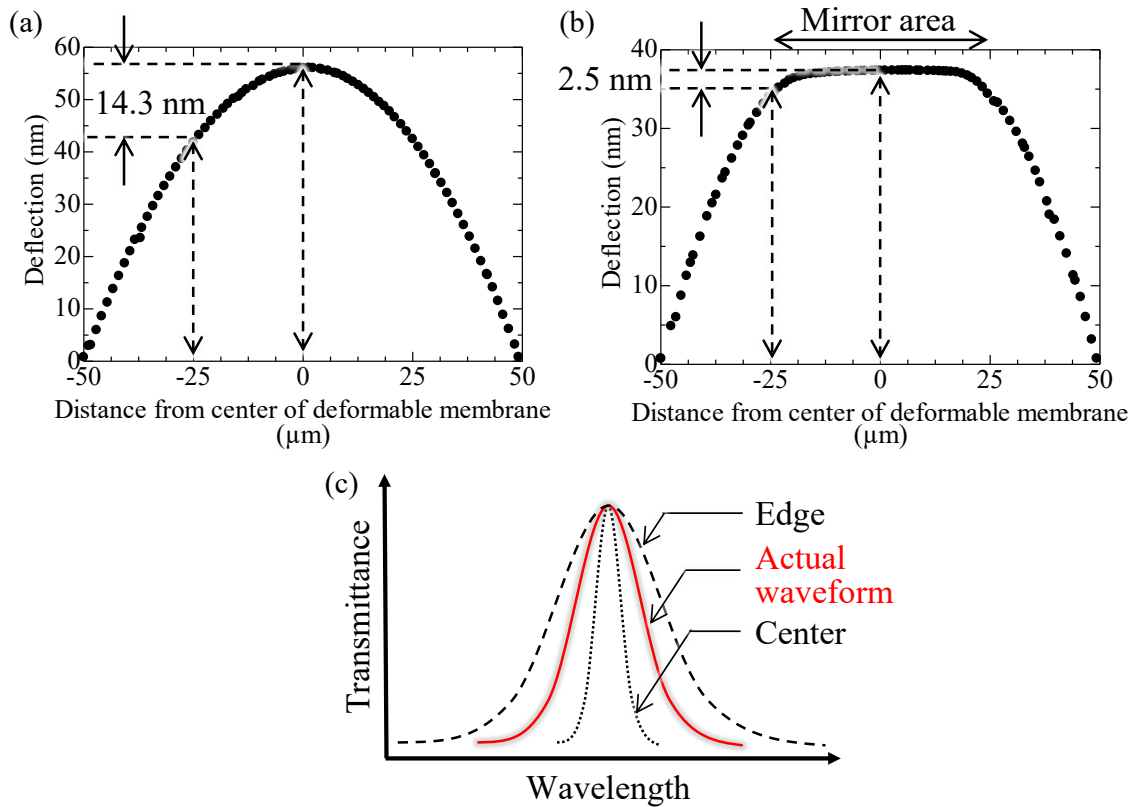


Figures 2.5: (a) Analysis model (b) relationship between the coverage of the Au half-mirror on the movable film and the deflection amount of the membrane.

For an Fabry–Perot interferometer, a high flatness of the mirror surface is an important parameter because it can suppress the scattering of the incident light on the mirror surface and permits more light to enter the interferometer. Therefore, the effect of the flatness of the mirror above the deformable membrane by the integration of Au mirrors was evaluated using finite element analysis. Fig. 2.6 shows the difference in the amount of deflection at the centre of the membrane and at a distance of 25 μm from the centre when the membrane deformed between a conventional structure without mirrors and a structure with a 25% Au mirror coverage. Comparing the difference in the amount of deformation between them, we observed it to be 14.3 nm in the conventional structure without mirrors and 2.5 nm in the structure with integrated mirrors. This difference was due to the increased stiffness of the film in the mirrored area and the support of the membrane by the mirror, indicating that a flat upper mirror can be formed by the integration of Au.

Interferometers with low mirror flatness cause the optical path length immediately below the mirror to change in the centre and vicinity of the mirror when the upper mirror is deformed during light illumination (Fig. 2.6a). In other words, the light transmitted through the interferometer contains a transmitted light component with reduced optical path length, resulting in a transmission

spectrum with reduced wavelength selectivity (Fig. 2.6c). Therefore, by integrating the Au onto a deformable membrane, the flatness of the upper mirror of the interferometer is maintained when the movable film is deformed, permitting light with highly selective wavelength to be transmitted.

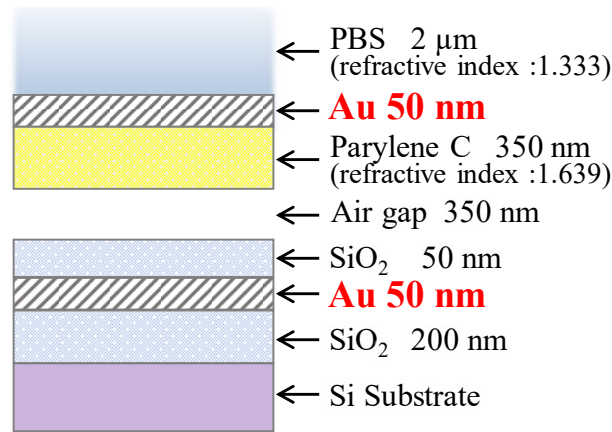


Figures 2.6: Deflection of the deformable membrane in (a) a conventional structure without a mirror and (b) an Au mirror with 25% coverage when a surface stress of 10 mN/m is applied. (c) Schematic diagram of transmission spectrum in an interferometer with low flatness of the mirror.

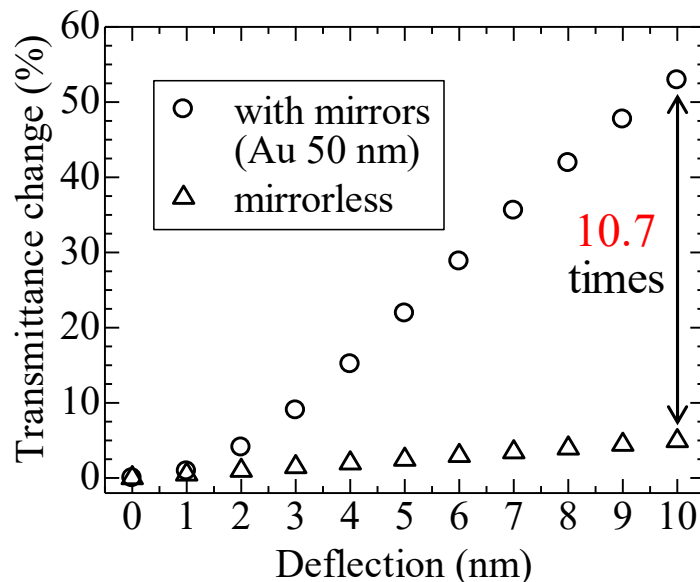
2.3.3 Analysis of transmittance change to the deflection of deformable membranes in liquids

To determine the relationship between the amount of deflection of the deformable membrane and the change in transmitted light intensity when molecules are adsorbed on the interferometer in a liquid, we calculated the relationship between them through optical analysis using the analytical model shown in Fig. 2.7, and the results are shown in Fig. 2.8. In this analytical model, the analysis was performed under the condition of irradiating light from air while the sensor was immersed in PBS. The analysis in Section 1.2.2 indicates that the decrease in surface-stress sensitivity can be suppressed by designing the proper

coverage of the upper half-mirror and the thickness of the deformable film. Therefore, in this analysis, the comparison was based on the assumption that the interferometer with an integrated Au half-mirror is an ideal structure with no reduction in surface-stress sensitivity. While no significant difference was observed in the amount of deflection below 1 nm, a maximum increase of 10 nm in the air gap with increasing deflection was observed to result in a 52.93% change when Au mirrors are added. The conventional structure without mirrors resulted in a 4.93% change at the point of highest transmission intensity change. This result indicated that the change in transmitted-light intensity because of small displacements can be increased by 10.7-fold because of increased wavelength selectivity.



Figures 2.7: Optical analysis model of the MEMS interferometer in liquid.



Figures 2.8: Relationship between the amount of deflection of the deformable membrane and the transmittance change in a conventional structure without mirrors and a structure with 50 nm-thick Au half-mirrors.

2.4 Fabrication procedure

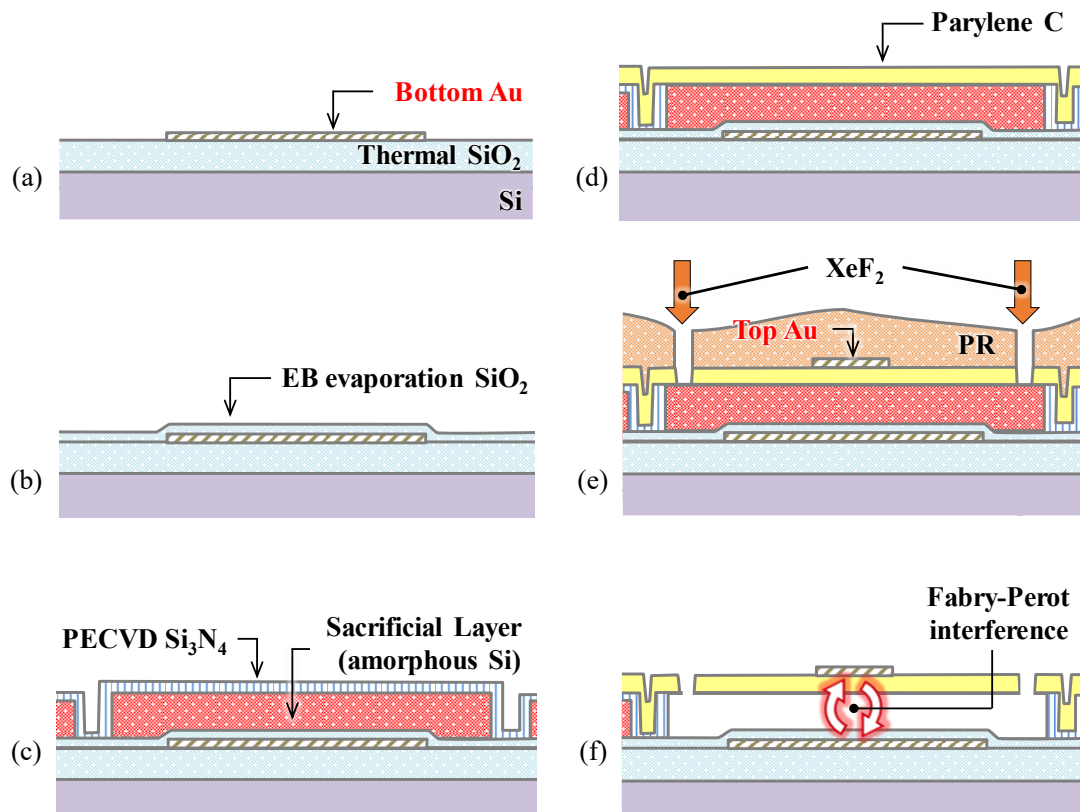
Fig. 2.9 shows the fabrication procedure of the MEMS interferometer with high wavelength selectivity. Considering the compatibility of the semiconductor process for integration with the photodiode, the fabrication process of this interferometer was based on a process that can be formed at less than 300 °C. The details of the fabrication procedure are as follows:

- (a) A 200-nm thick SiO_2 film was formed on a silicon substrate. This film had the effect of electrically isolating the bottom Au half-mirror of the interferometer and the n-diffusion layer in the Si substrate when the photodiode was integrated. To form Au mirrors using the lift-off process, after patterning with photoresist (THMR-iP3100HS LB 15cp), we used a high vacuum evaporator (ED-1600, SANVAC) to deposit Ti with a thickness of 5 nm as a binder layer, and then we deposited Au with a thickness of 50 nm. The wafer was then immersed in acetone and two ultrasonic rinses were performed to form Au mirrors while inhibiting the re-attachment of the stripped Au to the substrate.
- (b) A 120 nm-thick SiO_2 film on Au mirrors was deposited using a high vacuum evaporator capable of low-temperature deposition. Exposure of Au to XeF_2 , which was used during the formation of air gaps in the optical interferometer, would have caused it to be etched; therefore, SiO_2 films were employed to prevent this.
- (c) Following the SiO_2 deposition process in (b), the deposition source was changed to Si in the same apparatus and a 400 nm-thick Si film was deposited. Si has a property of being etched when exposed to XeF_2 , and because it selectively etches only the air-gap region of the interferometer (the sacrificial layer), the Si was processed into the shape of the sacrificial layer using a reactive ion etching device (RIE-200F, SAMCO). Since the thickness of this sacrificial Si film corresponded to the air-gap length of the interferometer, the peak position of the interference spectrum could be controlled by adjusting the thickness of the Si film to be deposited. In addition, since the XeF_2 used during sacrificial layer etching diffused isotropically, a region that acted as a side stopper to prevent lateral diffusion of the sacrificial layer was necessary to form. A plasma chemical vapour deposition (CVD) device (PD-220NS, SAMCO) using chemical vapour deposition was used to coat the sacrificial

layer with a 500 nm-thick silicon nitride film, considering the etching selectivity of XeF_2 , which enables a high coverage on uneven surfaces.

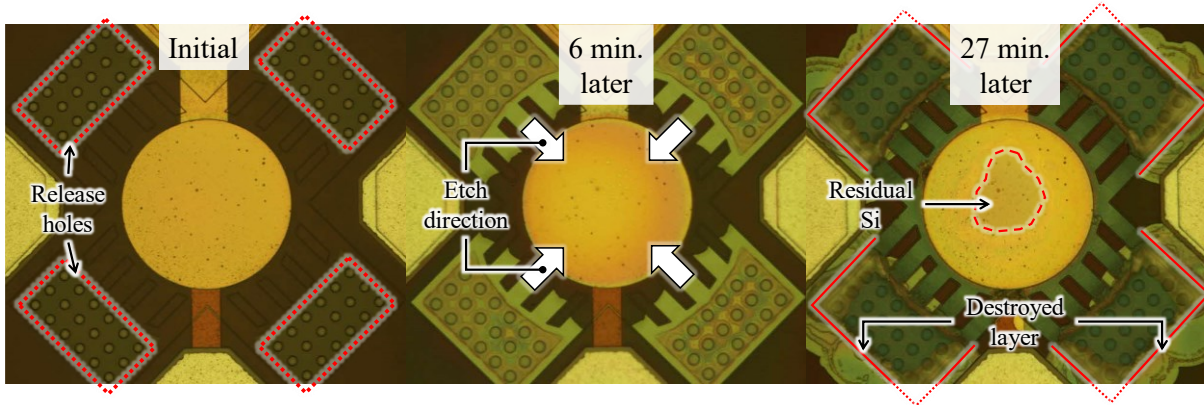
- (d) The Si_3N_4 above the sacrificial layer was removed using reactive ion etching. Before depositing the organic material parylene C to act as a deformable membrane, the wafer was subjected to silane coupling treatment to improve the adhesion between the inorganic and organic materials. The Si wafer was immersed for 15 min in a mixed solution obtained by stirring IPA, deionized water (DIW), and silane A-174 at a ratio of 100:100:1 for 2 h to apply silane on it. After this interfacial treatment, a 350 nm-thick parylene C film was deposited using a parylene coater device (PDS2010). This deposition method can be used at room temperature and in a vacuum as well as CVD, which reduces residual stress and permits a uniform film thickness regardless of surface shape.
- (e) A 50 nm-thick film of Au, which served as a half-mirror on top of the interferometer, was deposited using a high vacuum evaporator. The structure of the interface between the upper mirror and parylene C was designed to prevent mirror delamination by performing a silane coupling treatment before Au deposition. Similar to the bottom Au mirror, the top Au mirror was formed by the lift-off process. Subsequently, to expose XeF_2 to the sacrificial layer just below the movable membrane, release holes were opened in a portion of the movable membrane using a plasma dry cleaner (PX-250M, SAMCO). XeF_2 was exposed to the sensor chip using a Si etch device (Xactix, Xetech E1- β) without removing the photoresist used for this opening. Since the upper half-mirror was covered by the photoresist and the lower mirror by a SiO_2 film that acted as a protective layer against XeF_2 , and the sidewalls of the sacrificial layer were covered using a silicon nitride film, XeF_2 selectively etched the sacrificial layer Si immediately below the deformable membrane through the release holes, and the air gap was formed.
- (f) The photoresist on top of the deformable membrane was dry-etched using a plasma dry cleaner. In this process, both the photoresist and the parylene C of the deformable membrane were etched in the same way; thus, parylene C was deposited on the film with a thickness of approximately 20 nm larger than the design value to compensate for the decrease in film thickness.

In this fabrication process, appropriately designing the thickness of the SiO_2 in (b) and the silicon nitride film in (c) was important. The prototype MEMS interferometer did not have a silicon oxide film on the lower Au mirror and the silicon nitride film was deposited with a thickness of 300 nm. Since the thickness of the silicon nitride film was equivalent to the thickness of the sidewall, which served as a side stopper during the etching of the sacrificial layer, this thickness caused the sidewall to break before the sacrificial layer of a MEMS optical interferometer with a 100 μm diameter sensing area was completely etched, causing XeF_2 to leak out of the sensor (Fig. 2.10). In the etching of the sacrificial layer, only a sensor with a sensing area diameter of 50 μm could be formed without destroying the sidewalls, and its cross-sectional structure was observed using a scanning electron microscope, which revealed that the lower Au mirror was etched by XeF_2 for 22 nm (Fig. 2.11). Therefore, by changing the thickness of the silicon nitride film to 500 nm and depositing a SiO_2 film on the lower Au mirror using a low-temperature deposition method, we successfully formed a MEMS interferometer with a sensing area of 100 μm in diameter while maintaining the reflectivity of the Au mirror (Figs. 2.12–13).



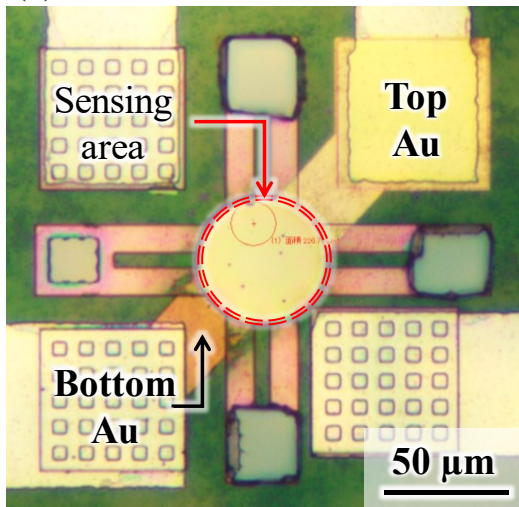
Figures 2.9: Process overview. (a) Patterning a bottom Au half-mirror using a lift-off process. (b) Deposition of SiO_2 to cover the bottom Au half-mirror. (c)

Patterning a sacrificial layer to form a trench and cover with Si_3N_4 passivation layer. (d) Deposition of parylene C with a top Au half-mirror for the movable membrane. (e) Removing the sacrificial layer by using XeF_2 to form a free-standing structure. (f) Finally, removing photoresist by using O_2 plasma ashing.

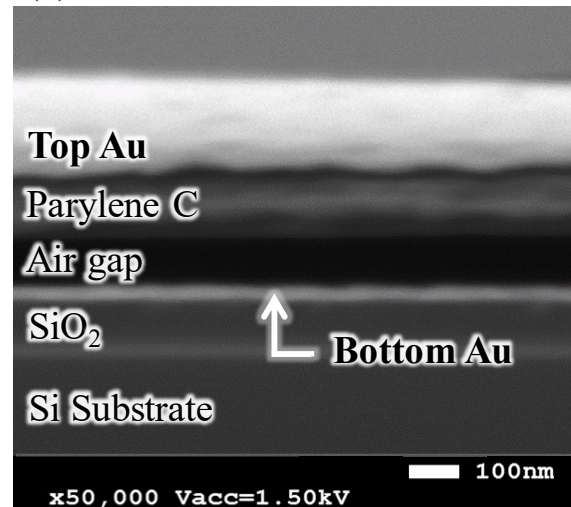


Figures 2.10: The process of sacrificial layer etching with XeF_2 before process improvement. The sidewalls of the sacrificial layer are broken and XeF_2 is leaking out of the sensor.

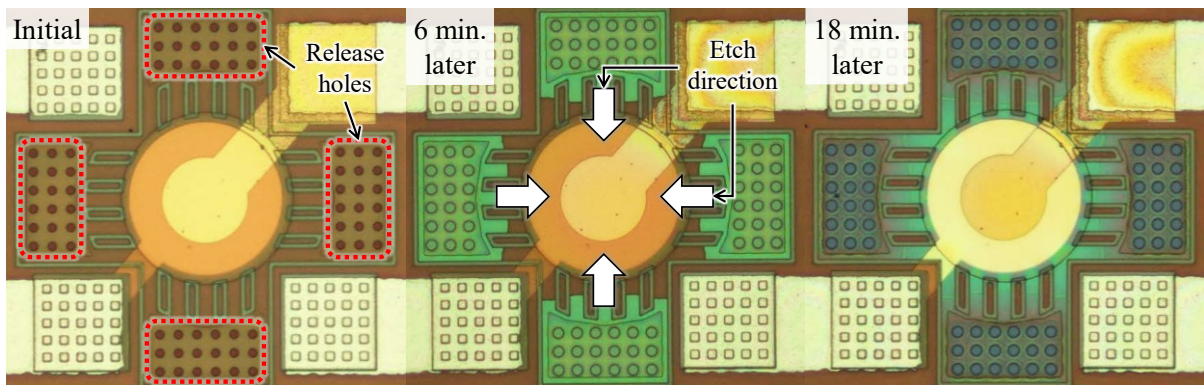
(a)



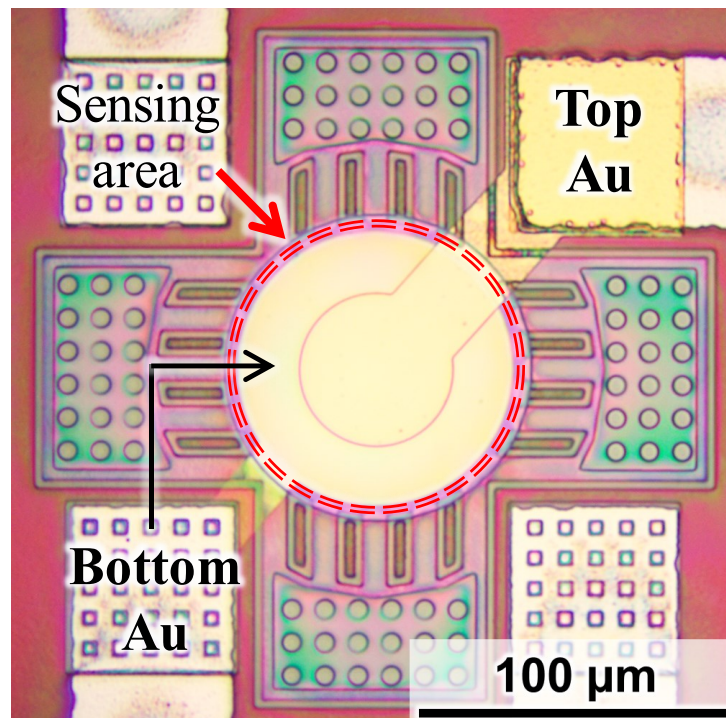
(b)



Figures 2.11: The fabricated prototype MEMS interferometer. (a) Optical micrograph and (b) cross-sectional SEM photograph. The lower part of the Au mirror is etched by XeF_2 .



Figures 2.12: The process of sacrificial layer etching using XeF_2 after process improvement. By changing the thickness of the silicon nitride film and depositing the SiO_2 film on the lower Au mirror, only the sacrificial layer is etched without XeF_2 leaking out of the sensor.

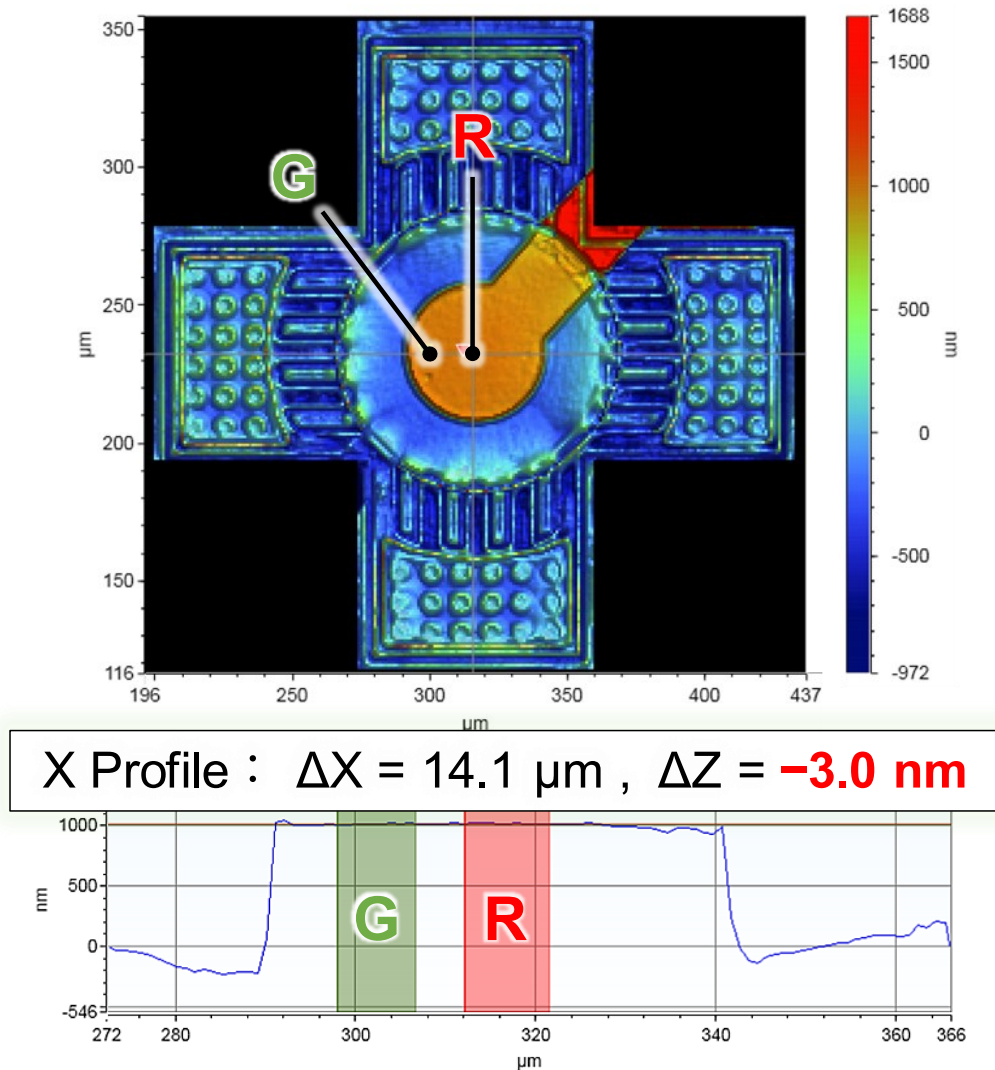


Figures 2.13: Optical micrograph of the fabricated MEMS interferometer. Changing the thickness of the silicon nitride film that serves as the sidewall of the sacrificial layer and depositing a silicon oxide film on the lower Au mirror, the MEMS optical interferometer was successfully formed while maintaining the reflectivity.

2.5 Fabrication Results

2.5.1 Structure and geometry evaluation

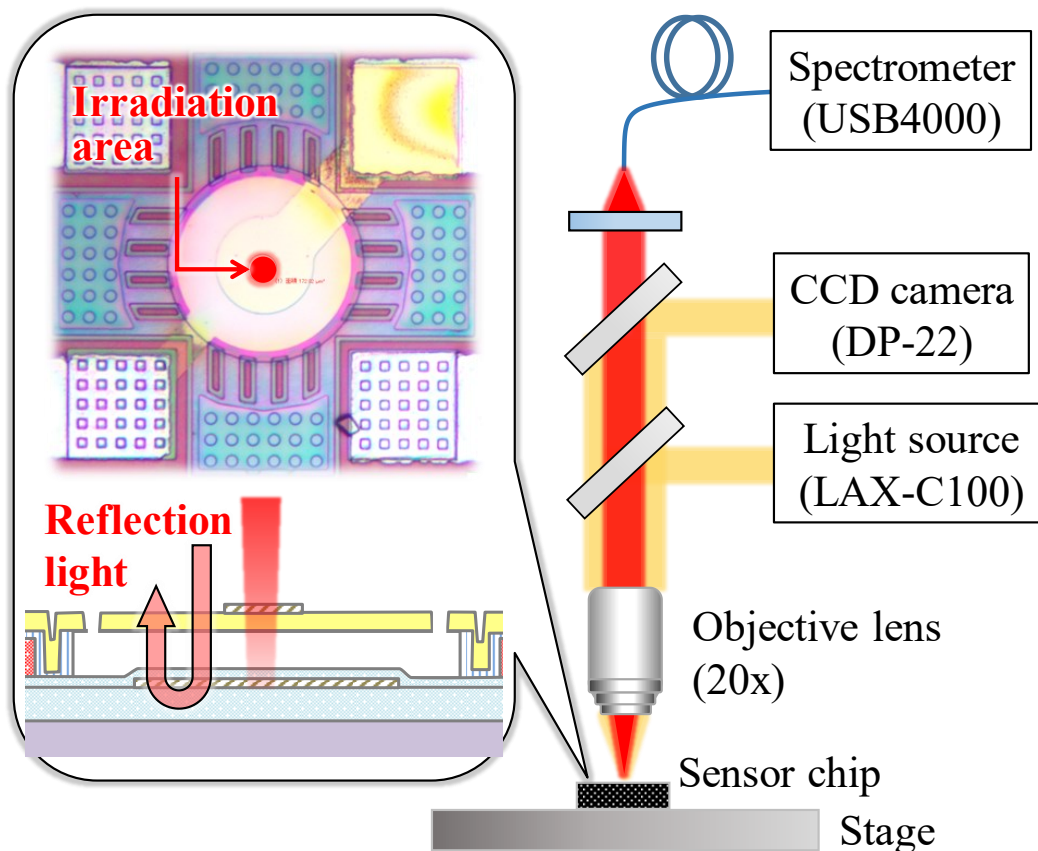
To evaluate the flatness of the deformable membrane with the thin Au layer, we measured the surface profile using a white light interferometric microscope (ContourGT-K, Bruker Nano Inc.) (Fig. 2.14). The height difference between the centre and edge of the mirror was observed to be 3 nm. This result almost corresponded to the 2.5 nm in the analysis of the difference in the amount of deformation in the centre and near the edges of the mirror in Section 1.2.2, which indicated that a very flat mirror was formed on the deformable membrane. Thus, this suggested that the fabricated interferometer can sufficiently reduce the change in the optical path length of the optical interferometer owing to the position of the light irradiation.



Figures 2.14: Surface profile of Au half-mirror formed on a freestanding structure

2.5.2 Evaluation of wavelength selectivity

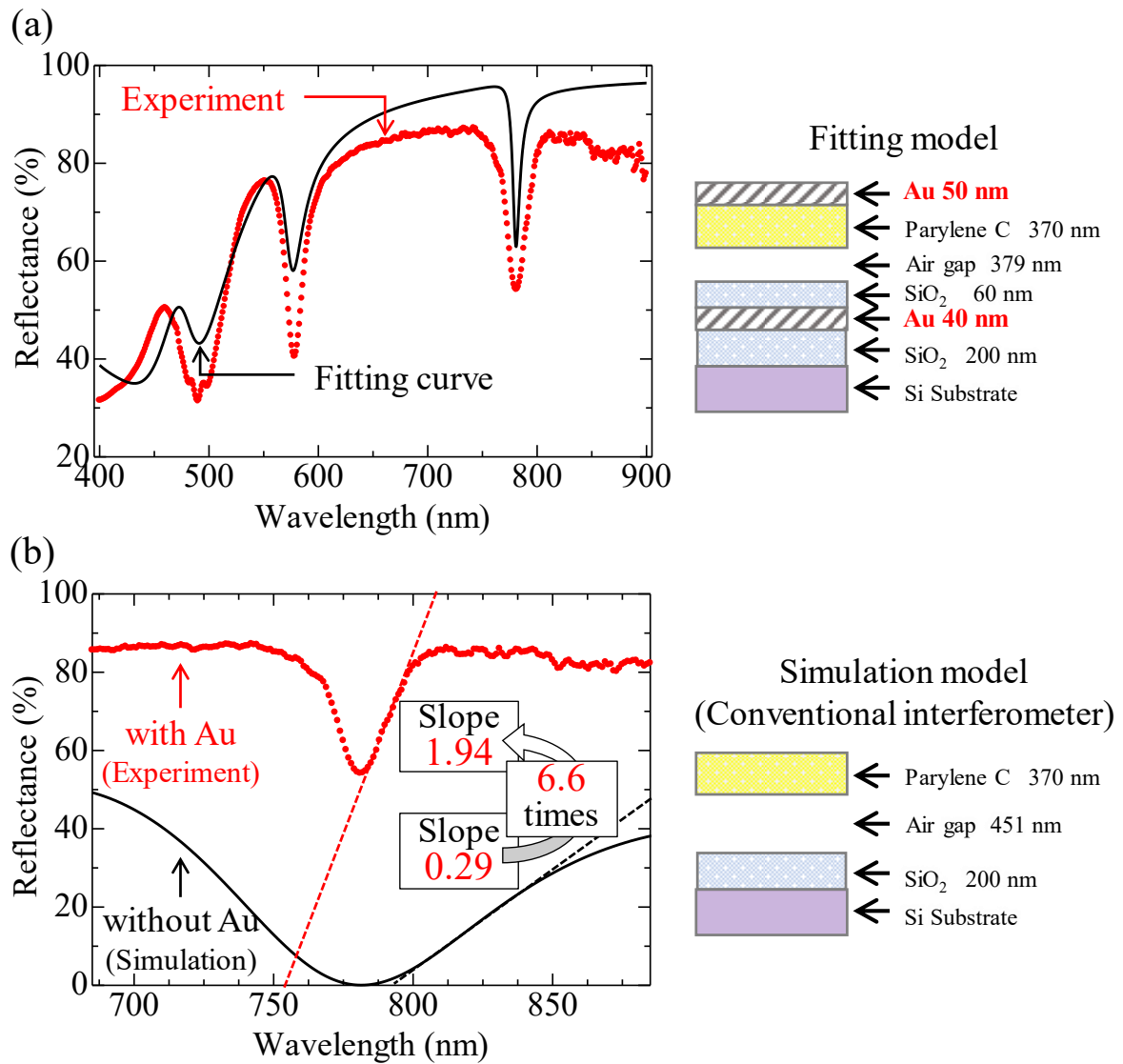
The wavelength selectivity of an optical interferometer formed on the silicon substrate can be evaluated through a spectroscopic measurement of the reflected light when white light is irradiated onto the sensing area and calculating the slope of the reflection spectrum. As shown in Fig. 2.15, in this experiment, a spectrometer (Ocean Optics USB4000) and a xenon light source (Asahi Spectra LAX-C100) were used, and the optical fibre diameter was adjusted to 100 μm , and a 20 \times objective was used to enable a light with a spot diameter of 5 μm to be irradiated on the upper Au mirror.



Figures 2.15: Experimental setup for evaluation of wavelength selectivity of the fabricated interferometer.

Fig. 2.16a shows the result of spectral characteristics of the fabricated MEMS interferometer using the above measurement system. Three sharp valleys caused by optical interference were observed to be near 490, 580, and 780 nm, which were in good agreement with the simulation curve using an air gap of 379 nm. Fig. 2.16b compares the slope on the reflection spectrum between the Au mirror-implemented sensor and a conventional one in the near-infrared wavelength range.

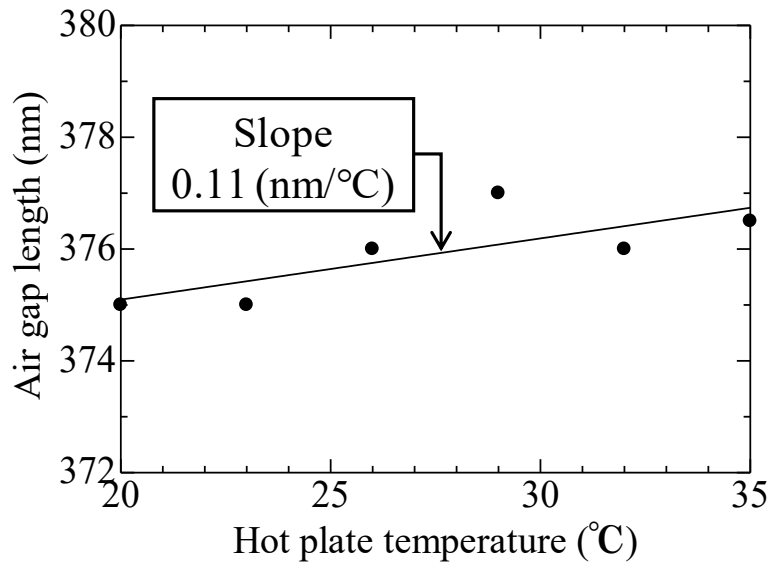
The comparison of the reflection spectral gradients between them indicated that the gradient of the spectrum increased by 6.6 times, which meant that the wavelength selectivity of the sensor increased by 6.6 times. Compared with the analysis of the spectral gradient in Section 1.2.1, the value was 62% of the design value. An important parameter to determine the reflection spectral gradient of the interferometer is the thickness of the Au mirrors above and below the deformable membrane. The thicknesses of each material that constituted the fabricated interferometer were in good agreement with the optical analysis results using the analytical model shown in Fig. 2.15(a), and the thicknesses of the films were 20 nm larger for parylene C, 29 nm larger for the air gap and 10 nm larger for the SiO₂ film on the lower Au mirror, and the lower Au mirror was 10 nm thinner than the design film thickness. This 10-nm error during bottom Au mirror deposition caused a deviation from the design value; thus, by decreasing the deposition rate, an Au mirror close to the design film thickness could be formed, which was expected to increase the wavelength selectivity of the MEMS optical interferometer.



Figures 2.16: Result of spectroscopic measurement of the fabricated MEMS interferometer. (a) Comparison of measured (red, dots) and analyzed (black, solid line) values at 400-900 nm wavelength range. (b) Comparison of the reflection spectral gradients of a conventional structure without mirrors (black, solid lines) and a structure with integrated Au mirrors (red, dots) in the near-infrared wavelength region.

2.5.3 Effect of change in temperature

Fig. 2.17 shows the result of the air gap change of the MEMS optical interferometer obtained from optical analysis when the fabricated chip was placed on a controllable digital hot plate with a resolution of 0.1 °C and the temperature was changed under a room-temperature environment (20 to 35 °C). The increase due to the air gap or parylene C expansion with temperature change was 0.11 nm/°C, and the optical path length increased up to 2 nm. Under this temperature environment, since the membrane deformation amount at the time of molecular adsorption was several tens of nm, the drift due to temperature change was considered to be negligible. In addition, even when the deflection of the deformable membrane occurred with no involvement of antigen–antibody reactions such as temperature and pressure change, the effect could be eliminated through a comparison with a reference sensor which was not immobilized with antibodies.



Figures 2.17: Impact of change in temperature to the air gap of fabricated interferometer.

2.6 Conclusion

In this chapter, the design and fabrication of the MEMS interferometer with Au half-mirrors structure are presented, and the increase in wavelength selectivity is discussed. The key points of this chapter are as follows:

【Optical design and analysis results using the finite element method】

1. The wavelength selectivity in the near-infrared region can be increased by 10.7-fold by forming 50 nm-thick Au half-mirrors on the top and bottom of the deformable membrane in the MEMS interferometer.
2. When the Au mirror at the top of the deformable membrane is formed with a coverage of 10% for the sensing area, the decrease in the deformation can be suppressed to approximately 6%, which confirms that only the wavelength selectivity can be increased without decreasing the surface-stress sensitivity by designing the appropriate coverage of the upper half-mirror.
3. Since the area on the deformable membrane covered by the Au mirror increases the rigidity of the film and the mirror supports the membrane, the difference between the amount of deflection in the centre of the deformable membrane and edge was observed to be 2.5 nm.
4. When the air gap is increased by up to 10 nm, the transmission intensity change of 52.93% is obtained for the Au-mirrored structure, which is estimated to improve the output response to the small deflection of the deformable membrane.

【Fabrication results】

1. By measuring the surface profile of the Au mirror at the top of the fabricated MEMS interferometer, the maximum height difference between the centre and the edge of the mirror was observed to be 3.0 nm. This value was in good agreement with the analytical value, confirming the formation of a very flat mirror.
2. The wavelength selectivity of the interferometer was confirmed to be 6.6 times higher than that of a conventional interferometer with no mirrors by measuring the slope of the reflection spectrum when the light was irradiated on the fabricated MEMS interferometer.

Chapter 3. Acquisition of sensor response for detecting proteins in liquid

3.1 Preface

For conventional MEMS interferometers without metal mirrors, diX-AM, an organic film with an amino group on the side chain, is deposited on the sensor using CVD and antibody molecules are adsorbed through electrostatic interaction. In contrast, the MEMS interferometer with Au mirrors can immobilize antibody molecules through self-assembled monolayers widely used in QCM and SPR biosensors, which utilize Au as a molecular adsorption layer. Since this technique permits the selective adsorption of antibody molecules on Au simply by immersing the sensor chip in a specific solution, productivity can be improved and the cost of the molecular immobilization process can be decreased.

In the experiment described in this chapter, we aimed to obtain the sensor response because of the adsorption of target molecules. First, a method of antibody modification using self-assembled monolayers on the upper Au mirror is described. Next, in the interferometer with a constructed bio-interface, we performed an experiment to acquire the response caused by antigen–antibody reactions. Third, the possibility of selective detection of the target molecule is discussed by comparing the amount of deflection between the target adsorption and non-specific adsorption. Finally, based on the results of this study, the recent research by our research group on a MEMS interferometer with enhanced surface-stress sensitivity to detect lower concentrations of proteins is introduced.

3.2 Consulting bio-interface onto top Au mirror

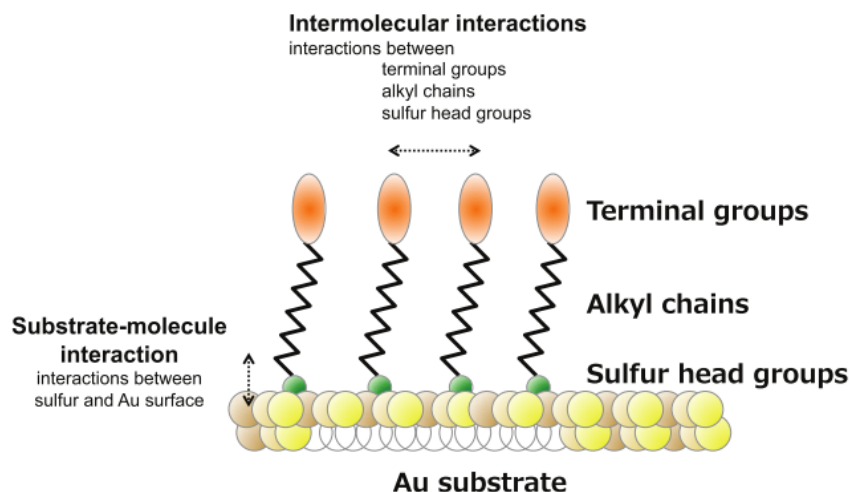
3.2.1 Molecule modification using self-assembled monolayers

Self-assembled monolayers (SAMs) are organic thin films with a thickness of several nanometres. When a chip is immersed in a solution of organic molecules with a high affinity for a particular substance, the organic molecules are chemically adsorbed on the surface of the chip. These are known that Van der Waals forces, and hydrophobic interactions between adsorbed molecules in the process result in a more aggregated action of the molecules, resulting in the formation of an oriented monolayer [69]. It has a high affinity for devices fabricated using MEMS technology because it can be covered regardless of the

surface shape if a gap (a few nanometres) exists for the adsorbed molecules to penetrate.

The molecules that form the SAM have long-chain alkyl groups between the sulfur atoms on the adsorbed substrate side and the terminal functional groups, (Fig. 3.1), and one pair of methylene units (-CH₂-) comprising this alkyl group corresponds to a film thickness of 0.2 nm. Au is often used for adsorbing substrates because sulfur atoms have a high affinity for transition metals and chemisorb strongly on metal surfaces. Using this mechanism, an interface that can capture antigen molecules on the sensor can be constructed by forming SAM on the fabricated MEMS interferometer followed by attaching antibodies to the terminal functional groups.

The proposed sensor increases the adsorption density of target antigen molecules by increasing the immobilization density of antibody molecules, and the distance between adsorbed molecules is shortened. Since the Coulomb repulsive force acting between adsorbing molecules is inversely proportional to the square of the distance between the molecules, the increase in charge density within the micro-region on the interferometer can be expected to increase the amount of deformation of the deformable membrane. Because the antibody molecule binds to the SAM-terminal functional group and is anchored on the sensor, the immobilization density of antibodies that form on the interferometer must be increased. The addition of CF₃COOH to the organic solvent during SAM formation has been reported to be an effective method [70]. In conventional SAM formation methods, SAMs with carboxyl groups at the ends are bonded to each other through hydrogen bonding, forming a region on the SAMs that cannot be modified by the molecule, and this is a factor that reduces the immobilization density of antibody. CF₃COOH prevents the de-ionization of the molecules at the end of the SAM, creating an electrostatic repulsion between the end molecules and preventing hydrogen bonding, which is considered to prevent the SAMs from binding to each other. Therefore, to demonstrate the effectiveness of this technique in the MEMS interferometer, we discuss the results of our investigations to improve the immobilization density of antibodies in the next section.



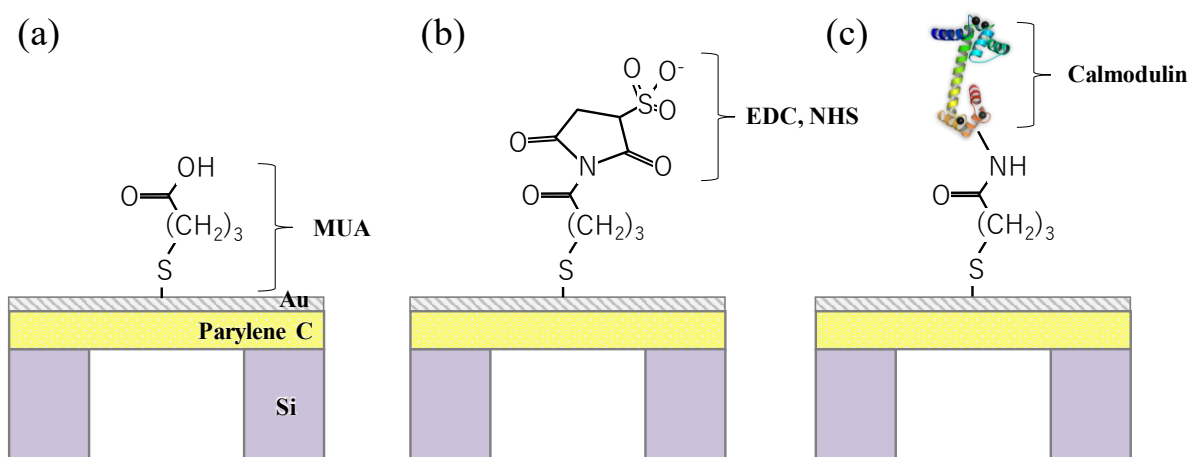
Figures 3.1: Conceptual diagram of self-assembled monolayer formed on Au [69].

3.2.2 Formation of SAMs and evaluation of surface condition of sensor

Fig. 3.2 shows the cross-sectional structure of a chip in the SAM formation and immobilization procedure of macromolecules. The chip that forms the SAM has a structure that reproduces the upper mirror of the MEMS interferometer by forming a through-hole on the backside of the Si substrate using a deep reactive-ion etching (RIE) device (MUC21-RD, Sumitomo Precision Products), depositing deformable membrane of parylene C and Au, followed by etching the bulk Si with XeF_2 . The immobilization procedure of SAM and macromolecule is as follows:

- (a) Surface contaminants of the chip are removed using a low-pressure plasma device or UV ozone cleaner as preparation for molecular immobilization. This process generally involves cleaning with sulfuric acid (piranha cleaning). However, in actual sensors, since the Al wiring is etched, a dry cleaning process with fewer effects is selected. After removing any contaminants on the Au surface using UV ozone, a SAM is formed on the Au surface by immersing the sensor chip for 19 h in mercaptoundecanoic acid (MUA) and a CF_3COOH in ethyl alcohol and rinsed in 10% (v/v) $\text{NH}_3\text{-H}_2\text{O/EtOH}$. To indicate that the addition of CF_3COOH increases the immobilization density of SAMs, a separate chip with SAMs on the chip without the addition of CF_3COOH was prepared and the subsequent molecular modification process was also performed under the same conditions.

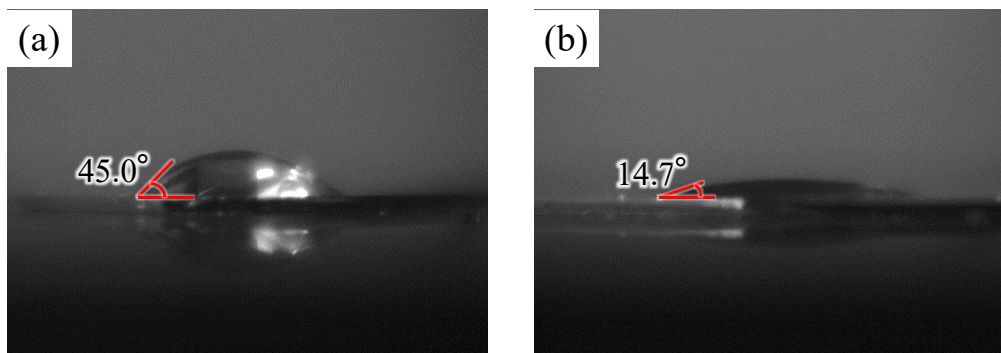
- (b) The carboxyl group of MUA was activated in a 50 mM 4-morpholinepropanesulfonic acid (MES) buffer solution (pH 5.5) with 1-ethyl-3-(3-dimethylaminopropyl) carbodiimide hydrochloride (EDC) and N-hydroxysuccinimide (NHS) for 30 min and washed in MES buffer solution. When applying a cross-linking reaction, the addition of NHS to EDC forms a highly stable NHS ester. This reaction pathway activates the carboxyl group at the end of the SAM and facilitates the binding of the macromolecule via amide bonds.
- (c) The sensor chip was immersed in MES buffer with the calcium-binding protein calmodulin (2 mg/mL) as a model protein molecule for 3 h, then it was rinsed with MES buffer. In this molecular modification process, based on the report of Gao *et al.* [71], who performed molecular modification using a SAM on a surface-stress sensor, calmodulin, a calcium-binding protein, was adsorbed after SAM formation, but this molecular modification process can also be applied to antibody molecules.



Figures 3.2: Cross-sectional structure of the sensor chip and molecular immobilization procedure on Au surface. (a) After SAM formation. (b) After adding crosslinker of EDC and NHS. (c) After calmodulin adsorption.

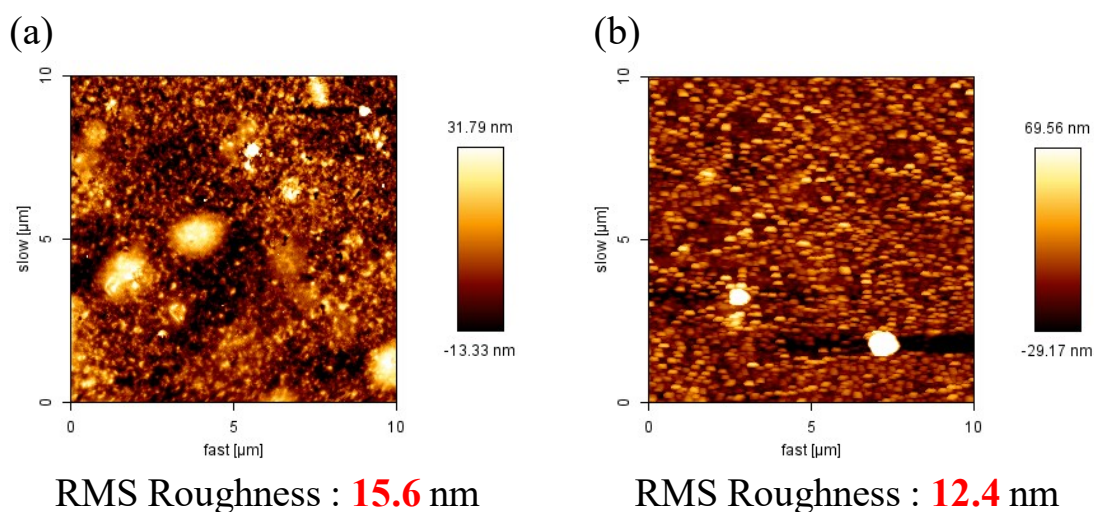
Fig. 3.3 shows a comparison of the contact angle between chips with and without CF_3COOH when 5 μL of DIW was dropped after SAM formation in process (a). If the carboxyl groups at the SAM ends are not bonded to each other, the hydrophilicity increases and the contact angle is smaller. If they are bound, the terminal of SAM becomes a thiol group; therefore, the hydrophilicity decreases and the contact angle to the carboxyl group increases. Since the contact angle was

observed to be approximately 30° smaller for the CF_3COOH -added chips, the results suggested that the binding between SAMs is suppressed and a uniform SAM is formed on Au.



Figures 3.3: Contact angle comparison between (a) conventional method and (b) method using CF_3COOH when dropped DI water.

Fig. 3.4 shows the surface condition in a $10\ \mu\text{m} \times 10\ \mu\text{m}$ chip captured using atomic force microscopy to observe its surface after adsorption of calmodulin in process (c). On the surface of the chips with CF_3COOH , the molecules were agglomerated without gaps, while on the surface of the chips without CF_3COOH , the molecules were adsorbed irregularly, and the root-mean-square roughness of the former was observed to be $3.2\ \text{nm}$ lower than that of the latter. These results suggested that the immobilization density of the SAM formed on Au increased, indicating that the immobilization density of the SAM on the upper Au mirror of the MEMS interferometer could also be increased and that the macromolecules can be bound through the SAM.

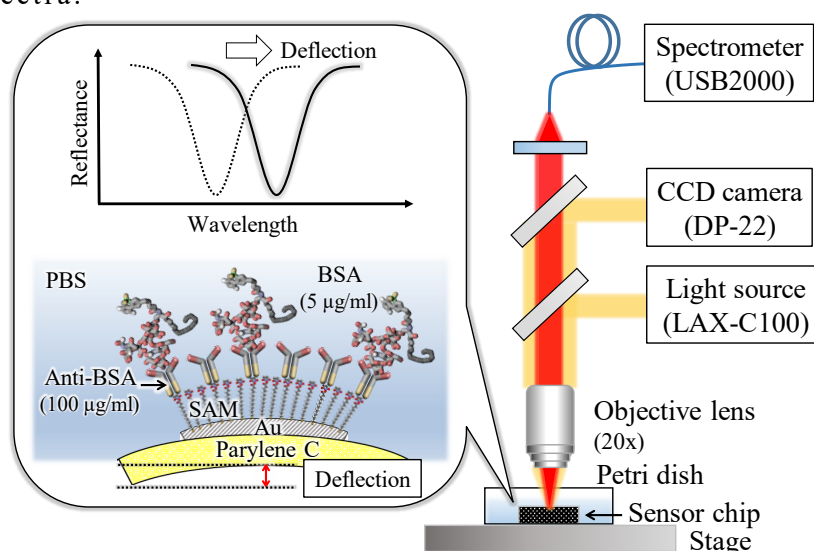


Figures 3.4: Surface roughness comparison between (a) a conventional method without CF_3COOH and (b) a method with CF_3COOH after calmodulin adsorption.

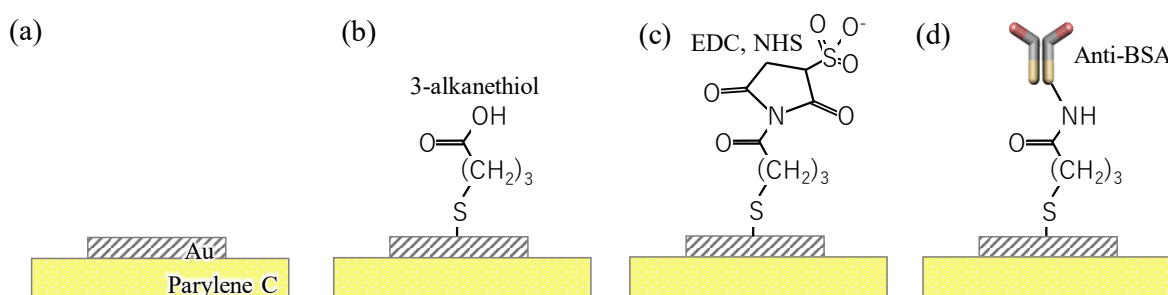
3.3 Acquisition of the response by antigen–antibody reaction

3.3.1 Evaluation of deflection amount by spectroscopic measurement

To obtain the sensor response during the antigen–antibody reaction with the fabricated MEMS interferometer, bovine serum albumin (BSA) antibodies were immobilized to the terminal molecule of the SAM, and the amount of deflection of the deformable membrane caused by the adsorption of BSA antigen molecules was evaluated using spectroscopy. As shown in Fig. 3.5, based on the experimental setup described in Section 2.4.2, spectroscopic measurements were performed by placing a petri dish filled with PBS onto the stage of a microscope and irradiating light to the sensing area while the sensor chip was immersed in this solution; subsequently, the reflected light was guided to the monochromator to acquire the reflection spectra.



Figures 3.5: Experimental setup for spectroscopic measurement and schematic diagram of antigen-antibody reaction on the sensor in liquid.



Figures 3.6: Immobilization procedure of BSA antibody molecule onto the fabricated MEMS interferometer. (a) Before molecule immobilization. (b) SAM

formation. (c) Functionalization by crosslinker of EDC and NHS. (d) Adsorption of BSA antibody molecule.

Based on the molecular modification procedure described in Section 3.3.2, the bio-interface shown in Fig. 3.6d with a concentration of 100 $\mu\text{g}/\text{mL}$ BSA antibody adsorbed via SAM onto an upper Au mirror was constructed. Fig. 3.7a shows the reflection spectra obtained when the sensor chip was immersed in PBS with a BSA antigen concentration of 5 $\mu\text{g}/\text{mL}$.

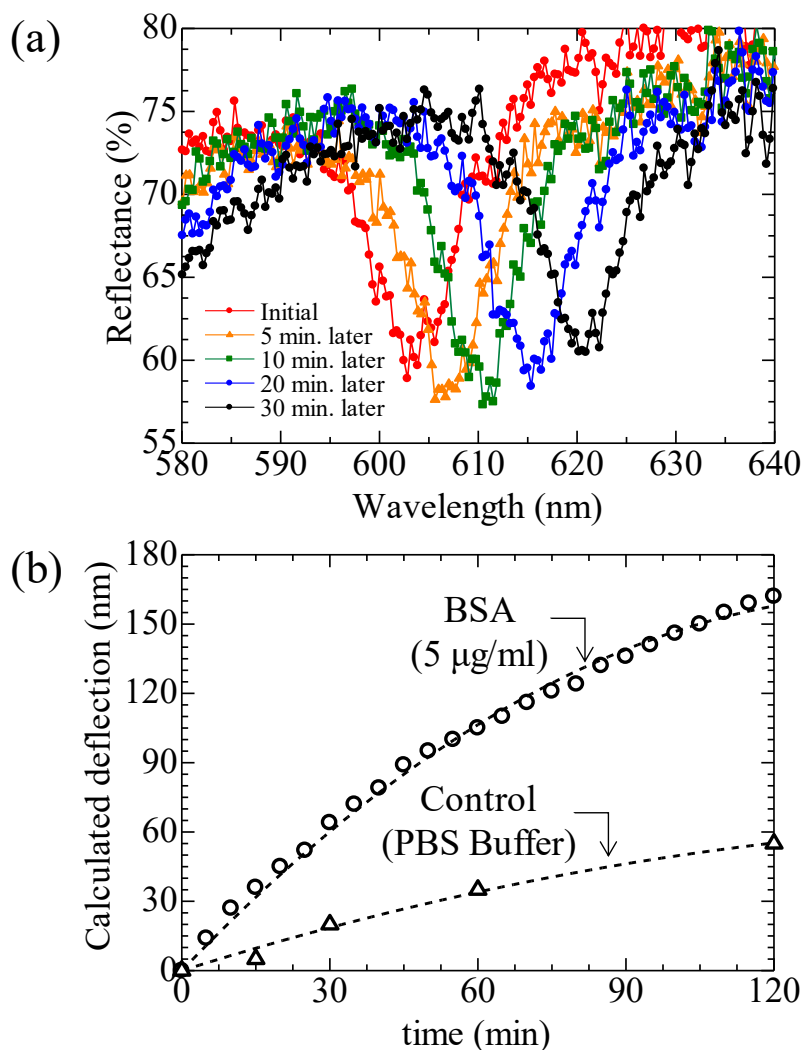


Figure 3.7: (a) Typical spectral shift caused by BSA antigen–antibody reaction on the MEMS interferometer and (b) time course of the deflection of deformable membrane calculated by optical analysis.

The change in the reflectance at approximately 600 nm was 5.5% after 5 min and 13.6% after 10 min, which was equivalent to the transmittance change to the substrate. Additionally, the deformation of 64 nm was observed to occur in 30 min

when the deflection of the membrane obtained was calculated using optical analysis from the wavelength shift because of the antigen–antibody reaction of the BSA. In the paper previously reported by our group [72], we have demonstrated an electrical readout from an optical interferometric surface-stress sensor which readouts voltage by impedance conversion using a source follower circuit from the output current of a MEMS optical interferometer integrated with a photodiode, and a voltage change of approximately 1 V was obtained through a decrease in the transmission intensity (an increase in the reflection) associated with 50 nm-deflection of the movable membrane. Because the deflection amount was larger than our previous report, we expected that a sufficient electrical readout signal can be obtained through antigen–antibody reactions.

Moreover, through a negative control experiment, we observed that membrane deflection due to the reflection wavelength shift also occurred when the chip was immersed in PBS without a BSA antigen. As shown in Fig. 3.8, since the sensor used in the experiments did not seal the release holes opened during the formation of the freestanding structure of the interferometer, the liquid diffused into the air gap of the interferometer when the chip was immersed in PBS. Since the SiO₂ film formed by electron beam (EB) deposition on the Au mirror at the bottom of the deformable membrane is a highly hygroscopic material, it swells with the diffused liquid and changes the effective refractive index. We considered that this effect causes a spectral shift in the reflection light because of an increase in optical path length at the SiO₂ layer even in the absence of deflection of membrane. Because the fluctuation in reflectance tends to become saturated after immersing in PBS for 1 h, this effect can be reduced by beginning measurements after ageing occurs.

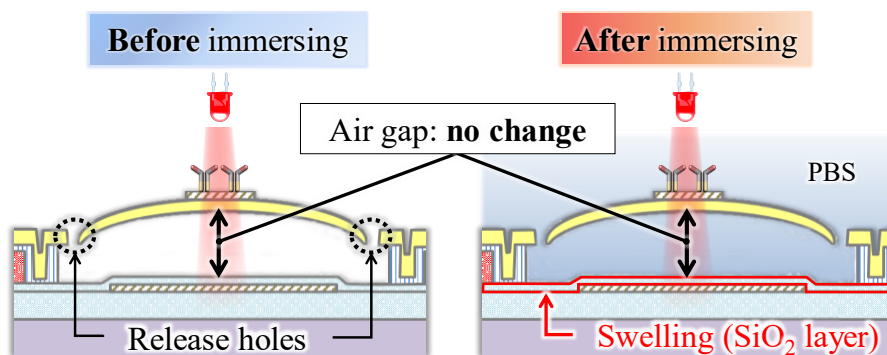


Figure 3.8: Schematic diagram of cross-sectional structure of the MEMS interferometer used the experiment. The swelling of SiO₂ occurs due to PBS entered in the air gap.

3.3.2 Selective detection of antigen molecules

To evaluate the response of the sensor in the BSA antigen and nonspecific binding, we used streptavidin molecules with molecular weights of 67–68 kDa, which are equivalent to the molecular weight of BSA molecules of 66 kDa, and the bio-interface was constructed using casein, which is the main component of skim milk, as a blocking agent to suppress the effect of non-specific adsorption. Based on the molecular immobilization procedure described in the previous section, BSA antibodies were immobilized on a SAM and rinsed in PBS. The sensor chip was then immersed in PBS containing casein (5% w/v) for 1 h and rinsed again with PBS to construct the molecular adsorption layer on the MEMS interferometer (Fig. 3.9).

After the chips were immersed in PBS for 1 h to remove the effects of fluctuation of reflectance, the BSA and avidin solution were added to bring the final concentration of the BSA and avidin to 10 and 100 ng/mL, respectively. Fig. 3.10 shows the time course of the deflection of the deformable membrane calculated from the reflection spectra from the BSA antigen–antibody reaction and avidin nonspecific adsorption. When PBS with streptavidin molecules were added, there was almost no deflection change, while the deflection increased by 17.5 nm for 10 min when PBS with BSA antigen molecules added. Only the BSA antigen molecules in PBS were captured by the BSA antibodies by the antigen–antibody reaction, the membrane was considered to deflect upward because the increase in surface stress transferred to the deformable membrane. These results suggested that the fabricated MEMS interferometer can be used for selective detection of target antigen molecules.

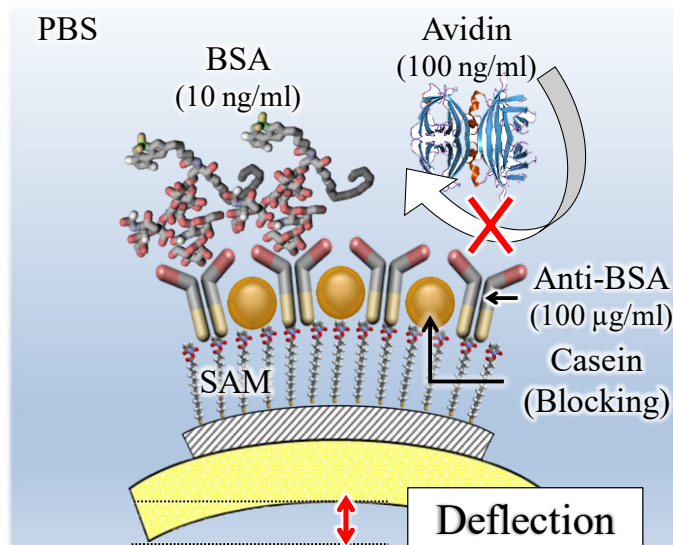


Figure 3.9: Schematic view on the Au mirror after immobilization of antibody molecules. Comparing the amount of deflection that occurs during the antigen-antibody reaction with BSA and non-specific adsorption with strept avidin.

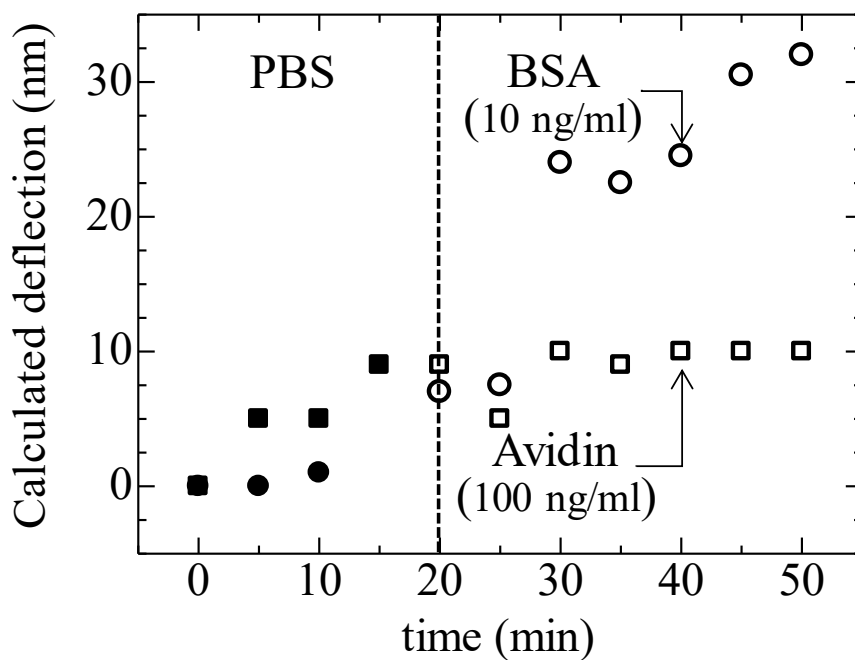


Figure 3.10: Comparison of the deflection amount of deformable membrane between addition of BSA and avidin molecule solution.

3.4 Acquisition of sensor output in the cavity-sealed MEMS interferometer with high surface-stress sensitivity

Based on the results of this study on molecular immobilization and the acquisition of the amount of membrane deflection by the antigen–antibody reaction, this section introduces recent research by our research group on the detection of lower concentrations of proteins in a MEMS interferometer with improved surface-stress sensitivity [73]. As shown in Fig. 3.11, the structure of the interferometer was formed using the dry transfer of a deformable membrane detached from different wafers to a chip and a cavity formed. The amount of deflection in a surface-stress sensor is inversely proportional to the Young's modulus and thickness of the deformable membrane and increases in proportion with the deformed area. Therefore, in the former, polymethyl methacrylate (PMMA), which has an order of magnitude lower Young's modulus than that of Au, was introduced as a molecular adsorption layer and the thickness of the deformable membrane decreased by 150 nm. In the latter, the surface-stress sensitivity was increased by extending the diameter of the deformable membrane to 300 μm . The MEMS interferometer with a cavity-sealed structure introduced in this section will be described in detail in Chapter 4.

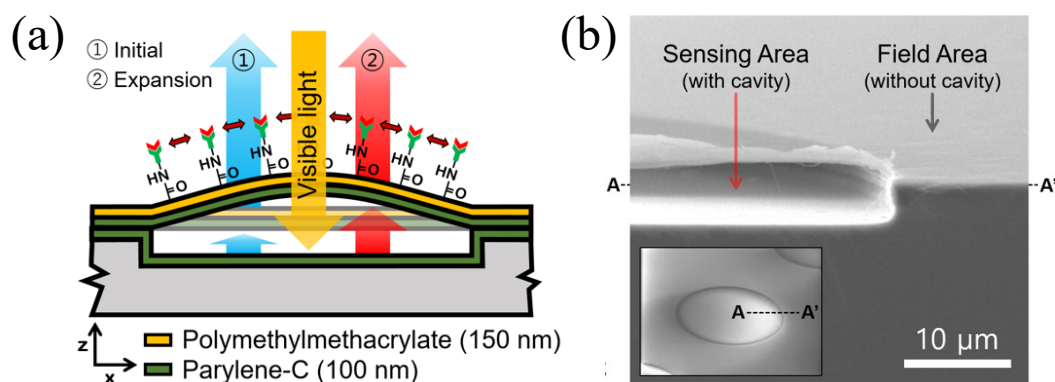


Figure 3.11: Cross-sectional view of the cavity-sealed interferometer. (a) Schematic diagram and (b) SEM image [73].

3.4.1 Immobilization of antibody molecules onto a sensor

In the molecular immobilization method introduced in Section 3.3, amine-reactive intermediates are formed by adding a cross-linker to the carboxyl group of the SAM-terminal, and the antibody molecules are immobilized by amide bonding. This immobilization method assumes that the surface state before the addition of the cross-linker is a carboxyl group. As shown in Fig. 3.12, the EDC/NHS cross-linked method cannot be applied to the PMMA in the molecular

adsorption layer because the terminal structure of PMMA is a methyl group. Therefore, we solved this problem by introducing a technique to oxidize PMMA using UV/O₃ treatment to change the terminal structure to a carboxyl group [74], and after immobilization of human serum albumin (HSA) antibodies, BSA was used as a blocking agent.

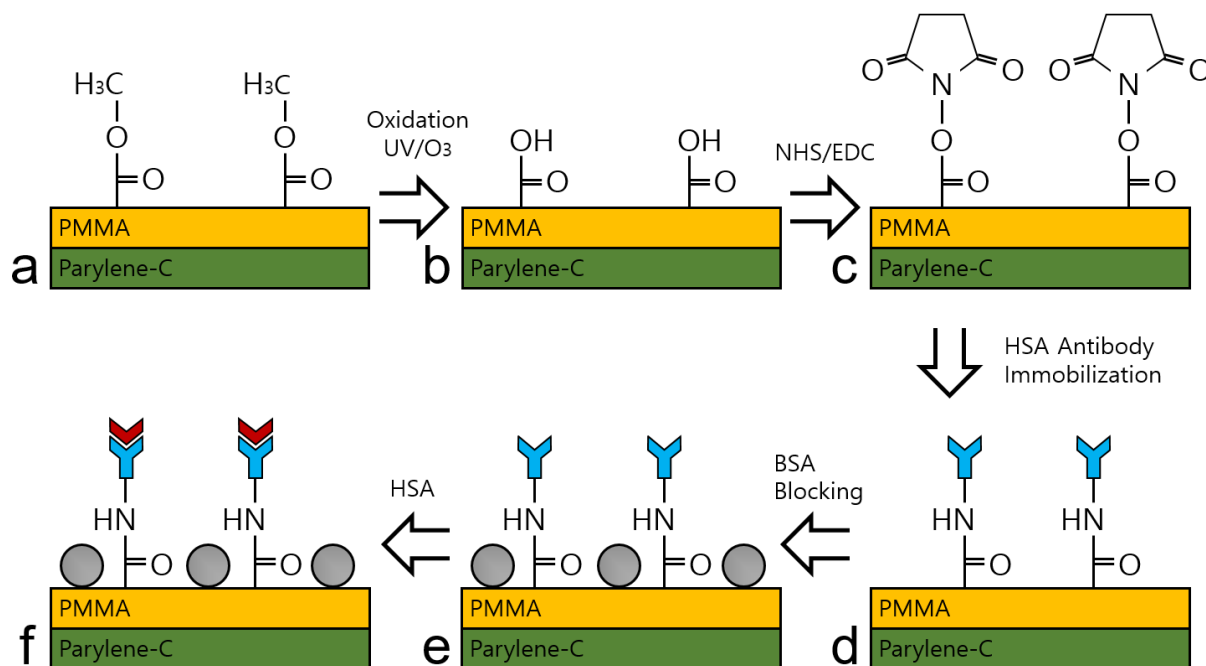


Figure 3.12: Immobilization protocol for detection of the HSA antigen using the fabricated sensor[73]. (a) Surface condition of as-fabricated sensor membrane. (b) Generation of carboxyl groups according to the oxidation process of the PMMA surface. (c) Surface activation by crosslinking treatment using EDC/NHS. (d) Immobilization of anti-HSA antibody. (e) Surface blocking treatment using BSA. (f) HSA antigen-antibody reaction.

3.4.2 Selectivity of the sensor

Fig. 3.13 shows the spectral shifts after 15 min of dropping HSA antigen at a concentration of 1 ng/mL to the sensor with HSA antibody molecules, or PBS, IgG, and streptavidin as negative controls. When PBS was added, a shift of 9.7 nm occurred because of a temporary pressure change by the PBS addition. The shifts were 8.7 and 10.9 nm for IgG and streptavidin, respectively. Since the shifts in the negative control were the same when PBS was added to the sensor, this suggested that the effect of physical adsorption is negligible. Furthermore, since the spectral shift of 31.2 nm for the HSA antigen drop was more than three times

greater than the response to the negative control, this indicated the selectivity of the sensor.

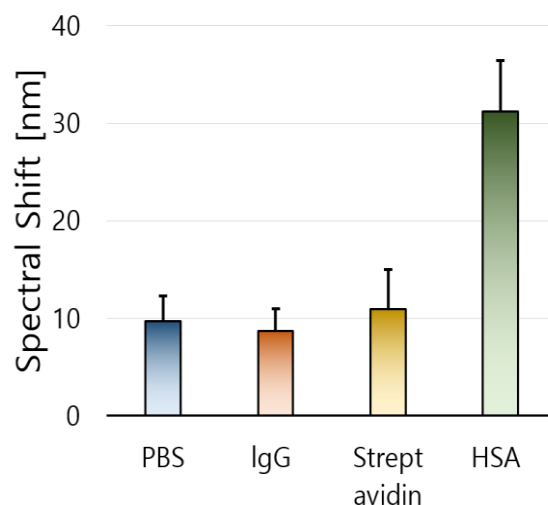


Figure 3.13: Molecular selectivity for 1 ng/mL IgG, 1 ng/mL Streptavidin, and 1 ng/mL HSA[73]. Response to PBS was obtained as a reference representing the physical response of the membrane. The reflection spectrum for each reagent was shifted by 9.7 nm, 8.7 nm, 10.9 nm, and 31.2 nm for 15 minutes.

3.4.3 Concentration dependence and limit of detection

In this experiment, the sensor was immersed in PBS for 30 min to stabilize the deflection of the deformable membrane because of pressure changes in the liquid. Fig. 3.14a shows the spectral shift caused by adding PBS with an HSA antigen to bring the final concentration to 100 ag/mL–1 ng/mL. At each final concentration, the amount of shift increased depending on the concentrations. In this experiment, each solution was added 3 min after the beginning of the measurement, and Fig. 3.14b shows the amount of peak shifts caused 15 min after the addition. Fig. 3.13c shows the calibration curve of the obtained spectral shifts. The coefficient of determination R^2 of the calibration curve was 0.976, which indicated that the calibration curve operated well. The amount of shift owing to physical effects (changes in liquid pressure or temperature) caused by adding PBS without HSA antigen was 8.1 nm. In contrast, since the shifts of 8.6 and 11.2 nm for the HSA antigen at a final concentration of 100 ag/mL–1 fg/mL, respectively, a large response compared with the response of PBS was obtained. In other words, this suggested that the detection limit of the HSA antigen in this sensor is 100 ag/mL–1 fg/mL. This result indicated that proteins can be detected at concentrations 200,000 times lower than the detection limit of 0.2–10 ng/mL [34], [65], [66] in

conventional MEMS surface-stress sensors. The LOD of digital ELISA, which is the most sensitive detection method using labelling agents, is 60 ag/mL [6], which is one order of magnitude smaller than our method; however, in semiconductor-based label-free biosensors, the most sensitive detection is possible.

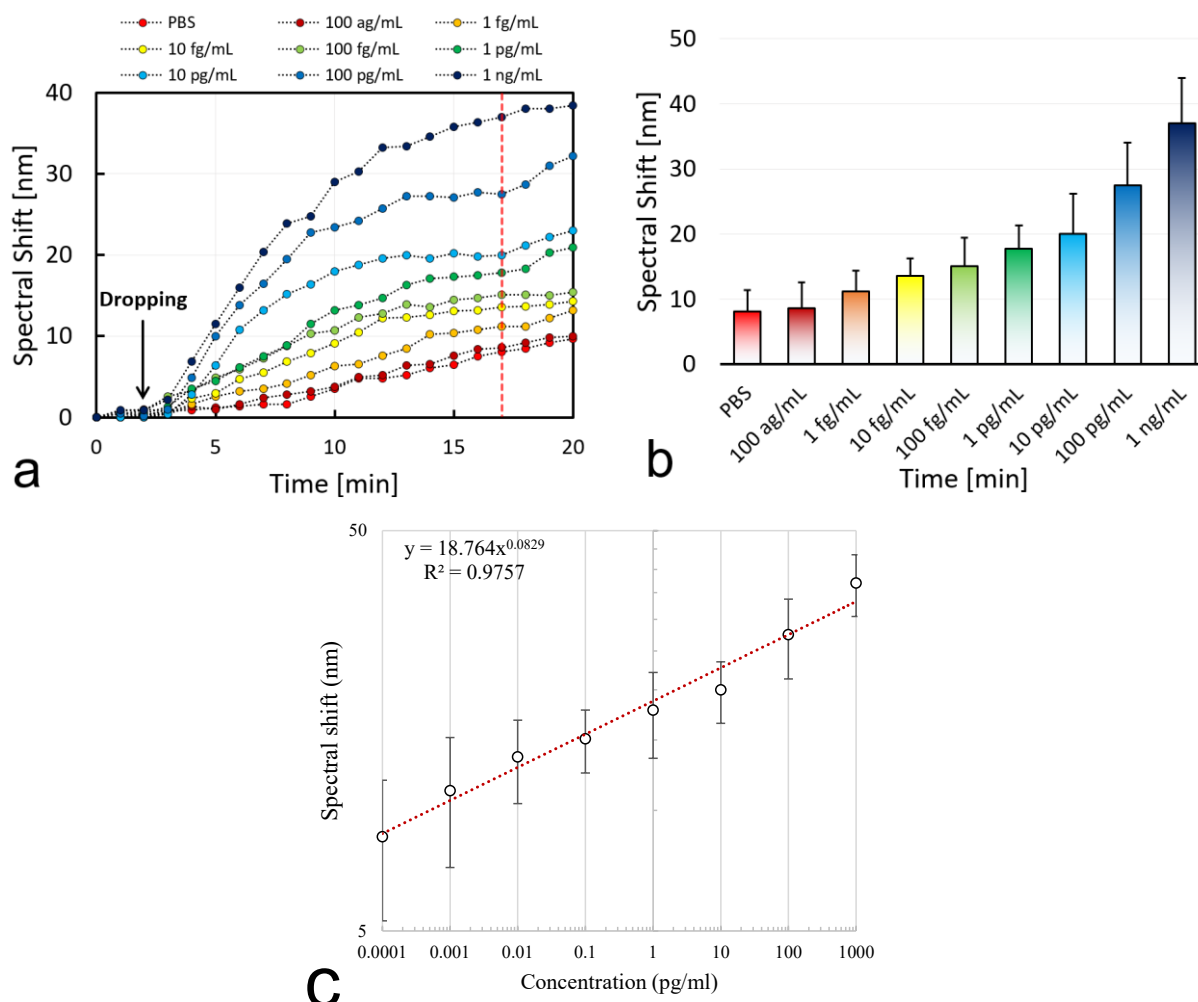


Figure 3.14: Spectral shift results after dropping PBS including no HSA and HSA at a final concentration of 100 ag ~ 1 ng/mL[73]. (a) The reagent was dropped at 3 minutes and the result of tracking the spectral shift for 17 minutes. (b) Spectrum shift was measured 15 minutes after dropping the reagent. (c) Calibration curve in the spectrum shift amount. Spectral shifts value were measured at 8.1 nm, 8.6 nm, 11.2 nm, 13.6 nm, 15.1 nm, 17.8 nm, 20 nm, 27.5 nm, and 37 nm for each reagent, respectively. The response at 1 fg/mL (15 aM) was significantly different from the physical response to PBS. (Error bar means standard deviation of 3 interferometers)

3.5 Conclusion

This chapter describes the construction of bio-interfaces that immobilize antibody molecules via a self-assembled monolayer on a MEMS interferometer with high wavelength selectivity, and the detection of macromolecular proteins using the antigen–antibody reactions is demonstrated. In addition, based on the results of this study, recent research by our research group on the detection of lower concentrations of macromolecular proteins in a MEMS interferometer with improved surface-stress sensitivity is introduced. The key points of this chapter are as follows:

【Investigation on improving the immobilization density of SAM】

1. The addition of CF₃COOH during SAM formation resulted in the formation of a uniform SAM on Au, and the root-mean-square roughness after macromolecules adsorption was reduced by 3.2 nm compared with the scenario of SAM formation without the addition.

【Experimental results】

2. By immersing the sensor with BSA antibodies at the terminal group of SAM in a BSA antigen solution at a concentration of 5 μg/mL, the deformable membrane was deformed by the antigen–antibody reaction to 64 nm in 30 min, resulting in a 13.6% change in transmitted light intensity that would be expected to be sufficient output current change if the photodiode was integrated.
3. When a BSA antigen and streptavidin solution was added to the sensor, which had BSA antibodies at the SAM-terminal to bring the final concentration to 10 or 100 ng/mL, respectively, the deflection of membrane only occurred in the former scenario, suggesting that the fabricated MEMS interferometer can be used for the selective detection of target antigen molecules.

【Research work by our research group】

4. The selectivity of the sensor was demonstrated by the amount of spectral shift caused by an HSA antigen at a concentration of 1 ng/mL being more than three times greater than the response to the negative control PBS, IgG and streptavidin (final concentration of 1 ng/mL).
5. The large response to the shift amount of PBS without HSA antigen was obtained at the final concentration of 100 ag/mL–1 fg/mL, suggesting that the LOD of the protein in this sensor was 100 ag/mL–1 fg/mL.

Chapter 4. Investigation of cavity-sealed MEMS interferometer with high surface- stress sensitivity

4.1 Preface

In the early fabricated interferometers with metallic half-mirrors structures, the sealing of interferometer was incomplete because of the constraints of the fabrication process. This makes obtaining responses from the adsorption of low concentration target molecules difficult. This is because suppressing the changes in effective refractive index is difficult because of the swelling reaction of the SiO₂ layer and non-specific adsorption of target molecules to the backside of the membrane. In addition, the stiffness of the deformable membrane owing to the Au mirror as a molecular adsorption layer increases, which results in a decrease in the surface-stress sensitivity. Therefore, a MEMS interferometer with cavity-sealed structure is proposed to prevent liquid from entering the interferometer. The results of the detection of proteins in the liquid using the interferometer with the cavity-sealed structure in our research group have already been presented in Chapter 3. Thus, in this chapter, considering the application to the detection of gas molecules in the air, we propose a polymer membrane which can be used to detect gas molecules in air and proteins in liquids. Next, to increase the surface-stress sensitivity of the interferometer, the effects of reducing the Young's modulus and thickness of the deformable membrane are calculated using finite element analysis. In addition, to improve the spectral response to the deflection of the deformable membrane, the effect of narrowing the air-gap length of the interferometer is calculated using optical analysis. Finally, we describe the fabrication process of the MEMS interferometer that reflects the knowledge obtained from these designs and present the results of obtaining the reflection spectra of the fabricated interferometer.

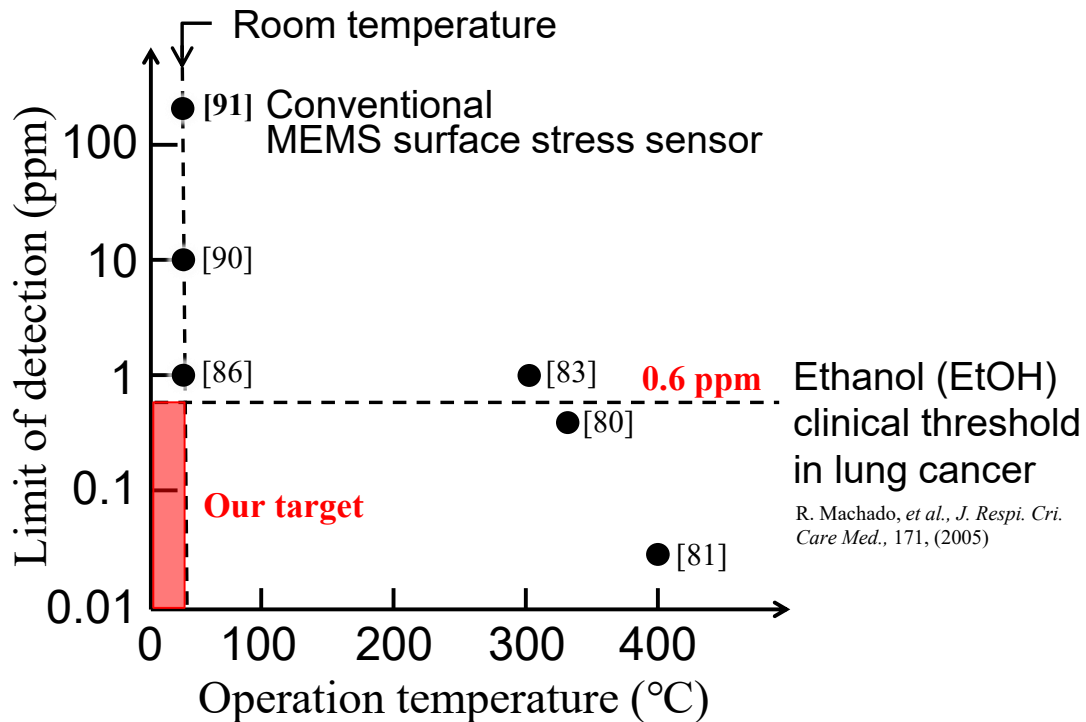
4.2 Aiming for the detection of volatile organic compounds in the breath

As a less invasive screening technique, volatile organic compounds (VOCs) in exhaled breath can be utilized as biomarkers to diagnose diabetes and renal failure,

lung cancer; this method has attracted interest over recent years as a promising diagnostic method for diseases with low patient burdens [75]–[78]. While the concentration of volatile ethanol gas in the exhaled breath is reported at 27–216.1 ppb in healthy people, it increases to 64–2160 ppb in patients with lung cancer and their average value is 0.6 ppm [78]. Therefore, it can be used for patient screening by achieving an operating range of ppm to sub-ppm. In recent years, various sensors have been developed to detect ethanol (EtOH), a type of VOC. Zhang *et al.* succeeded in detecting a wide dynamic range of 0.001–1000 ppm with high sensitivity in a gas sensor based on SnO₂ films as a method of reading out the resistance change caused by target molecules adsorbed on the gas-reactive film [79]. Because the oxide semiconductor-based gas-reactive film must be heated to several hundred degree Celsius for the sensing operation, the heater must be integrated around the sensing part [80]–[82]. The power consumption of the heater can be reduced by releasing the sensing area from the substrate through a hole, decreasing the heating capacity of the sensing area and preventing temperature increase in peripheral circuits [83], [84]. However, challenges such as the complexity of the fabrication process from integrating heaters into a sensor and an increase in footprint per unit element because of isolated heating parts from the peripheral circuits persists. Therefore, in recent years, gas sensors operated at room temperature without a heater have become popular. Semiconductor-based gas sensors have been reported to operate even at room temperature, but the LOD decreases to approximately several ppm [85], [86]. Another detection method which can operate at room temperature involves sensors using ZnO₂ nanohybrid thin films as gas-reactive films; these sensors can detect ethanol gas in a concentration range of 10–100 ppm by detecting the amount of change in the effective refractive index as a change in the peak shift of the reflection spectrum when white light is irradiated [87]. Alternatively, MEMS surface-stress sensors have been reported as gas sensors for room-temperature operation. An epoxy acrylate film with a gas-reactive film was used to successfully detect EtOH in a wide dynamic range of 200–16000 ppm [88]. Despite the challenges of detection sensitivity, surface-stress sensors have been widely studied as bio and gas sensors because they can be used to detect various target molecules by selecting the appropriate reactive membrane. Generally, although gas-reactive films have a challenge of the selectivity of gases, gas species can be identified by acquiring the response patterns of several types of

gas-reactive films and implementing machine learning [89]. Therefore, sensor arrays and the coating of several reactive films are practical solutions.

Fig. 4.1 summarizes the LOD and operating temperatures in EtOH detection. Assuming the application to a simple IoT chemical sensor, a sensor with a low detection limit is desirable in a detection method that can operate at room temperature, for which low power consumption is expected. However, a sensor that can operate at room temperature with a detection limit of less than 0.6 ppm, which is necessary for the screening of lung cancer patients, has not been realized. Therefore, we aimed to create such a sensor. Assuming that the above-mentioned sensors are used for both bio and chemical sensing applications, surface-stress sensors are the most versatile because they can be used in room-temperature environments and can respond to bio and gas molecules by changing the adsorption layer (adsorbed receptor molecules). Therefore, the deposition of a gas-reactive layer on the MEMS interferometric surface-stress sensor proposed by our laboratory is expected to enable the detection of volatile ethanol gas in a room-temperature environment.



- [80] M. Righettoni, *et al.*, *AIChE Proc.*, 82 (2010) [86] D. Zhang, *et al.*, *RSC Adv.*, 24 (2015)
 [81] A. Güntner, *et al.*, *Sens. act. B chem.*, 257 (2018) [90] O. Lupan, *et al.*, *Phys. Status Solidi. Lett.*, 10 (2016)
 [83] Q. Wan, *et al.*, *Appl. Phys. Lett.*, 84 (2004) [91] H. Guo, *et al.*, *IEEE Electron Device Lett.*, 33 (2012)

Figure 4.1: Comparison of operating temperature and LOD in each EtOH sensing sensor [80], [81], [83], [86], [90], [91].

4.3 Design of the MEMS interferometer

Fig. 4.2 shows the schematic diagram of the cross-sectional structure and detection principle of an optical interferometric surface-stress sensor. This sensor is composed of a parylene C deformable membrane and gas-reactive PMMA layer on a cavity formed in a Si substrate; hence, the Fabry–Perot interferometer comprises the deformable PMMA/parylene C membrane, air gap, and Si substrate. When a target gas molecule is absorbed in the gas-reactive layer, the deformable membrane is subjected to a compressive or tensile stress as the gas-reactive layer expands or contracts, respectively. The deformable membrane, including the gas-sensitive layer, is deformed upward in the former and downward in the latter. This mechanical deflection is observed as a peak shift in the reflection spectrum, which enables us to detect the small deflection of the membrane caused by the adsorption of target molecules.

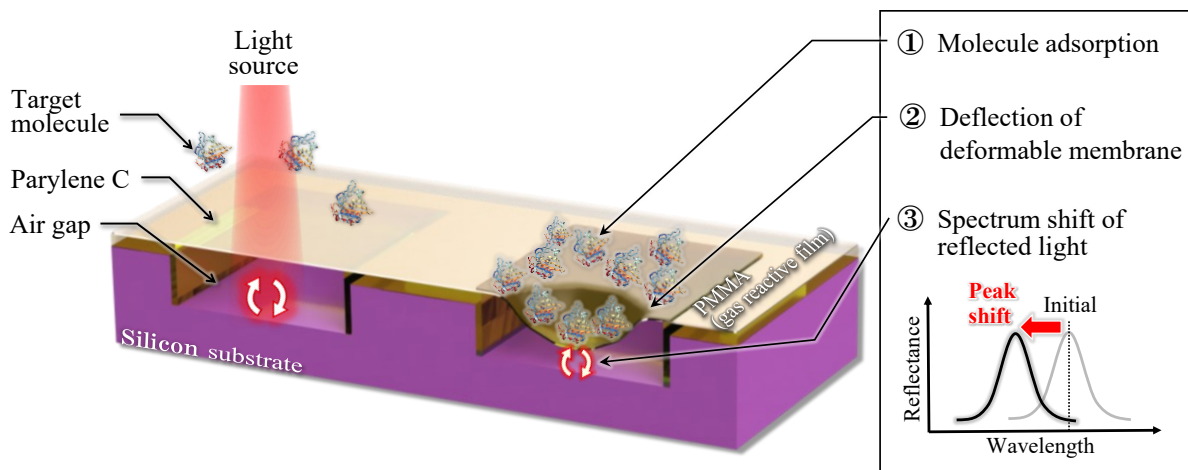


Figure 4.2. Schematic diagram and detection principle of MEMS optical interferometric surface-stress sensor.

Because the amount of deflection of the surface-stress sensor is inversely proportional to the Young's modulus of the material used for the moving part and thickness of the film [51], an increase in the detection sensitivity is expected when using a soft material with low Young's modulus and thin film thickness. Moreover, sensors based on optical interferometry can increase the shift in the interference spectrum at the time of membrane deflection by narrowing the air gap of the interferometer. As the detection performance can be improved without expanding the area of the device by controlling the above parameters, highly sensitive chemical sensing at room temperature can be achieved while compensating for the limitations of the piezoresistive sensor.

4.3.1 Analysis of the spectral shift associated with the deflection of the deformable membrane

Fig. 4.3 shows the optical analysis results of the ratio of the interference spectral shift associated with a 30-nm deformation of the deformable membrane using an optical analysis software (RSoft DiffractMOD). When the air-gap length of the interferometer is formed with the sub-micron scale, the peak shift involved with the membrane deflection increases. This means that the peak shift increases even when the deflection remains the same. Because the spectral shift ($\Delta\lambda$) is inversely proportional to the interference order, the response is expected to improve by the narrowing of the air gap through the reduction in the interference order to the visible region. In contrast, if the air gap is narrowed, the problem of stiction of the deformable membrane to the Si substrate occurs easily. Therefore, to prevent the stiction, we fabricated an interferometer with an air gap of $0.4\ \mu\text{m}$, which is sufficient for deflection during gas exposure. To validate the improvements, we also fabricated interferometers with air-gap lengths of 0.8 and $2.6\ \mu\text{m}$.

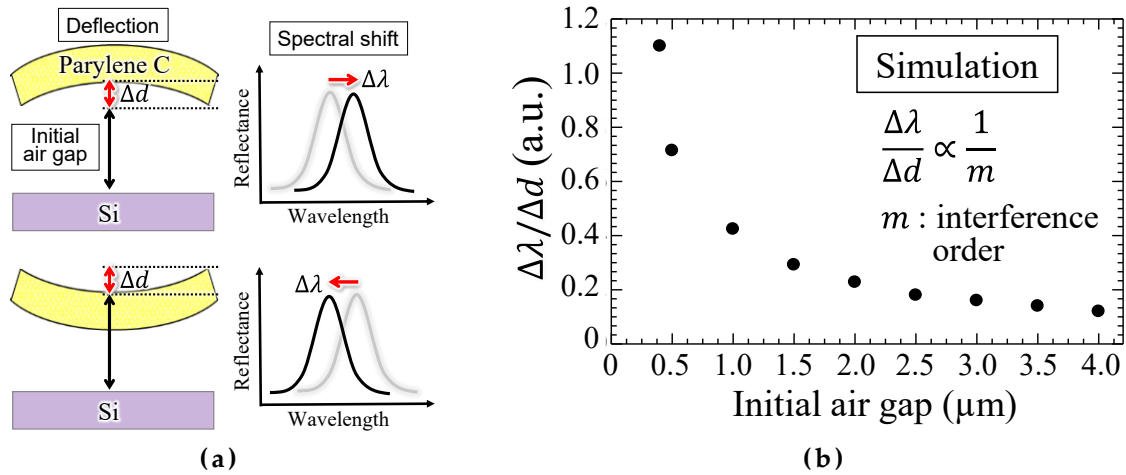


Figure 4.3: (a) Optical analysis model of the interferometer and (b) relationship between air-gap length of the interferometer and ratio of spectral shift to membrane deflection.

4.3.2 Analysis of the surface-stress sensitivity of the deformable membrane

Fig. 4.4 shows the analysis model and membrane deflection results with surface stress applied to the deformable membrane using the finite element method. When PMMA expands owing to gas adsorption, compressive stress is applied from the

edge to the centre of parylene C. During contraction, a tensile stress was applied in the opposite direction. The former is indicated as a red arrow and the latter as a blue arrow in Fig. 4.4a. The analysis results in Fig. 4.4b shows that the sensitivity of the deformable membrane to surface stress was larger when the deflection was smaller. The PMMA employed as a gas-reactive film has the following advantages: ease to form by spin coating and low Young's modulus, which is one order magnitude lower than that of metallic films such as Au, which is commonly used as a molecular adsorption layer in biosensing [44], [92]. In this design, the total film thickness, including PMMA and parylene C layers, was set to 300 nm, which was 100 nm lower than that of the conventional structure [93]. In addition, we changed the coverage ratio of the molecular adsorption layer on the top surface of the deformable membrane, extending the area to apply surface stress fourfold. Here, the wavelength resolution of the spectrometer (USB4000, Ocean optics) that evaluated the spectral shift was 0.3 nm, and the interference spectra were subjected to a 5-point moving average process after the acquisition of the spectra. Therefore, the lower limit of the measurable spectral shift was 1.5 nm. With the definition of the LOD as the value of the surface stress causing a 1.5-nm deformation, the LOD of the proposed structure was expected to be 7.4 times higher than that of the conventional structure.

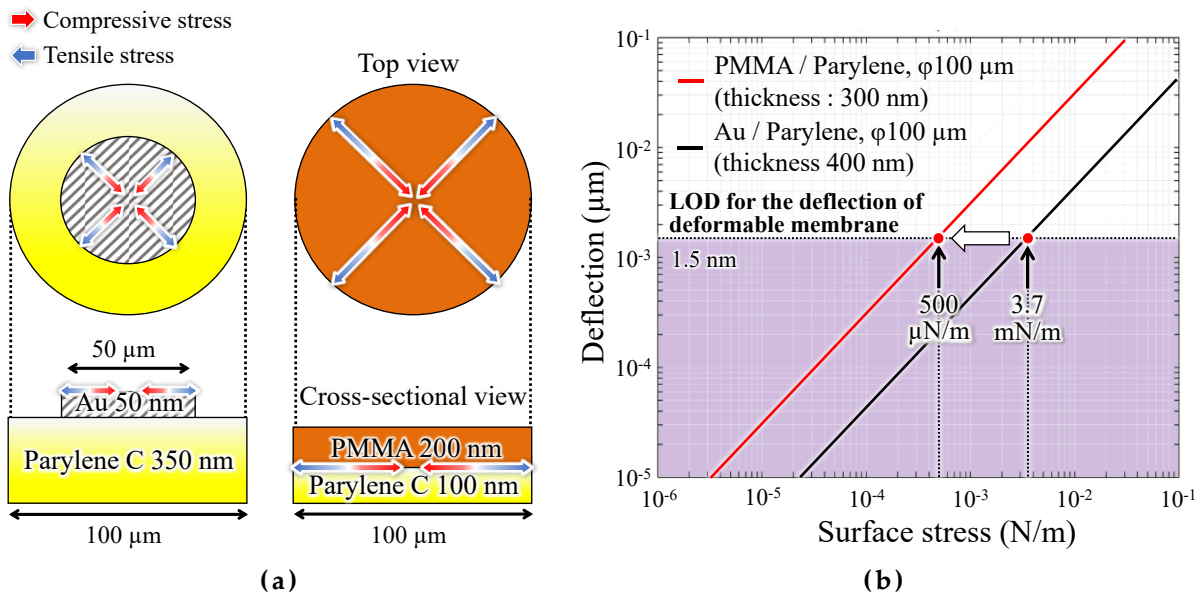


Figure 4.4. (a) Mechanical analysis model using the finite element method and (b) comparison of surface stress sensitivity between the conventional and proposed interferometer.

4.4 Fabrication procedure

Fig. 4.5 shows the fabrication procedure of a cavity-sealed interferometer. The fabrication process of this MEMS interferometer consists of two wafers: a transfer wafer to release the deformable membrane and a wafer to be transferred that forms a cavity. A strong bonding force is applied between the parylenes by simultaneously applying heat and pressure for a certain period with parylene C layers in contact with each other to seal the cavity of the interferometer [94]. The details of the fabrication procedure are as follows:

- (a) A parylene C thin film was deposited on a Si wafer coated with a surfactant (Micro-90, International Products Corp.)
- (b) Another parylene C layer was deposited on another Si wafer with a pre-formed cavity by reactive ion etching. Because the cavity depth formed in this process depended on the interferometer's air-gap length, interferometers with different gap lengths of 0.4, 0.8, and 2.6 μm were formed to compare differences in the response. The diameters of their sensing areas were determined to be 100 μm .
- (c) Pressure was applied in the two wafers by sandwiching them between steel plates and applying torque using four screws. The plate area and screw specifications were selected such that the applying pressure became 1.5 MPa, similar to that reported in [94]. In addition, heat and pressure were simultaneously applied by heating at 160 $^{\circ}\text{C}$ for 10 min in an N_2 gas atmosphere to bond the wafers.
- (d) The bonded wafer was immersed in DIW, which reacted with the surfactant to peel off the Si substrate, leaving the parylene C sheet on the Si wafer with cavities
- (e) Annealing was then performed at 160 $^{\circ}\text{C}$ for 1 h to improve the adhesion between the transferred parylene C sheet and parylene C layer on the Si substrate.

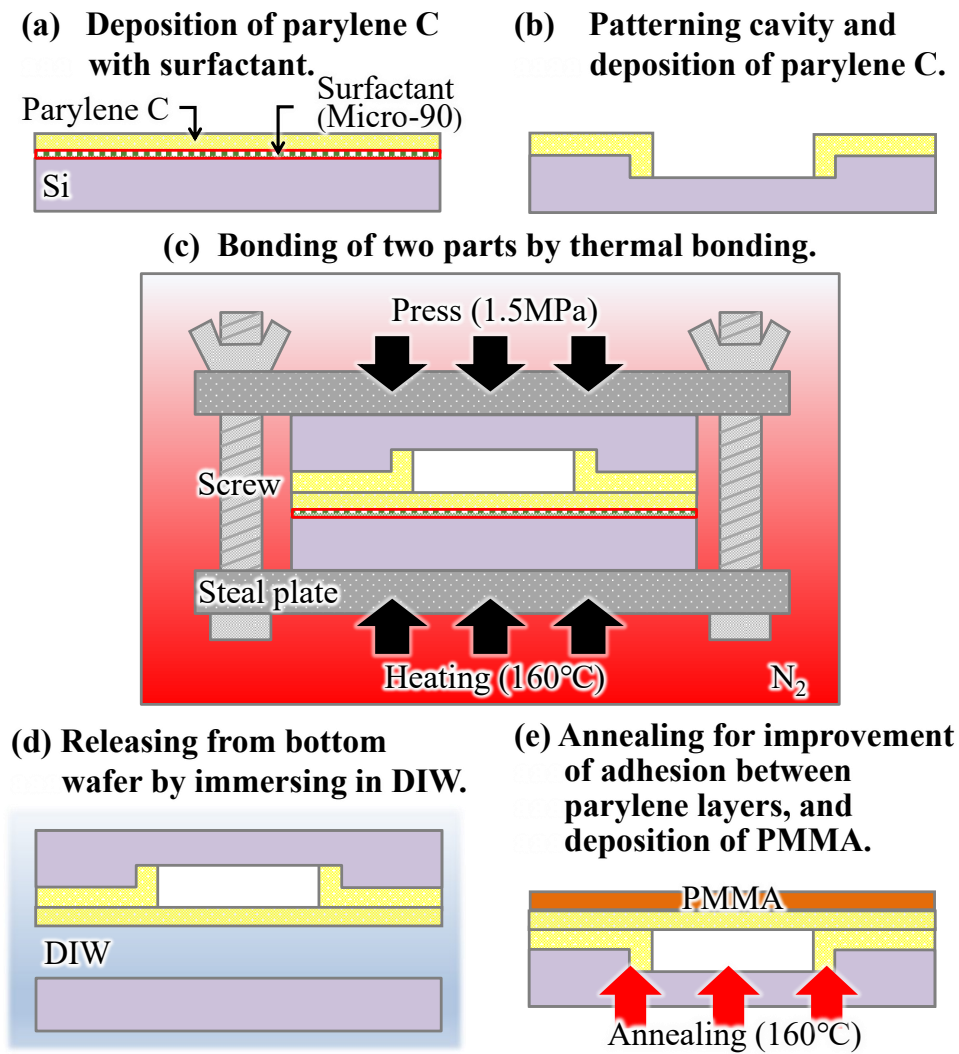


Figure 4.5. Fabrication process of the cavity-sealed interferometric interferometer.

4.5 Fabrication result

Fig. 4.6. shows optical microscope images of interferometers with different air-gap lengths and results of spectroscopic measurements when white light was irradiated onto the interferometer. The interference order (m) was obtained as follows:

$$m = \frac{2}{\lambda}(n_A d_A + n_P d_P) \quad (4.1)$$

where λ is the wavelength of interference peak, n_A and n_P are the refractive indexes of air and parylene C, respectively, d_A is the air-gap length, and d_P is the thickness of parylene C. The narrow air gap was observed to reduce the interference order. The obtained spectra EXHIBITED good agreement with the analytical waveforms with the air-gap lengths of 408, 778, and 2585 nm, respectively; thus, an interferometer close to the design values in sub-micro to micro scales was successfully fabricated.

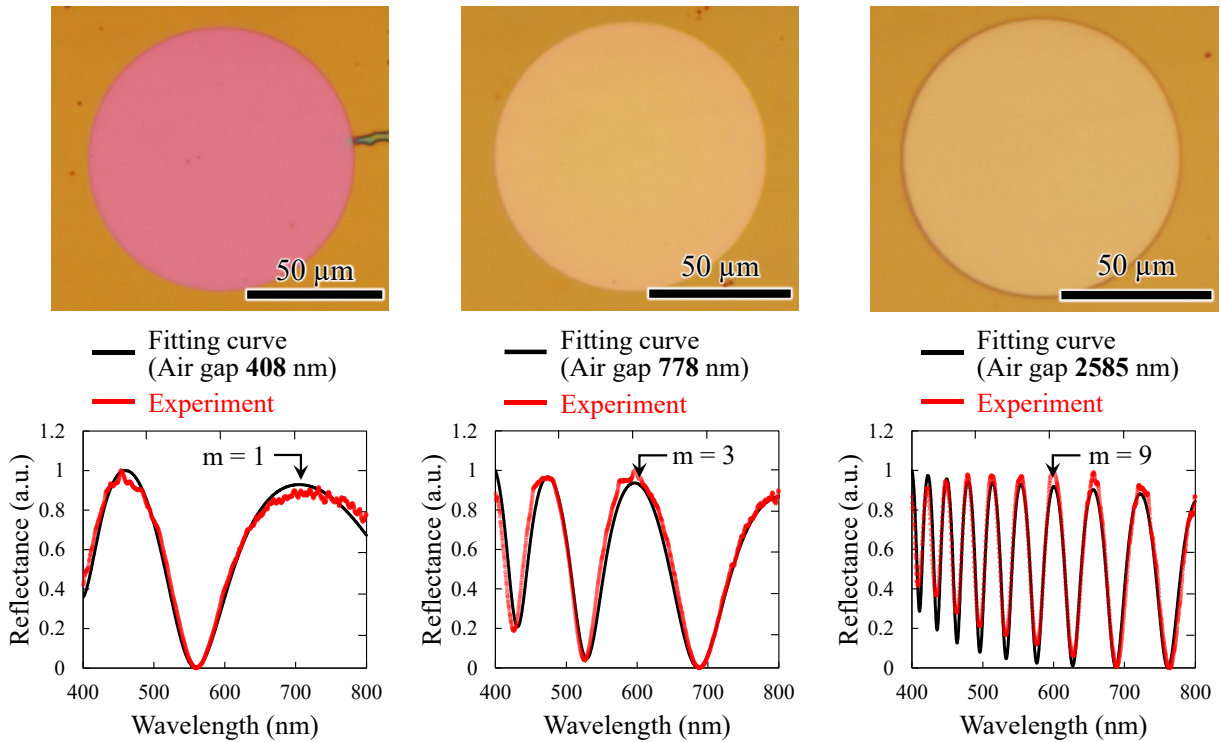


Figure 4.6. Optical microscope images (top) and reflection spectra (bottom) of developed Fabry-Perot interferometers. Fitting curves show good agreement with experimental values.

4.6 Conclusion

In this chapter, a new cavity-sealed MEMS interferometer with high surface-stress sensitivity, employing PMMA as a gas-reactive layer, is proposed for the detection of gas molecules in the air. We designed and fabricated the interferometer and obtained its reflection spectra, confirming that the interferometer was formed approximately equal to the design value. The key points of this chapter are as follows:

【Analysis results of optical design and finite element method】

1. The spectral response of the deflection of the deformable was confirmed to increase by narrowing the air-gap length of the interferometer and reducing the order of the interference in the visible wavelength region.
2. The surface-stress sensitivity increased by 7.4 folds compared with the interferometer with metal half-mirrors through the change of these parameters: adopting PMMA with an order of magnitude lower Young's modulus as a gas-reactive layer, extending the surface-stress area by four-fold, and reducing the thickness of the deformable membrane by 100 nm.

【Fabrication result】

3. We introduced a method using parylene bonding for a cavity-sealed MEMS interferometer and succeeded in fabricating an interferometer with an air-gap length of 408 nm. To compare the improvement in spectral response with narrower gaps, we fabricated three interferometers with different air-gap lengths, and their reflectance spectra were obtained; interferometers of 0.4, 0.8, and 2.6 μm were confirmed to be formed, which were approximately equal to the design value.

Chapter 5. Acquisition of sensor response for detecting gas molecules in the air

5.1 Preface

In the experiment described in this chapter, PMMA acting as a gas-sensitive film was spin-coated on the fabricated cavity interferometer and the response of PMMA to the absorption of volatile ethanol was acquired. First, we obtained the response of ethanol exposure to interferometers formed with different air-gap lengths and confirmed the improvement of the spectral response with narrower gaps. Next, using an interferometer that exhibited the highest spectral response, we evaluated the concentration dependence and LOD of volatile ethanol gas. Finally, we compared our fabricated sensor with other sensors that measure volatile ethanol in a room-temperature environment and demonstrated the superiority of the former.

5.2 Improvement of spectral response by narrowing the air-gap length of the interferometer

To evaluate the performance improvements resulting from narrowing the gap length, PMMA was spin-coated onto interferometers with gap lengths of 0.4, 0.8, and 2.6 μm . The deflection of the deformable membrane upon exposure to EtOH gas was measured as a shift in the reflection spectrum. Fig. 5.1 shows the detection system used in the experiment. Three interferometer chips with different gap lengths were arranged on a movable stage. The reflection spectrum, at 10 μm from the centre of the deformable membrane, was acquired at 20-s intervals with white light irradiation. In addition, a small petri dish with 0.4 mL of EtOH solution (diluted with 50% DIW) was placed near the chips and sealed with a large petri dish to prevent the leakage of the volatilized EtOH gas into the surrounding. The EtOH solution was placed in the vicinity of the chips for 9 to 20 min from the beginning of measurement and then removed. Fig. 5.2 shows the response of the volatile EtOH gas to the sensor. As shown in Fig. 5.2a, in the sub-micro scale narrow-gap interferometer, the membrane deflection was obtained as an interferometric colour change. Fig. 5.2b shows the time course of the reflection spectra in the interferometer with an air gap of 0.8 μm . After exposure to EtOH gas, the reflection spectrum blue-shifted from (1) to (2). In other words,

shortening the optical path length caused a downward membrane deformation, suggesting that the absorption of EtOH caused the PMMA film to shrink. Later, in the absence of exposure to the EtOH gas, the interference waveform red-shifted to (3), resulting in overlaps with the interference waveform before the gas exposure. Fig. 5.2c shows the time course of the peak shifts associated with gas exposure in all interferometers. When the exposure to EtOH gas was stopped, the peak shift returned to the initial state, which meant a reversible response due to the change in gas concentration was obtained in all interferometers. Fig. 5.2d shows the maximum peak shift during gas exposure in all the interferometers. The change in the peak shift of the 0.4- μm -gap interferometer with reduced interference order was 2.0 and 11.1 times higher than that of the 0.8 and 2.6 μm gap interferometers, respectively. The value of the 0.8- μm interferometer was approximately close to the optical analysis value of 2.1, while the value of the 2.6- μm interferometer was 1.8 times higher than the analysis value. This meant that the 0.4- and 0.8- μm sensors had the same deflection amount during the gas response, while the 2.6- μm -gap sensors had a lower deflection. This may be because of the thickness of the PMMA film used as the gas-reactive film, which was thicker than that of the 0.4- μm -gap interferometer. Because the surface-stress sensitivity is inversely proportional to the square of the film thickness, the surface-stress sensitivity decreased by 1.8 times with a 35% thicker PMMA film in an interferometer with an air-gap length of 2.6 μm . The PMMA layer deposited by spin coating may have deformed the parylene C membrane downward because of the immediate pressure from adding the liquid. Because the PMMA on the deformable membrane with a relatively deep cavity was locally formed thicker than other areas, it was assumed to have decreased the surface-stress sensitivity of the 2.6- μm interferometer, thereby decreasing the membrane deflection. The narrow-gap interferometer demonstrated gas detection by the change in interference colour with membrane deflection and improvements in the spectral response.

To evaluate characteristics of the sensor response depending on gas species, we measured reflection spectra during exposure to 90% dilution of EtOH, ammonia, methanol (MeOH), and water vapour (92% relative humidity). Fig. 5.3 shows the results of acquiring the peak shifts in the reflection spectrum of the sensor after exposure to 90% dilution of EtOH, ammonia, MeOH, and water vapour. The amount of peak shift on the vertical axis was positive for the direction in

which the spectrum shifted to the shorter wavelength side. The largest peak shift was obtained for EtOH among the exposed gases, while exposure to gases other than

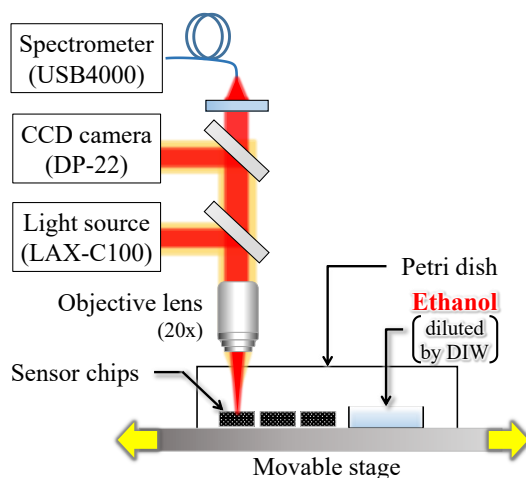


Figure 5.1: Schematic diagram of the experimental setup

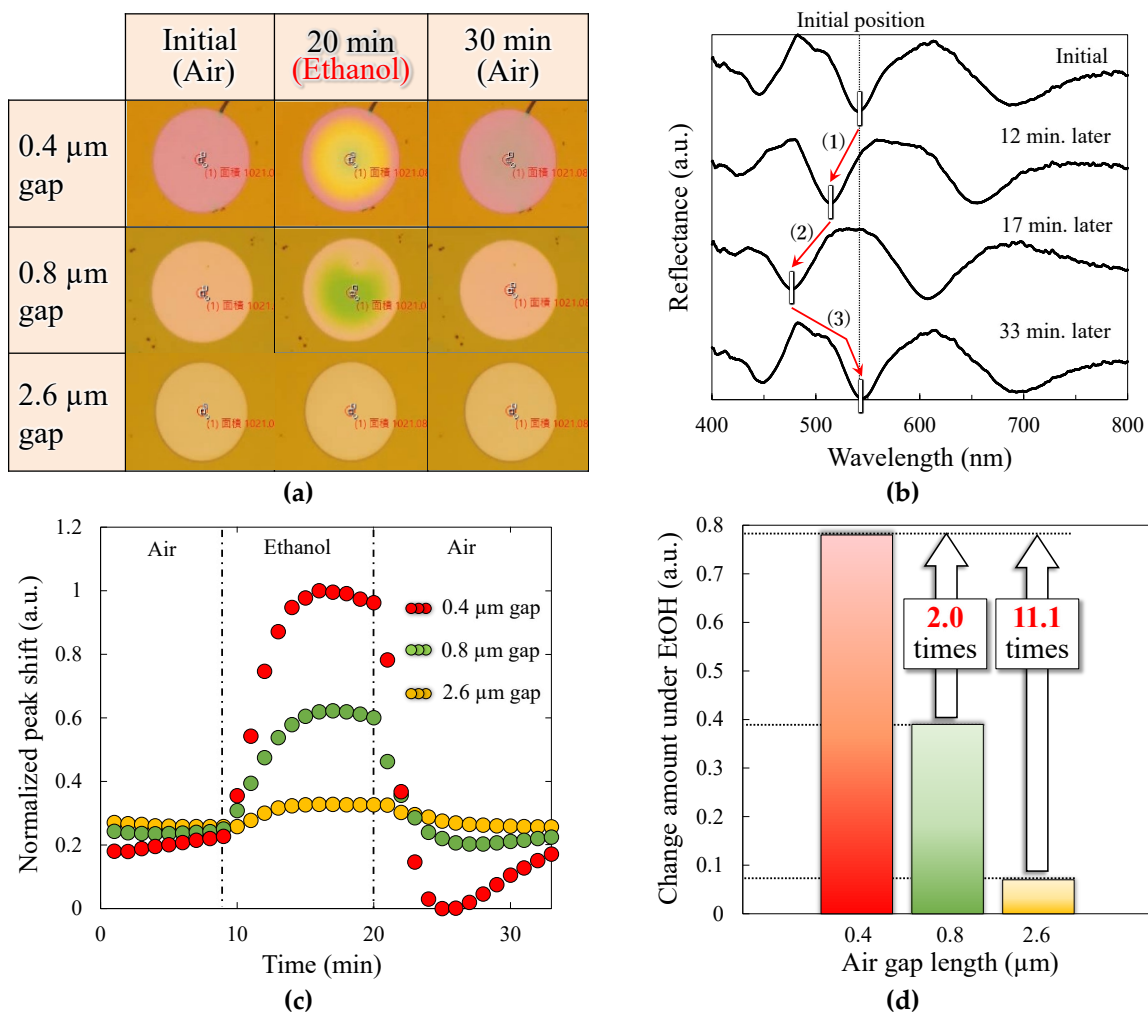


Figure 5.2: Comparison of interferometers with different air gaps under EtOH exposure. (a) Optical microscope images with colour change associated with

membrane deflection, (b) typical spectra shift in the interferometer of 0.8 μm gap, (c) change in peak shift to time, and (d) comparison of change amount in peak shift in the EtOH exposure.

EtOH resulted in a negative peak shift. In other words, since the deflection of the membrane occurred in the direction of cavity expansion, the PMMA layer of the gas-reactive membrane may have absorbed the gas and expanded, resulting in compressive stress to the deformable membrane. Thus, the expansion rate of PMMA differed depending on the gas species; we considered that there was a difference in the amount of peak shift. The result indicated that discriminating gas species with a single device is difficult, gas species can be distinguished through machine learning of the differences in the response patterns of multiple gas-sensitive membranes [82]. Note that we confirmed that the PMMA layer contracted and expanded during the absorption of EtOH and MeOH, respectively, which can be useful in discrimination gas species using machine learning.

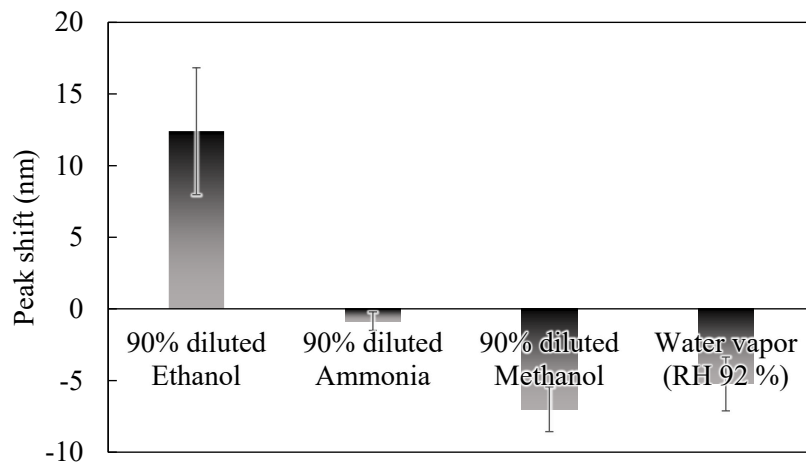


Figure 5.3: Comparison of gases response in interferometers with a 0.4 μm air gap and a 100 μm diameter. (Error bar means standard deviation of 3 interferometers on the same chip.)

5.3 Effect of changes in relative humidity and temperature

We measured the effects of temperature and humidity changes on the sensor. Under the condition of no ethanol in a petri dish, Fig. 5.4a shows the time course of the peak shift when the temperature was changed by a hot plate. In this experiment, the sensor chip was heated at 20 °C for the first 5 min, 27.5 °C for 5 to 22 min, and 35 °C for 22 to 45 min. Immediately after heating, the peak shift exhibited a negative value by the expansion of the film owing to thermal expansion, while the peak shift approached zero with time. Therefore, the deflection of the membrane because of temperature changes could be solved by ageing. Fig. 5.4b shows the time course of the peak shift of 90% diluted ethanol exposure at 20 °C and relative humidities of 55% and 92% (measured by a humidity sensor (HS1101LF, TE Connectivity)), respectively. The amount of change in the peak shift decreased under high humidity conditions while the nanomechanical response was obtained even in the high humidity environment. According to this result, when the relative humidity changed from 55% to 92%, the peak shift amount decreased by approximately 63%. The output response has been reported to decrease by 50% or more when the relative humidity changes from 50% to 90% in a semiconductor-based gas sensor using a heater [84]. Thus, the decrease in response in high-humidity environments is the same as that of other gas sensors.

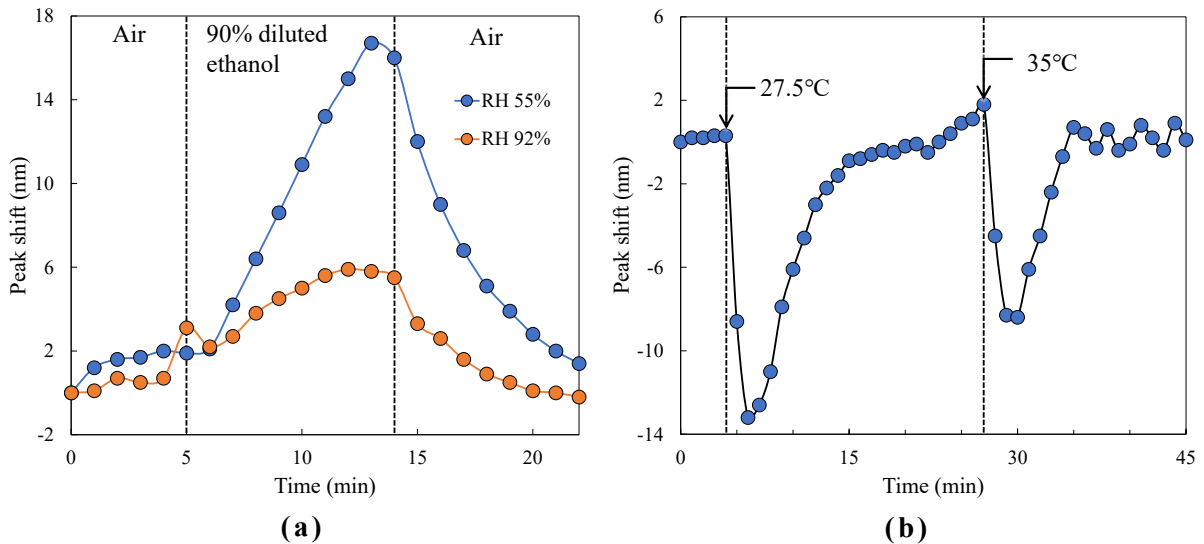


Figure 5.4: Impact of changes in temperature and humidity in interferometers with a 0.4 μm air gap and a 100 μm diameter. Time course of peak shift with (a) temperature change and (b) humidity change.

5.4 Concentration dependence and LOD

To evaluate the concentration dependence of the 0.4 μm interferometer, which showed the highest response to ethanol in the above-mentioned experiments, we performed experiments to obtain the peak shifts with changes in the dilution rate of ethanol from 60 to 100% (Fig. 5.5). The spectral response to changes in the ethanol dilution rate, on three interferometers with a 0.4- μm gap, was measured nine times and expressed as the standard deviation using error bars. At a noise level of 1.5 nm, determined by the spectrometer and moving average processing, the shift amount of 4.4 nm at a dilution rate of 97.5% was the minimum LOD. In addition, the MEMS interferometer had an approximately linear response when the dilution rate was between 60% and 97.5%. To obtain the correlation between the ethanol concentration and sensitivity, the concentration was identified with a commercial semiconductor gas sensor (TGS2620, Figaro). As Fig. 5.6a shows, the semiconductor gas sensor had a linear response in the range below 80% dilution rate, which is the guaranteed operating range represented by the ratio of resistance change of 0.18–3.4 [26]. In contrast, the stability was extremely degraded in the low-concentration range, where the dilution rate exceeded 80%, although the response changes according to the concentration. Fig. 5.6b shows the result of estimating the concentration of EtOH from the obtained resistivity for the dilution rate below 80%, indicating a linear response in the semiconductor sensor. Assuming the EtOH concentration of 0 ppm at 100% dilution, and extrapolating the linear response region of the semiconductor gas sensor, the concentration of EtOH at 97.5% dilution was obtained as 5 ppm, which was the lower LOD of the MEMS interferometer. Furthermore, in the low concentration range (dilution rate of 90–97.5%) exceeding the guaranteed operation range of the commercial gas sensor, a stable response could be obtained with a standard deviation of 0.62–1.24 compared with 1.72–3.03 for the semiconductor sensor.

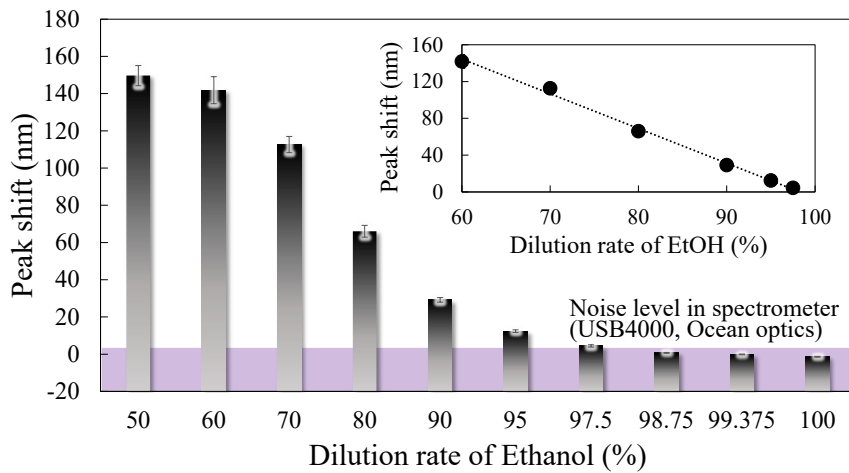


Figure 5.5: Concentration dependence under EtOH exposure in interferometers with a $0.4 \mu\text{m}$ air gap and a $100 \mu\text{m}$ diameter. (Error bar means standard deviation of 9 interferometers.)

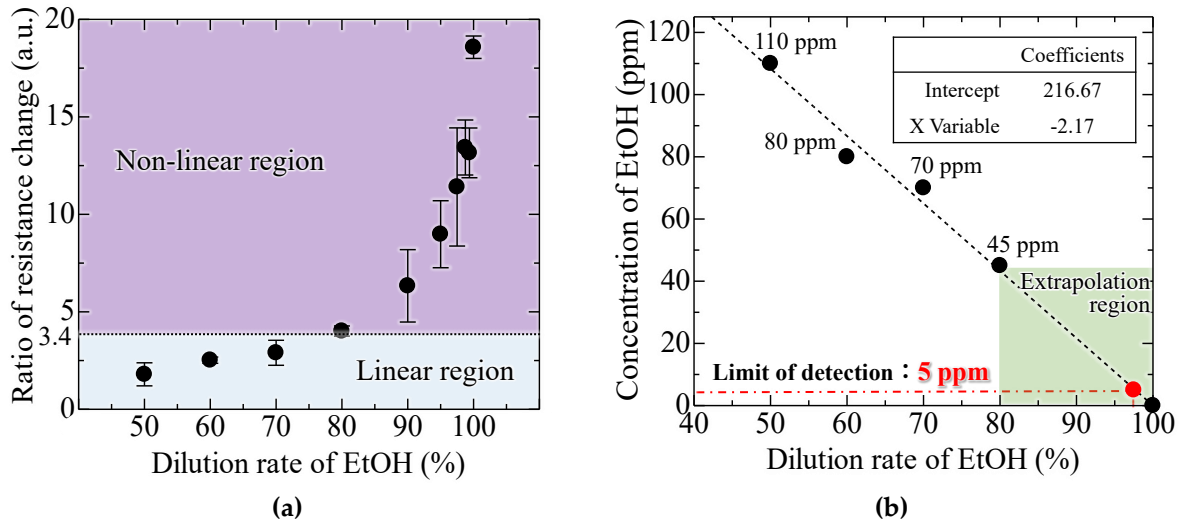


Figure 5.6: Estimation of the LOD of EtOH in MEMS Interferometer using semiconductor gas sensor. (a) Output response of semiconductor gas sensor and (b) correlation between dilution rate and concentration of EtOH. (Error bar means standard deviation of 3 semiconductor gas sensors.)

5.5 Improvement of LOD by optimizing geometry parameters

For further improvements in minimum LOD, the sensitivity of the MEMS surface-stress sensor was adjusted by changing the membrane diameter and thickness. Fig. 5.7a shows changes in the surface-stress sensitivity when the diameter of the deformable membrane expanded from 100 μm to 200 and 300 μm . The surface-stress sensitivity increased by ninefold when the diameter was extended by a factor of three.

The deformable membrane was further thinned without expanding the diameter. Subsequently, the surface-stress sensitivity of the interferometers with 50-nm-thick parylene C and 100-nm-thick PMMA, which are the minimum thickness formed by dry transfer and spin coating, respectively, were measured. Here, the surface-stress sensitivity increased by approximately fourfold (Fig. 5.7b), which was equivalent to 125 $\mu\text{N/m}$, which was the analysis value of sensitivity when the diameter was doubled. Therefore, the detection limit was expected to increase by more than one order of magnitude by simultaneously increasing the area of the deformable membrane and reducing the thickness. The sensing area size and LOD of the ethanol sensors operated under room temperature are summarized in Table 5.1. The fabricated interferometer area was more than two orders of magnitude smaller than that of the conventional piezoresistive surface-stress sensor, and it had superior detection limits. The sub-micron gap interferometric surface-stress sensor presented here exhibited ppm-level gas detection, which was almost equivalent to the performance of the latest semiconductor-based gas sensor at room temperature. By optimizing the geometry parameters, a sensor that can detect sub-ppm ethanol concentrations can be developed, which exceeds the detection performance of conventional room-temperature gas sensors.

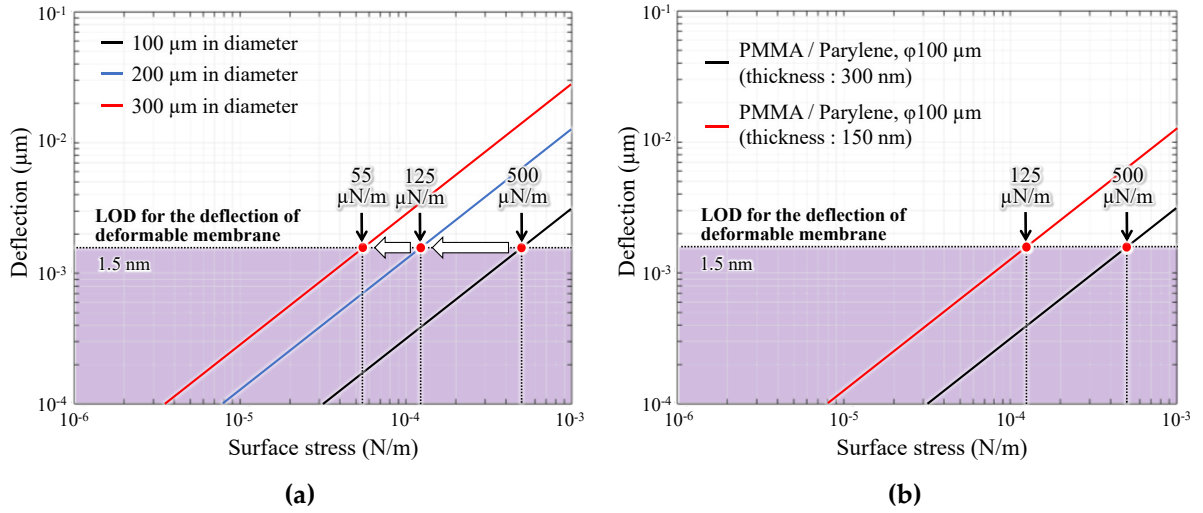


Figure 5.7: Improvement of detection limits by optimizing the surface stress sensitivity of interferometers. In the case of (a) expanding the diameter and (b) thinning of the deformable membrane.

Table 5.1 Comparison of EtOH sensing reports at room temperature.

Device type	Sensing area (μm^2)	LOD for EtOH (ppm)	LOD for surface stress ($\mu\text{N/m}$)	Ref.
SnO_2 -rGO hybrid film	N/A	1	N/A	[86]
Piezoresistive cantilever	1.2×10^6 Si bridge structure (1.1 mm \times 1.1 mm)	200	N/A	[88]
(a) This study (Experiment)	7.9×10^3 100 μm in diameter 300 nm in thickness (150x smaller than the piezoresistive type)	5	500	N/A
(b) This study (Analysis)	2.4×10^4 300 μm in diameter 300 nm in thickness (50x smaller than the piezoresistive type)	N/A	125	N/A
(c) This study (Analysis)	2.4×10^4 300 μm in diameter 150 nm in thickness (50x smaller than the piezoresistive type)	N/A	55	N/A

5.6 Conclusion

This chapter describes the deposition of PMMA, which acts as a gas-reactive layer, onto the cavity-sealed MEMS interferometer with high surface-stress sensitivity, and the concentration dependence and LOD of the sensor to volatile ethanol exposure is evaluated by obtaining the spectral response. We demonstrate that the spectral response can be improved by narrowing the air-gap length of the interferometer to 0.4 μm ; we successfully detected volatile ethanol at a concentration of 5 ppm in a room-temperature environment. The results indicated that the sensitivity of the sensor is comparable to that of a semiconductor-based sensor, which has the highest sensitivity for measuring ethanol at room temperature and suggested the feasibility of a sensor that can detect sub-ppm ethanol concentrations at room temperature by optimizing the shape parameters of the interferometer. The key points of this chapter are as follows:

【Experimental results】

1. The spectral response of 50% diluted volatile ethanol to interferometers with different air-gap lengths of 0.4, 0.8, and 2.6 μm was acquired and the reversible response because of the change in gas concentration was confirmed for all interferometers.
2. In the interferometer with an air-gap length of 0.4 μm , the change in the peak shift increased by 2.0 and 11.1 times compared with the 0.8- and 2.6- μm interferometers, respectively.
3. In an interferometer with an air-gap length of 0.4 μm , a linear response between 5–110 ppm of volatile ethanol concentration was obtained, and the LOD of the sensor was 5 ppm.
4. The optimization of the diameter and thickness of the deformable membrane in an interferometer suggested the feasibility of a sensor that can detect ethanol at a concentration of sub-ppm order, surpassing conventional gas sensors that can operate in room-temperature environments.

Chapter 6. Neurotransmitter detection using the MEMS interferometer with molecularly imprinted polymer

6.1 Preface

Thus far, we have demonstrated that the fabricated MEMS interferometers can detect both macromolecular proteins in liquids and gas molecules in air with greater sensitivity than conventional sensors. Therefore, if a bio-interface that can adsorb neurotransmitters can be constructed on the sensor, we can detect small molecules which have been difficult to detect using conventional surface-stress sensors.

As this chapter describes, an MIP was introduced on the cavity-sealed interferometer to detect neurotransmitters as an example of a small size molecule. First, a summary of the characteristics of typical MIP is introduced. Next, the fabrication procedure for forming the MIP onto the cavity-sealed interferometer is described. Third, the composition of this MIP and the formation of the neurotransmitter template are evaluated. Finally, using the MIP which confirmed the template formation, the detectability of neurotransmitters is described by comparing the sensor response because of the presence or absence of neurotransmitters.

6.2 Aiming for the detection of neurotransmitters

In the brain, neurotransmitters are released from the presynaptic cell to the postsynaptic cell, and they have a significant function in the control of the mind. For example, dopamine (DA) is known to cause excitement, such as joy and pleasure, noradrenaline to cause anger, anxiety, and fear in response to stress, and serotonin to regulate the secretion amount of DA and noradrenaline and to stabilize the mind. The imbalance of these concentrations is known to cause various diseases, and a decrease in the concentration of DA is highly correlated with the occurrence of Parkinson's disease [95], which causes impaired motor function. An excessive increase in DA levels have been reported to cause Huntington's disease [96], in which the limbs move against their will. Therefore, if these concentrations can be measured daily, and countermeasures can be

implemented, the number of patients with these diseases can be reduced. For the detection of these neurotransmitters, MEMS surface-stress sensors based on receptor-binding proteins and FET biosensors based on enzymatic reactions have been developed and their sensitivity has been improved. In the former, by focusing on the ability of receptor-binding proteins to change their own structure depending on neurotransmitter's concentration, and detecting surface stress change because of the structural change, acetylcholine (ACh), which is a known neurotransmitter, was detected at a concentration of 10 nM [97]. In the latter, by detecting the change in charge density in hydrogen ion caused by enzyme reaction, ACh at a concentration of 0.5–1000 μ M was detected [98]. However, the receptor-binding proteins used in the previous report have several problems: the reagents are expensive, detectable small molecules are limited, and they lack versatility; thus, there are few examples of detecting neurotransmitters using surface-stress sensors. The latter method using enzyme also has several problems: lack of stability, expensive, and require much time to produce, thus not being suitable for long-term storage [99]. Therefore, MIPs have become popular as alternatives to these molecular adsorption layers. This technique utilizes the specific binding of target molecules to the template by forming a template of the target molecule inside the MIP. The molecular imprinting method has several features: it can be developed for any template, it is stable in various conditions (pH, temperature, ionic strength, solvents), cost-effective synthesis, and long term storage without loss in performance (several months to years) [100]. However, when forming macromolecular templates, the problem of varying binding affinity is encountered because of its structural change. Therefore, when detecting macromolecules using MIPs, the formation of epitope templates, which is the smallest site where the antibody molecule recognizes the antigen molecule, has been proposed [101]. However, since producing the epitopes is expensive, the antibody-based method is a practical solution of detecting macromolecules in surface-stress sensors. As an example of MIP devices, by forming an MIP on the gate-electrode of an FET and by detecting the change charge density caused by the target adsorption to the templates, DA, which is known as a neurotransmitter, has been successfully detected at a concentration of 96 nM [99]. Therefore, if this MIP can be formed on the MEMS interferometer, low-molecular-weight neurotransmitters that have been difficult to detect using conventional surface-stress sensors can be detected.

6.3 Introduction of molecularly imprinted polymers

Table 1 shows typical monomers and formation techniques for MIPs and their features. Oxidative polymerization [102]–[104], in which MIPs are formed by supplying oxygen to the reaction solution, can be formed on any substrates, but forming them with uniform film thickness and density is difficult. Furthermore, the deformable membrane easily sticks to the Si substrate when the bubbles generated during oxygen supply touch the freestanding structure, resulting in device failure. In addition, MIPs using UV irradiation are formed by drop-casting a mixture of target molecules and cross-linkers in a low-molecular-weight solvent, followed by the cross-linking of the solvent using UV irradiation [105], [106]. In this technique, the MIPs can be formed only in the irradiated area by immersion in a stripping solution after exposure with a shadow mask during UV irradiation. However, because of the use of the acidic solution in the process of removing the imprinted molecules, available materials in the sensor are limited. In contrast, electrochemical polymerization [107]–[110], in which MIPs are formed by repeated potential sweeping in the reaction solution, is characterized by the easy control of film thickness and the formation of high-density polymerized films; it can be used only on conductive materials. In addition, when DA is used as the imprinting molecule, the DA is removed by immersion in ethanol, and templates can be easily formed [111]. When forming MIPs on the MEMS interferometer, a high-density MIP should be formed to uniformly apply surface stress to the deformable membrane. Furthermore, selecting highly reflective materials for the mirror surface of the interferometer improves the wavelength selectivity and the output response when a small deflection of the deformable membrane occurs [93]. Therefore, we selected polypyrrole (PPy) formed using electrochemical polymerization as the MIP layer to satisfy these conditions.

Table 6.1. Comparison of MIP-based common monomers and polymerization procedure, and their properties.

Monomer	Polymerization Procedure	Advantage	Disadvantage
Dopamine	Oxidation	Can be formed on any substrate	Unable to form uniform film thickness and density
Boronic acid	UV	Easy patterning	UV impairs the flexibility of the movable membrane
Pyrrole	Electrochemical	Can be formed high-density polymerized film with easy control of film thickness	Can be formed only on conductive materials

6.4 Fabrication procedure

Fig. 6.1 shows the fabrication procedure of the MEMS interferometer with an MIP film. This MEMS interferometer formed a cavity-sealed structure through the dry transfer of nanosheets fabricated from conductive materials (e.g. Au) and parylene deformable membrane to the cavity-formed chip. The details of the fabrication procedure are as follows:

- (a) Cavities were formed using deep RIE on the Si substrate. Since the cavity depth formed in this process corresponded to the air-gap length of the interferometer, the cavity depth was selected such that the deformable membrane did not adhere to the bottom surface through liquid pressure.
- (b) After the adhesion on Si was improved through silane coupling treatment, parylene C was deposited using vapour deposition. This parylene functioned as a binder when parylene functioning as the deformable membrane was transferred to the chip with cavities.
- (c) Parylene C was deposited on the Si substrate after spin coating with a surfactant (Micro-90, Products Corp.), and then Au was deposited using a shadow mask to form the electrode shape.
- (d) After the carrier tape was attached to the wafer, the Au/parylene C film was released from the Si substrate by immersing it in DIW and reacting it with a surfactant.
- (e) The released deformable membrane was transferred to the chip with cavities on polytetrafluoroethylene (PTFE), followed by the application of heat at 160 °C for 1 h.

- (f) The interferometer was immersed in a mixed solution consisting of KCl buffer: Pyrrole: DA = 100:10:20 mM. By performing a potential sweep for three cycles in a range of -1–1 V and a speed of 0.04 V/s via a potentiostat, PPy of MIP films on Au were selectively formed.
- (g) The dopamine imprinted inside the polypyrrole layer was removed by immersion in ethanol and templates are formed in the film.
- (h) The carrier tape and PTFE were removed from the chip.

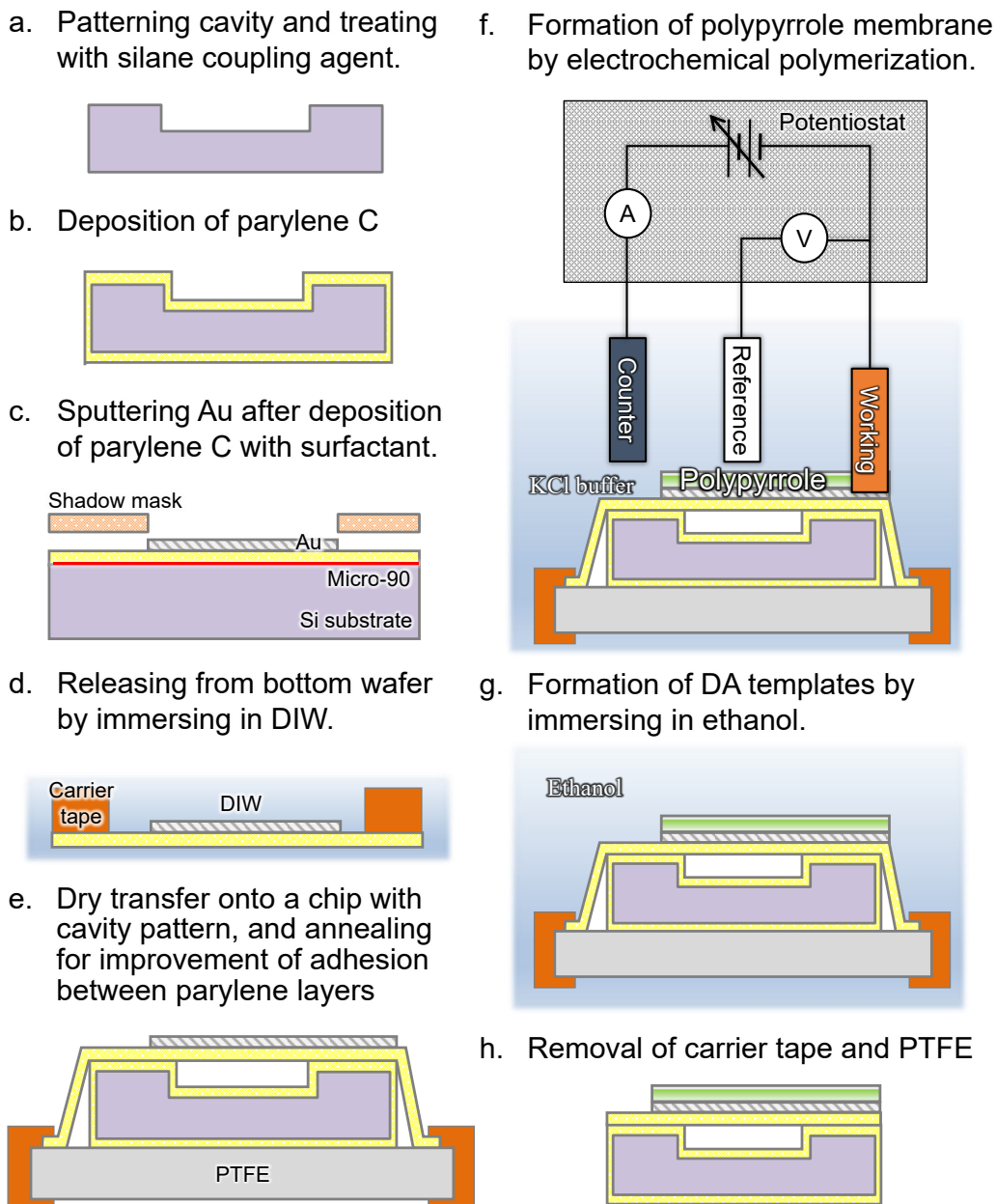


Figure 6.1: Fabrication procedure of MEMS interferometer with molecularly imprinted polymer film

6.5 Fabrication results

Fig. 6.2 shows an optical microscope image of the fabricated interferometer with an MIP film and the reflection spectrum obtained when white light was irradiated to the interferometer. The area functioned as the deformable membrane of the interferometer was formed to be 50 μm in diameter (Fig. 6.2a). Fig. 6.2c shows the reflection spectrum when the light was irradiated at the centre part of the interferometer using an optical fibre with a diameter of 200 μm and a 20 \times objective lens. The obtained reflection spectra are plotted on the graphs with the optical analysis results based on the optical analysis model of the interferometer shown in Fig. 6.2b. All the peaks of the analytical waveforms were in good agreement with the measured values, indicating that the interferometer structure which was close to the analytical model was formed; the domain structure observed on the film was considered to be caused by the non-uniform stress applied to the deformable membrane because of the local deposition of aggregates of Pyrrole, a monomer of PPy, on Au. This phenomenon could be solved by setting a slower sweep rate during electrochemical polymerization.

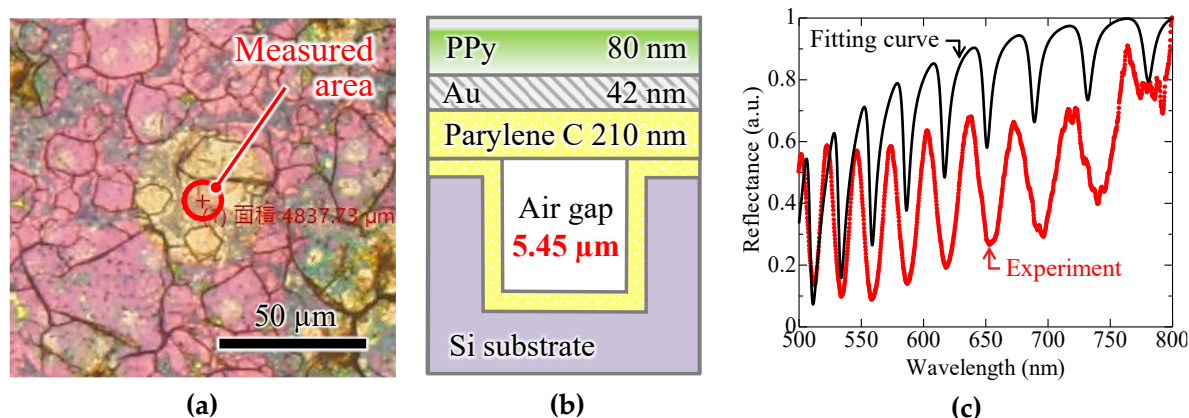


Figure 6.2: (a) Optical microscope image and (b) optical analysis model, and (c) reflection spectra of developed Fabry-Perot interferometer and analysis curve.

The composition of the PPy film formed by electrochemical polymerization was evaluated using Raman spectroscopy in the state of presence or absence of DA. Fig. 6.3 shows the measured Raman spectra. In the previous research [111], peaks owing to the C=C bond in PPy were reported to appear at 1335, 1414, and 1590 cm^{-1} , and weak peaks at 1265–1269 cm^{-1} and 1479–1495 cm^{-1} owing to the C-O bond in DA. In the Raman spectra obtained immediately after PPy formation, PPy-derived peaks (1334, 1416, 1590 cm^{-1}) and DA-derived peaks (1267, 1486 cm^{-1}) appeared, while after removal of DA, only three PPy-derived peaks (1335, 1414,

1590 cm^{-1}) appeared. These results suggested that DA was removed and the templates were formed in the MIP film.

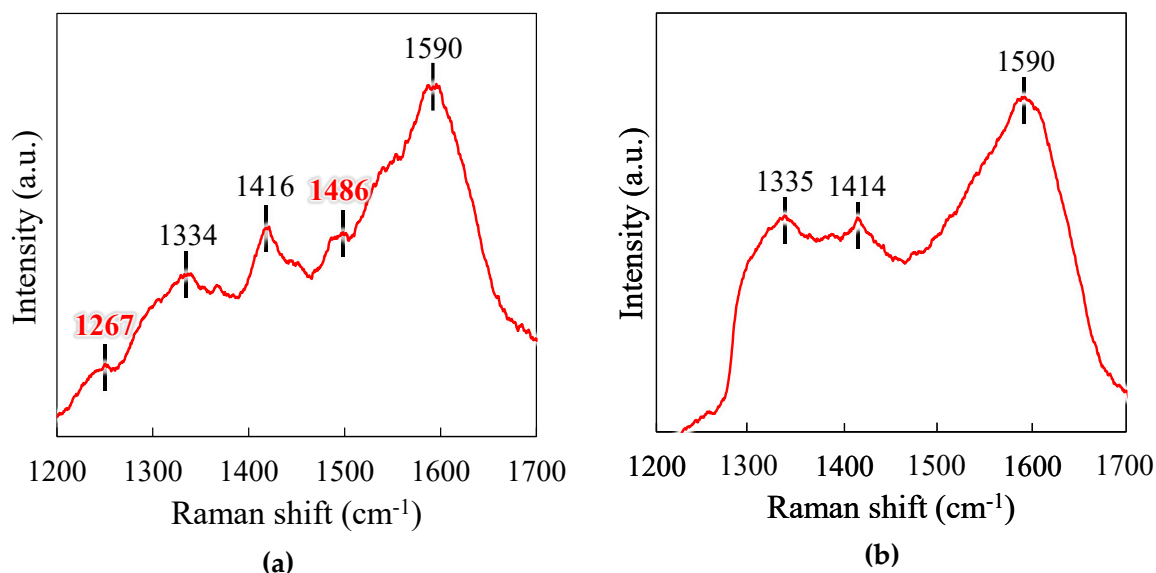


Figure 6.3: Raman spectra in molecular imprinted polymer (a) after deposition of PPy and (b) after removal of DA.

6.6 Acquisition of sensor response to neurotransmitter

Fig. 6.4 shows a schematic diagram of the experimental setup to measure the response of the adsorption of neurotransmitters. In this experiment, the sensor chip with DA templates was immersed in PBS for 60 min, and then a PBS solution containing DA was added to bring the final concentration to 1 μM . In this condition, Fig. 6.5 shows the time course of the reflection spectra when the light was irradiated to the interferometer immersed in PBS solution. Immediately after the DA addition, no variation was observed in the reflection spectrum, but it red-shifted with time. Figs. 6.6a and 6.6b show the time vs. peak shift amount of the reflection spectrum in the conditions between the absence and presence of DA. For the scenario of immersion in PBS without DA, the amount of shift was approximately 2 nm, whereas with DA, the amount of shift increased gradually after 20 min of immersion, and the amount of shift increased by approximately 5 nm at 100 min. In addition, the peak shift per unit time increased 1.4-fold to 0.0372 nm/min after DA was added, compared with 0.0269 nm/min for immersion in PBS without DA. This suggested that DA was gradually captured by the template in the PPy film by the DA addition, and during the expansion process of the PPy film, compressive stress was applied to the deformable membrane

underneath the PPy film, causing the membrane deflection. These results suggested that we obtained the spectral response due to the adsorption of DA.

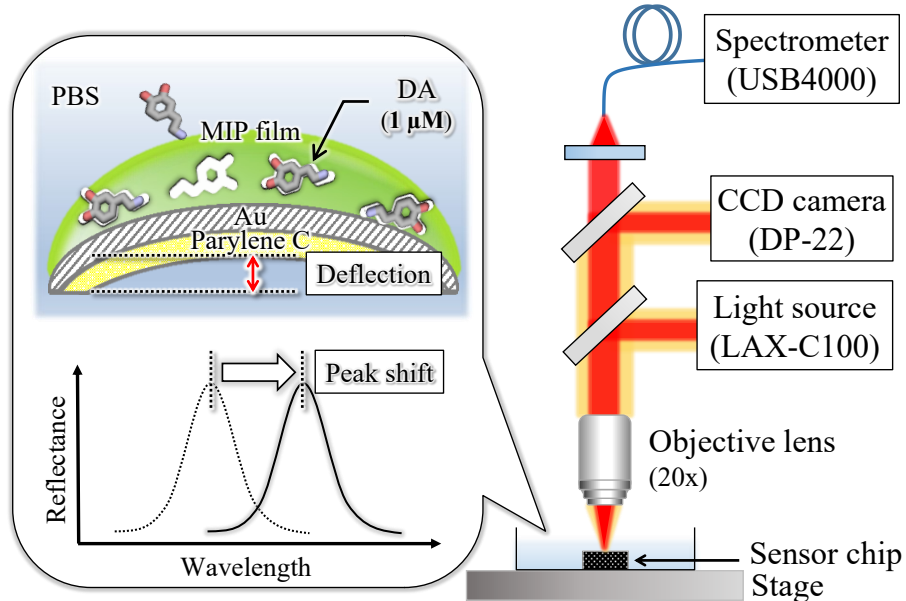


Figure 6.4: Schematic diagram of experimental setup for detecting deflection of deformable membrane caused by DA adsorption to the template.

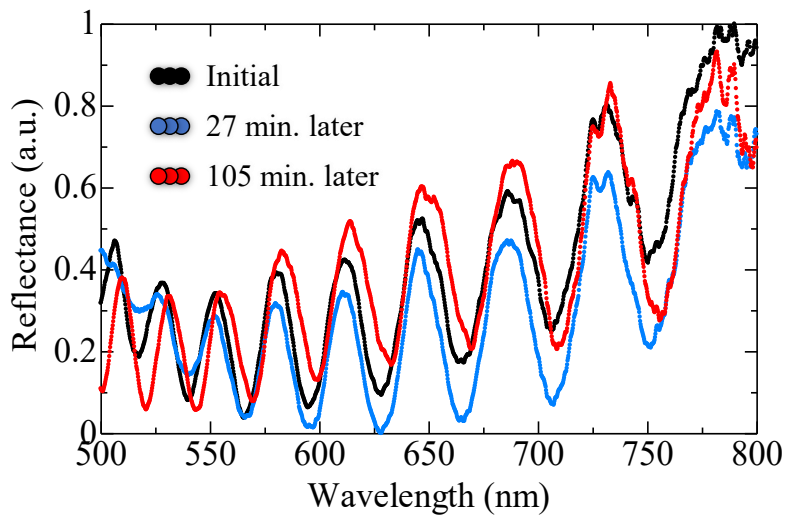


Figure 6.5: Reflection spectral shift after dropping DA in an interferometer with a 5.45 μm air gap and a 50 μm diameter.

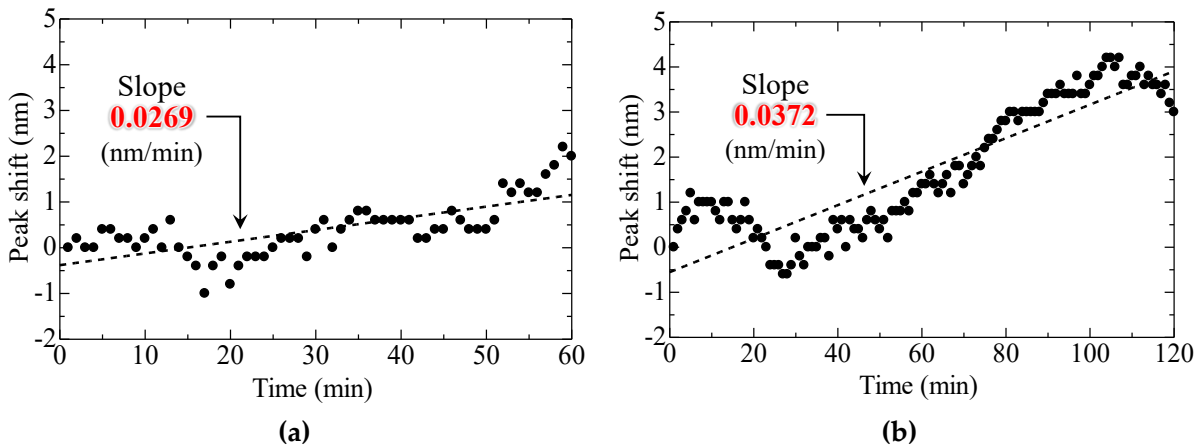


Figure 6.6: Time course of the amount of peak shift in the reflection spectrum in an interferometer with a 5.45 μm air gap and a 50 μm diameter. (a) Response to immersion in PBS and (b) response to a DA drop at a final concentration of 1 μM .

However, since the shift amount in the reflection spectrum due to DA adsorption was small (approximately 5 nm), a new interferometer with an air-gap length of 2.82 μm and a diameter of 300 μm was fabricated to improve the response, and the MIP films were formed using electrochemical polymerization under the conditions described in Section 6.4. Figs. 6.7 and 6.8 show the reflection spectra and time course of the spectra when the DA-containing PBS solution was added to the sensor chip to bring the final concentration to 1 μM after the sensor chip was immersed in PBS solution for 180 min. According to the result, the peak position of the reflection spectrum did not fluctuate at all during the immersion in PBS. For the peak shift amount, the peak shift of the spectrum in absence of DA was observed to be negative by approximately 7 nm within 15 min, and then it approached zero. This response was considered to be caused by a change in the pressure of the liquid during immersion, which caused the deformable membrane to temporarily sink and then return to the initial state. In contrast, for the presence of DA, the spectrum red-shifted with time. For the amount of the peak shift, we observed a negative shift of approximately 3 nm immediately after the addition, and a positive shift occurred after 16 min. This response was considered to be due to the deformable membrane temporarily sunk by liquid pressure, and then the expansion of the PPy film because of the adsorption of DA and the increase in the Coulomb repulsive force occurred. Before and after changing the geometry parameters of the interferometer, the peak shifts that occurred within 180 min after adding 1 μM DA were approximately 4 nm before and approximately 25 nm

after the change, and we confirmed that the response amount improved by approximately 6.3 times. These results suggested the possibility of label-free detection of neurotransmitters using MEMS interferometer with MIP films.

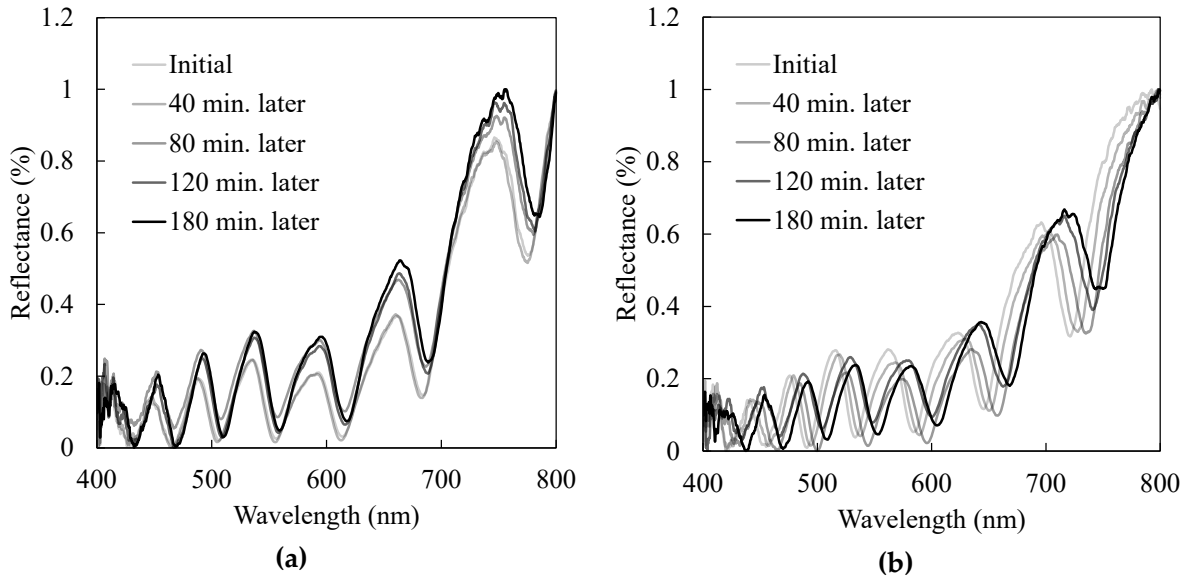


Figure 6.7: Reflection spectral shift in an interferometer with a 2.82 μm air gap and a 300 μm diameter. (a) Response to immersion in PBS and (b) response to a DA drop at a final concentration of 1 μM .

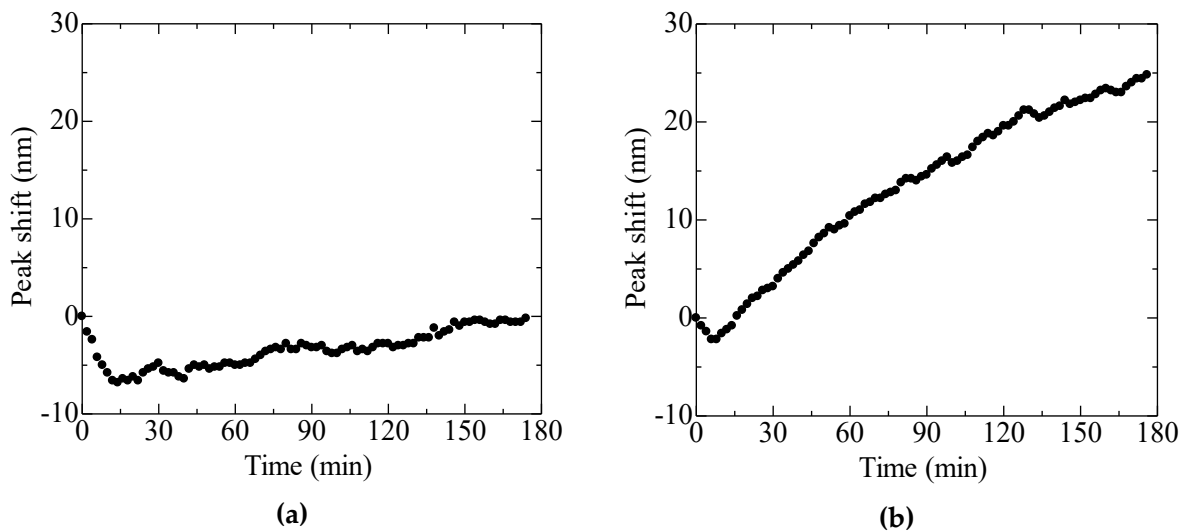


Figure 6.8: Time course of the amount of peak shift in the reflection spectrum in an interferometer with a 2.82 μm air gap and a 300 μm diameter. (a) Response to immersion in PBS and (b) response to a DA drop at a final concentration of 1 μM .

6.7 Conclusion

In this chapter, to detect small neurotransmitters in the cavity-sealed interferometer, a molecularly imprinted polymer (MIP), which can adsorb neurotransmitters, is introduced. A fabrication procedure for the formation of MIP on the interferometer was proposed, and a PPy film with a template of the neurotransmitter DA was formed on the fabricated interferometer using electrochemical polymerization. In addition, Raman spectroscopy was performed to confirm the formation of DA templates in the PPy film. In this sample, differences in the spectral responses were obtained in the presence and absence of DA, suggesting the possibility of detecting small neurotransmitters. The key points of this chapter are as follows:

【Fabrication and experimental results】

1. An 80 nm-thick MIP film (PPy) containing the DA was formed using electrochemical polymerization onto the interferometer with the cavity-sealed structure.
2. Using Raman spectroscopy, DA and PPy-derived peaks were observed immediately after imprinting DA, and only PPy-derived peaks were observed after immersion in ethanol, suggesting that the imprinted DA was removed from PPy and the DA templates were formed.
3. After immersing the sensor chip with DA templates in PBS, the time course of the reflection spectra was obtained when the DA-containing PBS was added to make the final concentration 1 μM . As a result, the peak shift per unit time increased 1.4 times to 0.0372 nm/min after DA was added, compared with 0.0269 nm/min when the sample was immersed in PBS without DA.
4. We confirmed that the sensor response of DA at a concentration of 1 μM increased by 6.3-fold by changing the geometry parameters of the interferometer.

Chapter 7. Overall conclusion

7.1 Summary

In this paper, we have described the development of sensors that can comprehensively detect molecules of various sizes without extending the Debye length. The MEMS optical interferometric surface-stress sensor proposed by our laboratory can comprehensively detect low-concentration and small molecules, which have been difficult to detect using conventional surface-stress sensors, as well as large molecules exceeding the Debye length by optimizing the wavelength selectivity and geometry parameters of the interferometer. Therefore, for the highly sensitive detection of target molecules of various sizes, interferometers with metal half-mirrors structure and cavity-sealed structure with optimized geometry parameters, which can improve the detection performance of the sensor, were fabricated and bio-interfaces for adsorbing molecules on the sensor were constructed. By conducting the above tasks, we aimed to develop the sensor for a label-free and comprehensive detection of proteins and neurotransmitters in liquids and gas molecules in air.

In Chapter 2, the selection of the mirror material and optical design, and analysis of surface-stress sensitivity of the interferometer for the realization of a metal half-mirrors structure are presented, and optimized sensor structure and film thickness conditions are described. According to these design and analysis, we observed that only the wavelength selectivity can be increased without decreasing the surface-stress sensitivity by designing the appropriate coverage of the upper half-mirror, and the wavelength selectivity in the near-infrared region can increase by 10.7-fold by forming 50 nm-thick Au half-mirrors on the top and bottom of the deformable membrane. In addition, when the air gap is increased by up to 10 nm, the transmission intensity changes of 52.93% can be obtained for the Au-mirrored structure, which is estimated to improve the output response to small deflection of the deformable membrane. Finally, the MEMS interferometer with Au a half-mirror structure that reflects the above findings was fabricated, and we successfully improved the wavelength selectivity of the interferometer, which was confirmed to be 6.6 times higher than that of a conventional interferometer with no mirrors.

In Chapter 3, to obtain the sensor response because of the adsorption of target molecules, a method of antibody modification using an SAM on the upper Au

mirror is established. By immersing the sensor with BSA antibodies at the terminal group of SAM in a BSA antigen solution at a concentration of 5 $\mu\text{g/mL}$, the deformable membrane was deformed by the antigen–antibody reaction to 64 nm in 30 min, resulting in a 13.6% change in transmitted light intensity that would be expected to be sufficient output current change if the photodiode is integrated. Furthermore, when the BSA antigen and streptavidin solution was added to the sensor, which had the same bio-interface, to bring the final concentration to 10 or 100 ng/mL , respectively, the deflection of membrane only occurred in the former scenario, suggesting that the fabricated MEMS interferometer can be used for the selective detection of target antigen molecules. Based on the results of this study, in recent research by our research group, the selectivity of the sensor was demonstrated by the amount of spectral shift caused by HSA antigen at a concentration of 1 ng/mL being more than three times greater than the response to the negative control PBS, IgG and streptavidin (final concentration of 1 ng/mL). Additionally, the large response to the shift amount of PBS without HSA antigen was obtained at the final concentration of 100 ag/mL –1 fg/mL , suggesting that the LOD of the protein in this sensor is 100 ag/mL –1 fg/mL . This result indicated that proteins can be detected at concentrations 200,000 times lower than can be detected using conventional MEMS surface-stress sensors, and the most sensitive detection was indicated to be possible in semiconductor-based label-free biosensors.

In Chapter 4, a new cavity-sealed MEMS interferometer with high surface-stress sensitivity employing PMMA as a gas-reactive layer is proposed for the detection of gas molecules in the air. In the optical design of the proposed interferometer, we confirmed that the spectral response of the deflection of the deformable can be increased by narrowing the air-gap length of the interferometer and reducing the order of the interference in the visible wavelength region. In addition, we confirmed that surface-stress sensitivity increased by 7.4-fold compared with the interferometer with metal half-mirrors by changing these parameters: adopting PMMA with an order of magnitude lower Young's modulus as a gas-reactive layer, extending the surface-stress area by four-fold, and reducing the thickness of the deformable membrane by 100 nm. We introduced a method using parylene bonding to realize a cavity-sealed MEMS interferometer that reflects the above findings, succeeded in fabricating an interferometer with 408 nm in an air-gap length. Furthermore, to compare the improvement in spectral

response with narrower gaps, three interferometers with different air-gap lengths were fabricated and their reflectance spectra were obtained, and interferometers of 0.4, 0.8, and 2.6 μm were confirmed to be formed, which were approximately equal to the design value.

In the experiment described in Chapter 5, PMMA, which acts as a gas-reactive layer, was deposited on the cavity-sealed MEMS interferometer with high surface-stress sensitivity, and the concentration dependence and LOD of the sensor to volatile ethanol exposure were evaluated by obtaining the spectral response. We demonstrated that the spectral response can be improved by narrowing the air-gap length of the interferometer to 0.4 μm , and we successfully detected volatile ethanol at a concentration of 5 ppm in a room-temperature environment. The results indicated that the sensitivity of the sensor is comparable to that of a semiconductor-based sensor, which has the highest sensitivity for measuring ethanol at room temperature; this suggested the feasibility of a sensor that can detect sub-ppm ethanol concentrations at room temperature by optimizing the shape parameters of the interferometer.

In Chapter 6, to detect small neurotransmitters in the cavity-sealed interferometer, we introduce the MIP, which can adsorb neurotransmitters, onto the sensor; the fabrication procedure for the formation of MIP on the interferometer is proposed, and PPy films with a template of the neurotransmitter DA were formed on the fabricated interferometer through electrochemical polymerization. In addition, Raman spectroscopy was performed to confirm the formation of DA templates in the PPy film. In this sample, differences in the spectral responses were obtained in the presence and absence of DA, suggesting the possibility of detecting small neurotransmitters.

Through these achievements, in the MEMS interferometer, we demonstrated the label-free detection of macromolecular protein and neurotransmitter in liquid and gas molecule in air; this indicated the feasibility of the sensor that can comprehensively detect molecules of various sizes. We expect that the realization of the device with no restriction on the size of detectable molecules and can measure the concentration change of target molecules in real-time will become an innovative basic technology in medical research.

7.2 Prospects

In this study, although we demonstrated the feasibility of the sensor that can detect molecules of various sizes by realizing the cavity-sealed MEMS interferometer with a high surface-stress sensitivity, to make it practical as a quick and simple inspection device, the following tasks must be solved.

1. 【Acquisition of electrical response in MEMS interferometers】

To date, the responses of the sensors acquired have obtained sensor outputs as a shift amount in the reflection spectrum caused by the deflection of deformable membranes. However, this method requires a spectrometer to acquire the reflection spectra and an optical system that requires detailed alignment, which makes miniaturization difficult and limits the number of sensors that can be measured at a time. Therefore, by integrating the photodiode and source follower circuit into the Si substrate, the response from the sensor can be acquired using a voltage signal and solve the problem.

2. 【Development of a robust sensing system that implements a reference sensor and comparison circuits】

For precise measurements, environmental effects, such as changes in the intensity of the incident light due to contaminants in the sample and pressure and temperature changes should be removed, and only the output response when target molecules adsorb to the sensor should be acquired. This can be solved by simultaneously acquiring the output by a reference sensor that does not adsorb antibodies and reading only the differential signal.

3. 【Establishment of a patterning method for the simultaneous measurement of multiple target molecules】

We employed PMMA and polypyrrole as molecular adsorption layers for the detection of various molecules in the interferometer with cavity-sealed structures. However, to simultaneously measure different target molecules on a single chip, a sensor structure with a mixture of these molecular adsorption layers should be realized. Therefore, PMMA, which is used as a photoresist, can be solved through photolithography, while polypyrrole, which is formed on a conductive material, can be patterned using a lift-off process or by a formation technique using a shadow mask.

4. **【Optimization of electrochemical polymerization conditions during MIP film formation】**

The conditions for the formation of MIP films introduced to date have not been optimized, and the number of samples required to confirm the reproducibility is insufficient. Therefore, after optimizing the conditions, concentration dependence should be obtained while confirming the reproducibility.

References

- [1] National Institute of Population and Social Security Research, “Population Projections for Japan: 2016-2065.” [Online]. Available: http://www.ipss.go.jp/pp-zenkoku/j/zenkoku2017/pp29_ReportALL.pdf. [Accessed: 06-Nov-2020].
- [2] N. Hawkes, “Cancer survival data emphasise importance of early diagnosis,” *BMJ*, vol. 364, p. 1408, 2019.
- [3] “Point-of-Care Diagnostics Market Growing at a CAGR of 10.4%.” [Online]. Available: <https://www.marketsandmarkets.com/Market-Reports/point-of-care-diagnostic-market-106829185.html>. [Accessed: 28-Aug-2020].
- [4] D. L. Rosin and M. D. Okusa, “Dangers Within: DAMP Responses to Damage and Cell Death in Kidney Disease,” *J. Am. Soc. Nephrol.*, vol. 22, no. 3, pp. 416–425, 2011.
- [5] T. ting Du, T. Cui, H. mei Qiu, N. ru Wang, D. Huang, and X. hui Jiang, “Simultaneous determination of tryptophan, kynurenine, kynurenic acid and two monoamines in rat plasma by HPLC-ECD/DAD,” *J. Pharm. Biomed. Anal.*, vol. 158, pp. 8–14, 2018.
- [6] S. H. Kim, S. Iwai, S. Araki, S. Sakakihara, R. Iino, and H. Noji, “Large-scale femtoliter droplet array for digital counting of single biomolecules,” *Lab Chip*, vol. 12, no. 23, pp. 4986–4991, 2012.
- [7] Hiyoyuki Noji, “Digital Revolution of Bio-analysis.” [Online]. Available: https://www.jst.go.jp/pdf/pc201507_noji.pdf. [Accessed: 10-Nov-2020].
- [8] P. R. Bueno, L. M. Gonçalves, and F. C. Santos, “Electrogravimetric Analysis by Quartz-Crystal Microbalance on the Consumption of the Neurotransmitter Acetylcholine by Acetylcholinesterase,” *Anal. Lett.*, no. 46, pp. 258–265, 2013.
- [9] N. Kim, D. K. Kim, and Y. J. Cho, “Development of indirect-competitive quartz crystal microbalance immunosensor for C-reactive protein,” *Sensors Actuators, B Chem.*, vol. 143, no. 1, pp. 444–448, 2009.
- [10] Y. Uludağ and I. E. Tothill, “Development of a sensitive detection method of cancer biomarkers in human serum (75%) using a quartz crystal microbalance sensor and nanoparticles amplification system,” *Talanta*, vol. 82, no. 1, pp. 277–282, 2010.
- [11] S. Kurosawa, M. Nakamura, J. W. Park, H. Aizawa, K. Yamada, and M. Hirata, “Evaluation of a high-affinity QCM immunosensor using antibody fragmentation and 2-methacryloyloxyethyl phosphorylcholine (MPC) polymer,” *Biosens. Bioelectron.*, vol. 20, no. 6, pp. 1134–1139, 2004.
- [12] P. Ding, R. Liu, S. Liu, X. Mao, R. Hu, and G. Li, “Reusable gold nanoparticle enhanced QCM immunosensor for detecting C-reactive protein,” *Sensors Actuators, B Chem.*, vol. 188, pp. 1277–1283, 2013.
- [13] H. Aizawa *et al.*, “Detection of C-Reactive Protein in Serum Using Resonant Property of Quartz Crystal Microbalance,” *Electrochemistry*, vol. 74, no. 2, pp. 156–158, 2006.
- [14] T. Frisk, N. Sandström, L. Eng, W. van der Wijngaart, P. Månsson, and G. Stemme, “An integrated QCM-based narcotics sensing microsystem,” *Lab Chip*, vol. 8, no. 10, pp. 1648–1657, 2008.

- [15] R. Wang and Y. Li, "Hydrogel based QCM aptasensor for detection of avian influenza virus," *Biosens. Bioelectron.*, vol. 42, no. 1, pp. 148–155, 2013.
- [16] L. P. Wu, Y. F. Li, C. Z. Huang, and Q. Zhang, "Visual detection of Sudan dyes based on the plasmon resonance light scattering signals of silver nanoparticles," *Anal. Chem.*, vol. 78, no. 15, pp. 5570–5577, 2006.
- [17] K.-H. Lee, Y.-D. Su, S.-J. Chen, F.-G. Tseng, and G.-B. Lee, "Microfluidic systems integrated with two-dimensional surface plasmon resonance phase imaging systems for microarray immunoassay," *Biosens. Bioelectron.*, vol. 23, no. 4, pp. 466–472, 2007.
- [18] G. A. J. Besselink, R. P. H. Kooyman, P. J. H. J. Van Os, G. H. M. Engbers, and R. B. M. Schasfoort, "Signal amplification on planar and gel-type sensor surfaces in surface plasmon resonance-based detection of prostate-specific antigen," *Anal. Biochem.*, vol. 333, no. 1, pp. 165–173, 2004.
- [19] J.-W. Choi, D.-Y. Kang, Y.-H. Jang, H.-H. Kim, J. Min, and B.-K. Oh, "Ultra-sensitive surface plasmon resonance based immunosensor for prostate-specific antigen using gold nanoparticle–antibody complex," *Colloids Surfaces A Physicochem. Eng. Asp.*, vol. 313–314, pp. 655–659, 2008.
- [20] H. S. Jang, K. N. Park, C. D. Kang, J. P. Kim, S. J. Sim, and K. S. Lee, "Optical fiber SPR biosensor with sandwich assay for the detection of prostate specific antigen," *Opt. Commun.*, vol. 282, no. 14, pp. 2827–2830, 2009.
- [21] L. Huang *et al.*, "Prostate-specific antigen immunosensing based on mixed self-assembled monolayers, camel antibodies and colloidal gold enhanced sandwich assays," *Biosens. Bioelectron.*, vol. 21, no. 3, pp. 483–490, 2005.
- [22] P. Preechaburana, M. C. Gonzalez, A. Suska, and D. Filippini, "Surface Plasmon Resonance Chemical Sensing on Cell Phones," *Angew. Chemie*, vol. 124, no. 46, pp. 11753–11756, 2012.
- [23] M. O. Noor and U. J. Krull, "Silicon nanowires as field-effect transducers for biosensor development: A review," *Anal. Chim. Acta*, vol. 825, pp. 1–25, 2014.
- [24] A. Vacic, J. M. Criscione, N. K. Rajan, E. Stern, T. M. Fahmy, and M. A. Reed, "Determination of molecular configuration by debye length modulation," *J. Am. Chem. Soc.*, vol. 133, no. 35, pp. 13886–13889, 2011.
- [25] Y. Miyahara and T. Sakata, "Electrical Detection of Bio-molecular Recognition Using Insulated Gate Field Effect Transistors," *Journal-Surface Sci. Soc. Japan*, vol. 27, no. 1, pp. 13–20, 2006.
- [26] G. Zheng, X. P. A. Gao, and C. M. Lieber, "Frequency domain detection of biomolecules using silicon nanowire biosensors," *Nano Lett.*, vol. 10, no. 8, pp. 3179–3183, 2010.
- [27] D. Kang *et al.*, "Ultrasensitive mechanical crack-based sensor inspired by the spider sensory system," *Nature*, vol. 516, no. 7530, pp. 222–226, Dec. 2014.
- [28] G. Presnova *et al.*, "Biosensor based on a silicon nanowire field-effect transistor functionalized by gold nanoparticles for the highly sensitive determination of prostate specific antigen," *Biosens. Bioelectron.*, vol. 88, pp. 283–289, 2017.

- [29] Toshiya Sakata, "Biointerface control for label-free DNA sequencing based on semiconductor principles." [Online]. Available: https://shingi.jst.go.jp/past_abst/abst/p/10/1036/jst6.pdf. [Accessed: 10-Nov-2020].
- [30] Kazuhiko Matsumoto, "Realization of Quantum Nanodevices by Quantum Interface Control." [Online]. Available: https://www.jst.go.jp/kisoken/crest/research/nenpou/h24/05_matsumoto.pdf. [Accessed: 10-Nov-2020].
- [31] J. K. Gimzewski, C. Gerber, E. Meyer, and R. R. Schlittler, "Observation of a chemical reaction using a micromechanical sensor," *Chem. Phys. Lett.*, vol. 217, no. 5–6, pp. 589–594, Jan. 1994.
- [32] J. Homola, "Surface plasmon resonance sensors for detection of chemical and biological species," *Chem. Rev.*, vol. 108, no. 2, pp. 462–493, 2008.
- [33] F. Huber, H. P. Lang, J. Zhang, D. Rimoldi, and C. Gerber, "Nanosensors for cancer detection," *Swiss Med. Wkly.*, vol. 145, pp. 1–8, 2015.
- [34] G. Wu, R. H. Datar, K. M. Hansen, T. Thundat, R. J. Cote, and A. Majumdar, "Bioassay of prostate specific antigen using microcantilevers," *Nat. Biotechnol.*, vol. 19, no. 9, pp. 856–860, 2001.
- [35] K. Gruber, T. Horlacher, R. Castelli, A. Mader, P. H. Seeberger, and B. A. Hermann, "Cantilever Array Sensors Detect Specific Carbohydrate–Protein Interactions with Picomolar Sensitivity," *ACS Nano*, vol. 5, no. 5, pp. 3670–3678, 2011.
- [36] S. Wu *et al.*, "Highly sensitive nanomechanical assay for the stress transmission of carbon chain," *Sensors Actuators, B Chem.*, vol. 186, pp. 353–359, 2013.
- [37] S. T. Koev, R. Fernandes, W. E. Bentley, and R. Ghodssi, "A cantilever sensor with an integrated optical readout for detection of enzymatically produced homocysteine," *IEEE Trans. Biomed. Circuits Syst.*, vol. 3, no. 6, pp. 415–423, 2009.
- [38] Y. Arntz *et al.*, "Label-free protein assay based on a nanomechanical cantilever array," *Nanotechnology*, vol. 14, no. 1, pp. 86–90, 2002.
- [39] N. Backmann *et al.*, "A label-free immunosensor array using single-chain antibody fragments," *Proc. Natl. Acad. Sci. U. S. A.*, vol. 102, no. 41, pp. 14587–14592, 2005.
- [40] P. M. Kosaka *et al.*, "Detection of cancer biomarkers in serum using a hybrid mechanical and optoplasmonic nanosensor," *Nat. Nanotechnol.*, vol. 9, no. 12, pp. 1047–1053, 2014.
- [41] M. Yue, J. C. Stachowiak, and A. Majumdar, "Cantilever arrays for multiplexed mechanical analysis of biomolecular reactions," *Mech. Chem. Biosyst.*, vol. 1, no. 3, pp. 211–220, 2004.
- [42] J. Thaysen, A. D. Yal inkaya, P. Vettiger, and A. Menon, "Polymer-based stress sensor with integrated readout," *J. Phys. D. Appl. Phys.*, vol. 35, no. 21, pp. 2698–2703, 2002.
- [43] S. Satyanarayana, D. T. McCormick, and A. Majumdar, "Parylene micro membrane capacitive sensor array for chemical and biological sensing," *Sensors Actuators, B Chem.*, vol. 115, no. 1, pp. 494–502, 2006.
- [44] A. Jian *et al.*, "A PDMS surface stress biosensor with optimized micro-membrane: Fabrication and application," *Sensors Actuators, B Chem.*, vol. 242, pp. 969–976, 2017.

- [45] S. Sang *et al.*, “PDMS micro-membrane capacitance-type surface stress biosensors for biomedical analyses,” *Microelectron. Eng.*, vol. 134, pp. 33–37, 2015.
- [46] K. W. Wee *et al.*, “Novel electrical detection of label-free disease marker proteins using piezoresistive self-sensing micro-cantilevers,” *Biosens. Bioelectron.*, vol. 20, no. 10, pp. 1932–1938, 2005.
- [47] R. Katragadda, Z. Wang, W. Khalid, Y. Li, and Y. Xu, “Parylene cantilevers integrated with polycrystalline silicon piezoresistors for surface stress sensing,” *Appl. Phys. Lett.*, vol. 91, no. 8, 083505, pp. 1–3, 2007.
- [48] G. Yoshikawa, T. Akiyama, S. Gautsch, P. Vettiger, and H. Rohrer, “Nanomechanical Membrane-type Surface Stress Sensor,” *Nano Lett.*, vol. 11, no. 3, pp. 1044–1048, 2011.
- [49] G. Yoshikawa *et al.*, “Two dimensional array of piezoresistive nanomechanical Membrane-type Surface stress Sensor(MSS) with improved sensitivity,” *Sensors*, vol. 12, no. 11, pp. 15873–15887, 2012.
- [50] M. Omidi, M. Choolaei, F. Asjodi, F. Haghirsadat, and F. Yazdian, “Measurement of prostate specific antigen using self-sensing nanomechanical membrane,” *Procedia Eng.*, vol. 87, pp. 660–663, 2014.
- [51] K. Zheng *et al.*, “Optical Lever Based Parylene Cantilevers for Biochemical Sensing,” *Open Opt. J.*, vol. 2, no. 1, pp. 86–93, 2008.
- [52] K. Takahashi, H. Oyama, N. Misawa, K. Okumura, M. Ishida, and K. Sawada, “Surface stress sensor using MEMS-based Fabry-Perot interferometer for label-free biosensing,” *Sensors Actuators, B Chem.*, vol. 188, pp. 393–399, 2013.
- [53] Y. Masuya, R. Ozawa, M. Ishida, K. Sawada, and K. Takahashi, “Fast mechanical biosensing in liquid using mems Fabry-Perot interferometric surface-stress sensor,” *2015 Transducers - 2015 18th Int. Conf. Solid-State Sensors, Actuators Microsystems, TRANSDUCERS 2015*, pp. 1613–1616, 2015.
- [54] M. Omidi, M. Choolaei, F. Asjodi, and F. Haghirsadat, “Measurement of Prostate Specific Antigen Using Self-Sensing Nanomechanical Membrane,” *Procedia Eng.*, vol. 87, pp. 660–663, 2014.
- [55] S. B. Patil *et al.*, “Decoupling competing surface binding kinetics and reconfiguration of receptor footprint for ultrasensitive stress assays,” *Nat. Nanotechnol.*, vol. 10, no. 10, pp. 899–907, 2015.
- [56] Y. Masuya, K. Takahashi, R. Ozawa, T. Hizawa, M. Ishida, and K. Sawada, “Highly sensitive MEMS Fabry-Perot interferometric biosensor with Ag half-mirror and high responsivity photodiode,” *Proc. 7th Asia-Pacific Conf. Transducers Micro/Nano Technol.*, 2014.
- [57] A. García-Juárez, R. Gómez-Colín, F. Gracia-Témich, and C. Gutiérrez-Martínez, “Design of multi-layer mirrors for measuring optical phase modulation at 1300nm,” *Opt. Laser Technol.*, vol. 41, no. 5, pp. 550–556, 2009.
- [58] P. Hajireza, K. Krause, M. Brett, and R. Zemp, “Glancing angle deposited nanostructured film Fabry-Perot etalons for optical detection of ultrasound,” *Opt. Express*, vol. 21, no. 5, pp. 6391–6400, 2013.
- [59] C. E. Lee, W. N. Gibler, R. A. Atkins, and H. F. Taylor, “In-line fiber Fabry-Perot interferometer with high-reflectance internal mirrors,” *J. Light. Technol.*, vol. 10, no. 10, pp. 1376–1379, 1992.

- [60] C. Y. Lo, H. Fujita, and H. Toshiyoshi, "Toward realization of transmissive display by MEMS etalon," *IEICE Electron. Express*, vol. 5, no. 9, pp. 326–331, 2008.
- [61] Y. Moriyama and K. Takeda, "Disruption of Protein Structure by the Light Irradiation," *J. Illum. Eng. Inst. Japan*, vol. 78, no. 6, pp. 305–307, 1994.
- [62] K. Takeda and Y. Moriyama, "Unavoidable time-dependent ellipticity changes of proteins in the current CD measurements," *J. Am. Chem. Soc.*, vol. 113, no. 17, pp. 6700–6701, 1991.
- [63] H. Onoyama, C. Ryu, M. Suguri, and M. Iida, "Stability of 2170nm as a Key Wavelength for Protein Analysis by Near Infrared Spectroscopy," *Proceedings of the 4th Asian Conference on Precision Agriculture*, vol. 38, no. 9, pp. 850–857, 2011.
- [64] T. Herold *et al.*, "Elevated levels of IL-6 and CRP predict the need for mechanical ventilation in COVID-19," *J. Allergy Clin. Immunol.*, vol. 146, no. 1, pp. 128–136, 2020.
- [65] J. Bausells, "Piezoresistive cantilevers for nanomechanical sensing," *Microelectron. Eng.*, vol. 145, pp. 9–20, 2015.
- [66] M. G. Von Muhlen, N. D. Brault, S. M. Knudsen, S. Jiang, and S. R. Manalis, "Label-free biomarker sensing in undiluted serum with suspended microchannel resonators," *Anal. Chem.*, vol. 82, no. 5, pp. 1905–1910, 2010.
- [67] M. Yue, J. C. Stachowiak, H. Lin, R. Datar, R. Cote, and A. Majumdar, "Label-free protein recognition two-dimensional array using nanomechanical sensors," *Nano Lett.*, vol. 8, no. 2, pp. 520–524, 2008.
- [68] K. S. Hwang, H. K. Jeon, S. M. Lee, S. K. Kim, and T. S. Kim, "Quantification of disease marker in undiluted serum using an actuating layer-embedded microcantilever," *J. Appl. Phys.*, vol. 105, no. 10, 102017, pp. 1–7, 2009.
- [69] T. Hayashi and M. Hara, "Nonfouling Self-Assembled Monolayers: Mechanisms Underlying Protein and Cell Resistance," *Curr. Phys. Chem.*, vol. 1, no. 2, pp. 90–98, 2011.
- [70] H. Wang, S. Chen, Lingyan Li, and S. Jiang, "Improved Method for the Preparation of Carboxylic Acid and Amine Terminated Self-Assembled Monolayers of Alkanethiolates," *Langmuir*, vol. 21, no. 7, pp. 2633–2636, 2005.
- [71] H. Gao, K. R. Buchapudi, A. Harms-Smyth, Marvin K. Schulte, A. Xiaohe Xu, and Hai-Feng Ji, "Improved Surface Modification Approach for Micromechanical Biosensors," *Langmuir*, vol. 24, no. 2, pp. 345–349, 2008.
- [72] S. Maruyama, T. Hizawa, K. Takahashi, and K. Sawada, "Optical-Interferometry-Based CMOS-MEMS Sensor Transduced by Stress-Induced Nanomechanical Deflection," *Sensors*, vol. 18, no. 1, 138, pp. 1–10, 2018.
- [73] Y. Choi, T. Takahashi, M. Taki, K. Sawada, and K. Takahashi, "Label-free attomolar protein detection using a MEMS optical interferometric surface-stress immunosensor with a freestanding PMMA / parylene-C nanosheet," *Biosens. Bioelectron.*, vol. 172, no. 15, 112778, pp. 1–7, 2021.
- [74] M. Rowinska, S. M. Kelleher, F. Soberon, A. J. Ricco, and S. Daniels, "Fabrication and characterisation of spin coated oxidised PMMA to provide a robust surface for on-chip assays," *J. Mater. Chem. B*, vol. 3, no. 1, pp. 135–143, 2015.

- [75] W. Miekisch, J. K. Schubert, and G. F. E. Noeldge-Schomburg, "Diagnostic potential of breath analysis - Focus on volatile organic compounds," *Clin. Chim. Acta*, vol. 347, pp. 25–39, 2004.
- [76] S. Das and M. Pal, "Non-Invasive Monitoring of Human Health by Exhaled Breath Analysis: A Comprehensive Review," *J. Electrochem. Soc.*, vol. 167, no. 3, 037562, pp. 1–22, 2020.
- [77] C. Lourenço and C. Turner, "Breath Analysis in Disease Diagnosis: Methodological Considerations and Applications," *Metabolites*, vol. 4, no. 2, pp. 465–498, 2014.
- [78] S. Das, S. Pal, and M. Mitra, "Significance of Exhaled Breath Test in Clinical Diagnosis: A Special Focus on the Detection of Diabetes Mellitus," *J. Med. Biol. Eng.*, vol. 36, no. 5, pp. 605–624, 2016.
- [79] Y. Zhang, J. Li, G. An, and X. He, "Highly porous SnO₂ fibers by electrospinning and oxygen plasma etching and its ethanol-sensing properties," *Sensors Actuators, B Chem.*, vol. 144, no. 1, pp. 43–48, 2010.
- [80] M. Righettoni, A. Tricoli, and S. E. Pratsinis, "Si:WO₃ sensors for highly selective detection of acetone for easy diagnosis of diabetes by breath analysis," *AIChE Annu. Meet. Conf. Proc.*, vol. 82, no. 9, pp. 3581–3587, 2010.
- [81] A. T. Güntner, S. Abegg, K. Wegner, and S. E. Pratsinis, "Zeolite membranes for highly selective formaldehyde sensors," *Sensors Actuators, B Chem.*, vol. 257, pp. 916–923, 2018.
- [82] A. T. Güntner, S. Abegg, K. Königstein, P. A. Gerber, A. Schmidt-Trucksäss, and S. E. Pratsinis, "Breath sensors for health monitoring," *ACS Sensors*, vol. 4, no. 2, pp. 268–280, 2019.
- [83] Q. Wan *et al.*, "Fabrication and ethanol sensing characteristics of ZnO nanowire gas sensors Fabrication and ethanol sensing characteristics of ZnO nanowire gas sensors," vol. 84, no. 18, pp. 3654–3656, 2004.
- [84] D. Shlenkevitch, S. Stolyarova, T. Blank, I. Brouk, and Y. Nemirovsky, "Novel miniature and selective combustion-type CMOS gas sensor for gas-mixture analysis-Part 1: Emphasis on chemical aspects," *Micromachines*, vol. 11, no. 4, pp. 1–14, 2020.
- [85] J. E. Ellis, U. Green, D. C. Sorescu, Y. Zhao, and A. Star, "Indium oxide-single-walled carbon nanotube composite for ethanol sensing at room temperature," *J. Phys. Chem. Lett.*, vol. 6, no. 4, pp. 712–717, Feb. 2015.
- [86] D. Zhang, J. Liu, H. Chang, A. Liu, and B. Xia, "Characterization of a hybrid composite of SnO₂ nanocrystal-decorated reduced graphene oxide for ppm-level ethanol gas sensing application," *RSC Adv.*, vol. 5, no. 24, pp. 18666–18672, 2015.
- [87] D. Sebok and I. Dékány, "ZnO₂ nanohybrid thin film sensor for the detection of ethanol vapour at room temperature using reflectometric interference spectroscopy," *Sensors Actuators, B Chem.*, vol. 206, pp. 435–442, 2015.
- [88] H. Guo, X. Chen, Y. Yao, G. Du, and H. Li, "Detection of ethanol and methanol vapors using polymer-coated piezoresistive Si bridge," *Sensors Actuators, B Chem.*, vol. 155, no. 2, pp. 519–523, 2011.
- [89] K. Shiba, R. Tamura, G. Imamura, and G. Yoshikawa, "Data-driven nanomechanical sensing: specific information extraction from a complex system," *Sci. Rep.*, vol. 7, no. 1, pp. 1–12, 2017.

- [90] O. Lupan *et al.*, “Single and networked CuO nanowires for highly sensitive p-type semiconductor gas sensor applications,” *Phys. Status Solidi - Rapid Res. Lett.*, vol. 10, no. 3, pp. 260–266, 2016.
- [91] H. Guo, L. Lou, X. Chen, and C. Lee, “PDMS-coated piezoresistive NEMS diaphragm for chloroform vapor detection,” *IEEE Electron Device Lett.*, vol. 33, no. 7, pp. 1078–1080, 2012.
- [92] P. Carneiro, J. Loureiro, C. Delerue-matos, S. Morais, and C. Pereira, “Alzheimer’s disease : Development of a sensitive label-free electrochemical immunosensor for detection of amyloid beta peptide,” *Sensors Actuators B. Chem.*, vol. 239, pp. 157–165, 2017.
- [93] T. Takahashi, T. Hizawa, M. Nobuo, M. Taki, K. Sawada, and K. Takahashi, “Surface stress sensor based on MEMS Fabry–Perot interferometer with high wavelength selectivity for label-free biosensing,” *J. Micromechanics Microengineering*, vol. 28, no. 5, 054002, pp. 1–10, 2018.
- [94] H. Noh, K. Moon, A. Cannon, P. J. Hesketh, and C. P. Wong, “Wafer bonding using microwave heating of parylene intermediate layers,” *J. Micromechanics Microengineering*, vol. 14, no. 4, pp. 625–631, 2004.
- [95] H. Bernheimer, W. Birkmayer, O. Hornykiewicz, K. Jellinger, and F. Seitelberger, “Brain dopamine and the syndromes of Parkinson and Huntington Clinical, morphological and neurochemical correlations,” *J. Neurol. Sci.*, vol. 20, no. 4, pp. 415–455, 1973.
- [96] W. Z. Wan Ismail, G. Liu, K. Zhang, E. M. Goldys, and J. M. Dawes, “Dopamine sensing and measurement using threshold and spectral measurements in random lasers,” *Opt. Express*, vol. 24, no. 2, pp. 85–91, 2016.
- [97] K. Buchapudi, X. Xu, Y. Ataian, H. Ji, and M. Schulte, “Micromechanical measurement of AChBP binding for label-free drug discovery,” *Analyst*, vol. 137, pp. 263–268, 2012.
- [98] L. Syedmoradi, A. Ahmadi, M. L. Norton, and K. Omidfar, “A review on nanomaterial-based field effect transistor technology for biomarker detection,” *Microchim. Acta*, vol. 186, no. 11, pp. 1–23, 2019.
- [99] T. Sakata, S. Nishitani, and T. Kajisa, “Molecularly imprinted polymer-based bioelectrical interfaces with intrinsic molecular charges,” *RSC Adv.*, vol. 10, no. 29, pp. 16999–17013, 2020.
- [100] S. Ansari and S. Masoum, “Molecularly imprinted polymers for capturing and sensing proteins: Current progress and future implications,” *TrAC - Trends Anal. Chem.*, vol. 114, pp. 29–47, 2019.
- [101] D. S. Janiak and P. Kofinas, “Molecular imprinting of peptides and proteins in aqueous media,” *Anal. Bioanal. Chem.*, vol. 389, no. 2, pp. 399–404, 2007.
- [102] Z. Xia *et al.*, “Facile synthesis of polydopamine-coated molecularly imprinted silica nanoparticles for protein recognition and separation,” *Biosens. Bioelectron.*, vol. 47, pp. 120–126, 2013.
- [103] X. Wang, J. Yu, J. Li, Q. Kang, D. Shen, and L. Chen, “Quantum dots based imprinting fluorescent nanosensor for the selective and sensitive detection of phycocyanin: A general imprinting strategy toward proteins,” *Sensors Actuators, B Chem.*, vol. 255, pp. 268–274, 2018.
- [104] M. Zhang, X. Zhang, X. He, L. Chen, and Y. Zhang, “A self-assembled polydopamine film on the surface of magnetic nanoparticles for specific capture of protein,” *Nanoscale*, vol. 4, no. 10, pp. 3141–3147, 2012.

- [105] X. Tu *et al.*, “Molecularly imprinted polymer-based plasmonic immunosandwich assay for fast and ultrasensitive determination of trace glycoproteins in complex samples,” *Anal. Chem.*, vol. 88, no. 24, pp. 12363–12370, 2016.
- [106] L. Li, Y. Lu, Z. Bie, H. Y. Chen, and Z. Liu, “Photolithographic boronate affinity molecular imprinting: A general and facile approach for glycoprotein imprinting,” *Angew. Chemie - Int. Ed.*, vol. 52, no. 29, pp. 7451–7454, 2013.
- [107] S. Viswanathan, C. Rani, S. Ribeiro, and C. Delerue-Matos, “Molecular imprinted nanoelectrodes for ultra sensitive detection of ovarian cancer marker,” *Biosens. Bioelectron.*, vol. 33, no. 1, pp. 179–183, 2012.
- [108] P. Jolly, V. Tamboli, R. L. Harniman, P. Estrela, C. J. Allender, and J. L. Bowen, “Aptamer-MIP hybrid receptor for highly sensitive electrochemical detection of prostate specific antigen,” *Biosens. Bioelectron.*, vol. 75, pp. 188–195, 2016.
- [109] F. T. C. Moreira, M. J. M. S. Ferreira, J. R. T. Puga, and M. G. F. Sales, “Screen-printed electrode produced by printed-circuit board technology. Application to cancer biomarker detection by means of plastic antibody as sensing material,” *Sensors Actuators, B Chem.*, vol. 223, pp. 927–935, 2016.
- [110] M. Bossert *et al.*, “Microelectrospotting as a new method for electrosynthesis of surface-imprinted polymer microarrays for protein recognition,” *Biosens. Bioelectron.*, vol. 73, pp. 123–129, 2015.
- [111] T. C. Tsai, H. Z. Han, C. C. Cheng, L. C. Chen, H. C. Chang, and J. J. J. Chen, “Modification of platinum microelectrode with molecularly imprinted over-oxidized polypyrrole for dopamine measurement in rat striatum,” *Sensors Actuators, B Chem.*, vol. 171–172, pp. 93–101, 2012.

Acknowledgements

First, I would like to express my sincere gratitude to my supervisor Associate Professor Kazuhiro Takahashi of the Department of Electrical and Electronic Information Engineering, Toyohashi University of Technology. His support through balanced guidance, encouragement, and valuable suggestions has been invaluable for me for the continuation of this research.

Additionally, I express my sincere gratitude to my supervisor, Leading Program Professor Hiroyuki Ohta, Faculty of Pharmacy, National Defense Medical College, and Professor Katsuyuki Machida, Department of Engineering, Tokyo Institute of Technology, and Professor Toshiya Sakata, Department of Materials Engineering, University of Tokyo, and Professor Hiromu Ishii, Research Administration Centre, Toyohashi University of Technology, and Professor Toshinori Fujie, School of Life Science and Technology, Tokyo Institute of Technology, for precise reviews.

I would like to express my sincere thanks and gratitude to Professor Makoto Ishida, Professor Kazuaki Sawada, Associate Professor Toshihiko Noda, Assistant Professor Yong-Joon Choi, Toyohashi University of Technology, and Lecturer Tatsuya Iwata, Department of Electrical and Electronic Engineering, Toyama Prefectural University, for their valuable suggestions and discussions throughout my research work.

I would like to express cordial thanks to Technical Engineer Dr Takeshi Hizawa, PhD You-Na Lee (currently Samsung Electronics), my senior advisor Yoshihiro Masuya (currently SCREEN Holdings), and Assistant Technical Staff Miki Taki, PhD Yoshihiro Kubota (currently KIOXIA Holdings), and PhD Hayato Kumagai (currently Sony), for their valuable suggestions and discussions throughout my research on device fabrication and biological experiment.

I would like to thank Associate Professor Toshiaki Hattori of Toyohashi University of Technology for reviewing this thesis.

Furthermore, I like to thank the other member of the research group: Yoshiaki Murata, Kazuki Komatsu, Hideo Doi, Junpei Uesaka, Ryouto Kanamori, Chinatsu Kawakami, Koutaro Sakamoto, Sylvia Loo Mei Lin, Yukihiro Tatsumi, Tomoya Ide, Hayato Muraguchi, Tay Shan Wei, Yuto Honda, Fumitaka Endo, Rintaro Tsubouchi, Tomoya Maeda, Kenta Senbo, and Ryomei Wada.

Finally, I wish to offer thanks to my family for supporting my life.

List of Publications & Awards

Journal Papers:

1. ○ **T. Takahashi**, T. Hizawa, M. Nobuo, M. Taki, K. Sawada, and K. Takahashi, “Surface stress sensor based on MEMS Fabry-Perot interferometer with high wavelength selectivity for label-free biosensing”, *J. Micromechanics Microengineering*, vol. 28, no. 5, pp. 054002-054012, 2018.
2. ○ **T. Takahashi**, Yoon-Joon Choi, K. Sawada, and K. Takahashi, “A ppm ethanol sensor based on Fabry-Perot interferometric surface stress transducer at room temperature”, *Sensors*, vol. 20, no. 23, pp. 1-14, 2020.
3. Y. Choi, ○ **T. Takahashi**, M. Taki, K. Sawada, and K. Takahashi, “Biosensors and Bioelectronics Label-free attomolar protein detection using a MEMS optical interferometric surface-stress immunosensor with a freestanding PMMA / parylene-C nanosheet,” *Biosens. Bioelectron.*, vol. 172, no. 15, pp. 1-7, 2021.

International Conference Proceedings:

1. ○ **T. Takahashi**, T. Hizawa, M. Nobuo, M. Taki, K. Sawada, and K. Takahashi, “Fabry-Perot interferometric surface-stress sensor with high wavelength selectivity for label-free biosensing”, *Solid-State Sensors, Actuators and Microsystems (Transducers’17)*, pp.476-479, 2017.
2. ○ **T. Takahashi**, Yoon-Joon Choi, S. Maruyama, M. Taki, K. Sawada, and K. Takahashi, “Fabrication of cavity-sealed optical interferometric surface stress biosensor by thin film transfer technique”, *Solid-State Sensors, Actuators and Microsystems (Transducers’19)*, pp.182-185, 2019.

Domestic Conference Proceedings:

1. ○ **T. Takahashi**, Y. Masuya, H. Hayato, K. Sawada and K. Takahashi, “Improving wavelength selectivity of MEMS Fabry-Perot interferometric biosensor using Au half mirrors”, *IEICE General Conference, IEICE Technical Report*, Vol.116 No.181, pp.41-45, 2016.
2. ○ **T. Takahashi**, Y. Masuya, H. Hayato, T.Hizawa, K. Sawada and K. Takahashi, “Design and fabrication of MEMS Fabry-Perot interferometric surface stress sensor with high wavelength selectivity”, *Proc. 77th JSAP Autumn Meet*, 15p-B10-7, 2016.

3. ○ **T. Takahashi**, T. Hizawa, N, Misawa, M. Taki, K. Sawada and K. Takahashi, “Fabrication of MEMS optical interferometric surface-stress sensor with high wavelength selectivity for label-free biosensing”, Proc. 64th JSAP Spring Meet., 16p-F205-11, 2017.
4. ○ **T. Takahashi**, T. Hizawa, N, Misawa, M. Taki, K. Sawada and K. Takahashi, “Fabrication and evaluation of MEMS optical interferometric biosensor with high wavelength selectivity”, IEICE General Conference, IEICE Technical Report, vol.117, no.172, pp. 5-8, 2017.
5. ○ **T. Takahashi**, T. Hizawa, N, Misawa, M. Taki, K. Sawada and K. Takahashi, “Fabrication of MEMS optical interferometric surface stress sensor with high wavelength selectivity for label-free biosensing”, The 34th sensor symposium, 02pm1-P-239, 2017.
6. ○ **T. Takahashi**, Yoon-Joon Choi, S. Maruyama, T. Miki, K. Sawada, K. Takahashi, “Evaluation of antigen-antibody reaction on MEMS optical interferometric surface-stress sensor”, Proc. 65th JSAP Spring Meet., 17a-F306-5, 2018.
7. ○ **T. Takahashi**, Yoon-Joon Choi, S. Maruyama, T. Miki, K. Sawada, K. Takahashi, “Fabrication of cavity-sealed optical interferometric surface stress biosensor by thin film transfer technique”, Proc. 65th JSAP Spring Meet., 10p-S421-4, 2019.
8. ○ **T. Takahashi**, Yoon-Joon Choi, S. Maruyama, M. Taki, K. Sawada, and K. Takahashi, “Fabrication and evaluation of the cavity-sealed MEMS interferometric biosensor with high surface stress sensitivity”, IEEJ Technical Meeting on Sensors and Micromachines, BMS-19-038, pp. 47-51, 2019.
9. R. Kanamori, Yoon-Joon Choi, ○ **T. Takahashi**, M. Taki, K. Sawada, and K. Takahashi, “Label-free detection of cancer marker by optical interferometric surface stress biosensor”, Proc. 80th JSAP Autumn Meet, 19p-PB1-30, 2019
10. ○ **T. Takahashi**, Yoon-Joon Choi, S. Maruyama, M. Taki, K. Sawada, and K. Takahashi, “Fabrication and evaluation of MEMS optical interferometric surface stress sensor with cavity-sealed structure using parylene bonding technique”, Proc. The 36th sensor symposium, 19pm5-PS3-10 2019.
11. ○ **T. Takahashi**, H Ohta, T. Fujie, K. Sawada, and K. Takahashi, “Fabrication of MEMS optical interferometric surface stress biosensor using molecular imprinting for label-free detection of neurotransmitter”, Proc. 81th JSAP Autumn Meet, 8p-Z12-12, 2020.

12. R. Kanamori, Yoon-Joon Choi, ○ **T. Takahashi**, M. Taki, K. Sawada, and K. Takahashi, “Fabrication of Optical Interferometric Surface Stress Biosensor Using Glutaraldehyde Crosslinking”, The 37th sensor symposium, 28A3-SS3-5, 2020.
13. ○ **T. Takahashi**, H Ohta, T. Fujie, K. Sawada, and K. Takahashi, “Fabrication and evaluation of MEMS optical interferometric surface stress sensor by molecular imprinting for label free detection of neurotransmitter”, Proc. The 12th Symposium on Integrated MEMS Technology, 28A3-AP-2, 2020.

Awards:

1. Institute of Electronics, Information and Communication Engineers (IEICE) Study Group of Electron Device, Excellent Presentation Award, 2017.
2. Institute of Electrical Engineers of Japan (IEEJ), Excellent Presentation Award, 2020.
3. Study Group of the integrated MEMS, Research Encouragement Award, 2021.

Others:

1. Japan Society for the Promotion of Science Research Fellow (DC2, Working for April 2019–March 2021)
2. OPERA Multi-Modal Sensing Co-Creation Consortium Research Assistant (Working for May 2020–March 2021)
3. Newspaper Article on High-Sensitivity Gas Sensor in this study (Electronic Device Industry News, January 21st, 2021)

Appendix A Process chart for MEMS interferometer with Au half-mirrors

Table A1. Fabrication procedure of MEMS interferometric surface stress sensor with Au half-mirrors structure for high wavelength selectivity

No.	Step	Condition	Time
1	Photolithography for stepper mark (1)	(1) Bake before coating 160°C (2) Spin-coat ip3100 with OAP surfactant (3) Pre-bake 110°C (4) Exposure (5) Developing with NMD-3, rinse with H ₂ O (6) Post-bake 120°C	90 sec 85.5 sec 90 sec 0.3 sec 160 sec 5 min
2	Stepper mark etching	Si-RIE 10 Pa Parameter 6 CF ₄ :15 sccm [cc(cm ³)min]	5 min
3	Resist removal	(1) H ₂ SO ₄ :H ₂ O ₂ =1:3 boil (2) DIW	10 min 10 min
4	Cleaning before oxidation	(1) HCl:H ₂ O ₂ :DIW=1:1:6,boil (2) DIW	10 min 10 min
5	Protective oxidation before ion implantation	OX1 1000°C SiO ₂ 50 nm (2) Dry (O ₂ = 250 l/hr) (3) Anneal (N ₂ = 250 l/hr)	60 min 10 min
6	Photolithography for n-well formation (2)	(1) Bake before coating 160°C (2) Spin-coat ip3100 with OAP surfactant (3) Pre-bake 110°C (4) Exposure (5) Developing with NMD-3, rinse with H ₂ O (6) Post-bake 120°C	90 sec 85.5 sec 90 sec 0.3 sec 160 sec 5 min
7	Ion implantation for forming n-well	PH ₃ , 150 keV Dose amount 1.0×10 ¹²	

8	Resist removal	(1) H ₂ SO ₄ :H ₂ O ₂ =1:3 boil (2) DIW	10 min 10 min
9	Pretreatment of drive-in	(1) HCl:H ₂ O ₂ :DIW=1:1:6,boil (2) DIW	10 min 10 min
10	Drive-in	OX6 1150°C Anneal (N ₂ = 250 l/hr)	9 hours
11	SiO ₂ removal	(1) BHF (2) DIW	60 sec 10 min
12	Cleaning before oxidation	(1) HCl:H ₂ O ₂ :DIW=1:1:6,boil (2) DIW	10 min 10 min
13	Field oxidation	OX1 1000°C SiO ₂ 800 nm (1) Wet (O ₂ = 250 l/hr + H ₂ =250 l/hr) (2) Dry (O ₂ = 250 l/hr) (3) Anneal (N ₂ = 250 l/hr)	4 hours 10 min 10 min
14	Photolithography for active area formation (3)	(1) Bake before coating 160°C (2) Spin-coat ip3100 with OAP surfactant (3) Pre-bake 110°C (4) Exposure (5) Developing with NMD-3, rinse with H ₂ O (6) Post-bake 120°C	90 sec 85.5 sec 90 sec 0.3 sec 160 sec 5 min
15	Field SiO ₂ removal	(1) O ₂ plasma 200W, O ₂ 100 sccm, 20Pa (2) BHF (3) DIW	1 min 30 sec 9 min 50 sec 10 min
16	Resist removal	(1) H ₂ SO ₄ :H ₂ O ₂ =1:3 boil (2) DIW	10 min 10 min
17	Pretreatment of protective oxidation	(1) HCl:H ₂ O ₂ :DIW=1:1:6 boil (2) DIW	10 min 10 min
18	Protective oxidation	OX1 1000°C SiO ₂ 50 nm (1) Dry (O ₂ = 250 l/hr) (2) Anneal (N ₂ = 250 l/hr)	60 min 10 min

19	Photolithography for substrate contact (4)	(1) Bake before coating 160°C (2) Spin-coat ip3100 with OAP surfactant (3) Pre-bake 110°C (4) Exposure (5) Developing with NMD-3, rinse with H ₂ O (6) Post-bake 120°C	90 sec 85.5 sec 90 sec 0.3 sec 160 sec 5 min
20	Ion implantation	BF ₄ , 60 keV, 1.0×10 ¹³	
21	Resist removal	(1) H ₂ SO ₄ :H ₂ O ₂ =1:3 boil (2) DIW	10 min 10 min
22	Photolithography for n ⁺ formation (5)	(1) Bake before coating 160°C (2) Spin-coat ip3100 with OAP surfactant (3) Pre-bake 110°C (4) Exposure (5) Developing with NMD-3, rinse with H ₂ O (6) Post-bake 120°C	90 sec 85.5 sec 90 sec 0.3 sec 160 sec 5 min
23	Ion implantation	PH ₃ , 60 keV, 4.0×10 ¹⁵	
24	Resist removal	O ₂ plasma 600W O ₂ flow 2.8, 1.6Torr SAMCO	30 min
25	Resist removal	(1) H ₂ SO ₄ :H ₂ O ₂ =1:3 boil (2) DIW	10 min 10 min
26	Photolithography for removal passivation SiO ₂ (6)	(1) Bake before coating 160°C (2) Spin-coat ip3100 with OAP surfactant (3) Pre-bake 110°C (4) Exposure (5) Developing with NMD-3, rinse with H ₂ O (6) Post-bake 120°C	90 sec 85.5 sec 90 sec 0.3 sec 160 sec 5 min

27	Removal passivation SiO ₂	(1) O ₂ plasma 100 W, O ₂ 50 sccm, 10 Pa (2) BHF (3) DIW	1 min 2 min 10 sec 10 min
28	Resist removal	(1) H ₂ SO ₄ :H ₂ O ₂ =1:3 boil (2) DIW	10 min 10 min
29	Pretreatment of oxidation	(1) NH ₄ OH:H ₂ O ₂ :H ₂ O=1:1:6 boil (2) DIW (3) HCl:H ₂ O ₂ :H ₂ O=1:1:6 boil (4) DIW (5) HF:H ₂ O=1:50 (6) DIW	10 min 10 min 10 min 10 min 15 sec 10 min
30	Oxidation	OX4 1000°C SiO ₂ 200 nm (2) Wet (O ₂ = 250 l/hr + H ₂ =250 l/hr) (3) Dry (O ₂ = 250 l/hr) (4) Anneal (N ₂ = 250 l/hr)	X min 10 min 10 min
31	Photolithography for bottom electrode formation (7)	(1) Bake before coating 160°C (2) Spin-coat ip3100 with OAP surfactant (3) Pre-bake 110°C (4) Exposure (5) Developing with NMD-3, rinse with H ₂ O (6) Post-bake 120°C	90 sec 85.5 sec 90 sec 0.3 sec 160 sec 5 min
32	Au evaporation	(1) Ti EB evaporation 5 nm (Emission current:50 mA) (2) Au EB evaporation 50 nm (Emission current:70 mA)	6 min 10 min
33	Lift off	(1) Acetone (2) IPA (Ultrasonic cleaning, output level:100%) (3) IPA (Ultrasonic cleaning, output	60 min 3 min 3 min

		level:100%) (4) DIW	5 min
34	Amorphous Si evaporation	Si EB evaporation 350 nm (Emission current:160 mA)	56 min
35	Photolithography for sacrificial layer formation (8)	(1) Bake before coating 160°C (2) Spin-coat ip3100 with OAP surfactant (3) Pre-bake 110°C (4) Exposure (5) Developing with NMD-3, rinse with H ₂ O (6) Post-bake 120°C	90 sec 85.5 sec 90 sec 0.3 sec 160 sec 5 min
36	Amorphous Si etching	F-RIE SF ₆ 10 sccm, 10 Pa, 100 W (Recipe 6)	4 min
37	Resist removal	O ₂ ashing or Remover PG	10 min
38	Plasma enhanced CVD	PECVD nitride Si ₃ N ₄ , 300 nm	11.5 min
39	Photolithography for removing nitride at contact and dicing line area (9)	(1) Bake before coating 160°C (2) Spin-coat ip3100 with OAP surfactant (3) Pre-bake 110°C (4) Exposure (5) Developing with NMD-3, rinse with H ₂ O (6) Post-bake 120°C	90 sec 85.5 sec 90 sec 0.3 sec 160 sec 5 min
40	Nitride removal	F-RIE O ₂ 5 sccm, CF ₄ 20 sccm, 4 Pa, 100 W	3 min
41	Resist removal	(1) Remover PG 60°C (2) Remover PG (Ultrasonic cleaning, output level:100%) (3) IPA (4) DIW	5 min 2 min 2 min 5 min

42	Photolithography for contact area formation (10)	(1) Bake before coating 160°C (2) Spin-coat ip3100 with OAP surfactant (3) Pre-bake 110°C (4) Exposure (5) Developing with NMD-3, rinse with H ₂ O (6) Post-bake 120°C	90 sec 85.5 sec 90 sec 0.3 sec 160 sec 5 min
43	Contact area etching (SiO ₂ removal)	F-RIE CHF ₃ 45 sccm, 3 Pa, 100 W	25 min
44	Resist removal	(1) Remover PG 60°C (2) Remover PG (Ultrasonic cleaning, output level:100%) (3) IPA (4) DIW	5 min 2 min 2 min 5 min
45	Pretreatment of sputtering	F-RIE CHF ₃ 45 sccm	15 sec
46	Al sputtering	Ar 5×10 ⁻¹ Pa、RF 1 kW 800 nm	17 min
47	Photolithography for Al wiring (11)	(1) Bake before coating 160°C (2) Spin-coat ip3100 with OAP surfactant (3) Pre-bake 110°C (4) Exposure (5) Developing with NMD-3, rinse with H ₂ O (6) Post-bake 120°C	90 sec 85.5 sec 90 sec 0.24 sec 160 sec 5 min
48	Al etching	(1) H ₃ PO ₄ :CH ₃ COOH:HNO ₃ = 250:20:3 55±5°C (2) DIW	~ 4 min 10 min
49	Resist removal	(1) Remover PG 60°C (2) IPA (4) DIW	5 min 2 min 5 min

50	Photolithography for nitride removal on sensing area, release holes, TEG (12)	(1) Bake before coating 160°C (2) Spin-coat ip3100 with OAP surfactant (3) Pre-bake 110°C (4) Exposure (5) Developing with NMD-3, rinse with H ₂ O (6) Post-bake 120°C	90 sec 85.5 sec 90 sec 0.3 sec 160 sec 5 min
51	Nitride removal	F-RIE O ₂ 5 sccm, CF ₄ 20 sccm, 4 Pa, 100 W	3 min
52	Resist removal	(1) Remover PG 60°C (2) Remover PG (Ultrasonic cleaning, output level:100%) (3) IPA (4) DIW	5 min 2 min 2 min 5 min
53	Photolithography for upper electrode lift off (13)	(1) Bake before coating 160°C (2) Spin-coat ip3100 with OAP surfactant (3) Pre-bake 110°C (4) Exposure (5) Developing with NMD-3, rinse with H ₂ O (6) Post-bake 120°C	90 sec 85.5 sec 90 sec 0.3 sec 160 sec 5 min
54	Au evaporation	(1) Ti EB evaporation 5 nm (Emission current:50 mA) (2) Au EB evaporation 50 nm (Emission current:70 mA)	6 min 10 min
55	Upper electrode lift off	(1) Acetone (2) IPA (Ultrasonic cleaning, output level:100%) (2) IPA (Ultrasonic cleaning, output level:100%) (4) DIW	60 min 3 min 3 min 5 min

56	Silane coupling treatment	(1) IPA:H ₂ O:A-174=100:100:1 (2) IPA (3) Drying at 60~80°C	15 min 2 min 60 min
57	Parylene-C deposition	Parylene-C 350nm	2 hours
58	Photolithography for parylene etching on release holes, electrode pad (14)	(1) Bake before coating 160°C (2) Spin-coat ip3100 with OAP surfactant (3) Pre-bake 110°C (4) Exposure (5) Developing with NMD-3, rinse with H ₂ O (6) Post-bake 110°C	90 sec 85.5 sec 90 sec 0.3 sec 160 sec 5 min
59	Parylene etching	O ₂ plasma 150W, O ₂ 40sccm, 10Pa	300 sec
60	Resist removal	(1) Remover PG 60°C (2) Remover PG (Ultrasonic cleaning, output level:100%) (3) IPA (4) DIW	5 min 2 min 2 min 5 min
61	Stealth dicing	ozawa5-P1~P3 recipe	
62	Sacrificial etching (Amorphous Si)	XeF ₂ 2.5 Torr , N ₂ 0 Torr、 30 sec	
63	Wire bonding		

Appendix B Process chart for cavity-sealed MEMS interferometer with gas reactive-layer

Table A2. Cavity-sealed MEMS interferometer with high surface stress sensitivity for gas sensing

1st wafer (4 inch)

No.	Step	Condition	Time
1	Spin-coating of surfactant	Tween 20, 1st 1000 rpm, 2nd 2000 rpm	5, 30 sec
2	Parylene-C deposition	Parylene-C 100 nm	2 hours

2nd wafer (4 inch)

No.	Step	Condition	Time
1	Photolithography for stepper mark (1)	(1) Bake before coating 160°C	90 sec
		(2) Spin-coat ip3100 with OAP surfactant	85.5 sec
		(3) Pre-bake 110°C	90 sec
		(4) Exposure	0.28 sec
		(5) Developing with NMD-3, rinse with H ₂ O	160 sec
		(6) Post-bake 120°C	5 min
2	Stepper mark etching	Si-RIE 10 Pa Parameter 6 CF ₄ :15 sccm [cc(cm ³)min]	5 min
3	Resist removal	(1) H ₂ SO ₄ :H ₂ O ₂ =1:3 boil	10 min
		(2) DIW	10 min
4	Photolithography for sensing area and aligner mark formation (2)	(1) Bake before coating 160°C	90 sec
		(2) Spin-coat ip3100 with OAP surfactant	85.5 sec
		(3) Pre-bake 110°C	90 sec
		(4) Exposure	0.28 sec
		(5) Developing with NMD-3, rinse with H ₂ O	160 sec
		(6) Post-bake 120°C	5 min

5	Bulk Si etching	Deep RIE, "honma-RIE_O ₂ _300W" recipe, Coil RF 300W, SF ₆ 130 sccm, C ₄ F ₈ 85 sccm	X cycle
6	Resist removal	(1) O ₂ ashing, RIE mode, RF 200W, O ₂ 40, CF ₄ 10 sccm (2) H ₂ SO ₄ :H ₂ O ₂ =3:1 boil (3) DIW	300 sec 15 min 10 min
7	Silane coupling treatment	(1) IPA:H ₂ O:A-174=100:100:1 (2) IPA (3) Drying at 60~80°C	15 min 2 min 60 min
8	Parylene-C deposition	Parylene-C 100 nm	2 hours
9	Photolithography for parylene etching on cavity pattern (3)	(1) Bake before coating 160°C (2) Spin-coat ip3100 with OAP surfactant (3) Pre-bake 110°C (4) Exposure (5) Developing with NMD-3, rinse with H ₂ O (6) Post-bake 120°C	90 sec 85.5 sec 90 sec 0.28 sec 160 sec 5 min
10	Parylene etching	O ₂ ashing, RIE mode, RF 150 W, O ₂ 40 sccm, 10 Pa	180 sec
11	Resist removal	(1) Acetone (2) IPA (3) DIW	10 min 2 min 5 min
12	Photolithography for dicing line formation (4)	(1) Bake before coating 160°C (2) Spin-coat ip3100 with OAP surfactant (3) Pre-bake 110°C (4) Exposure (5) Developing with NMD-3, rinse with H ₂ O (6) Post-bake 120°C	90 sec 85.5 sec 90 sec 0.28 sec 160 sec 5 min

13	Stealth dicing	ozawa5-P1~P3 recipe	
----	----------------	---------------------	--

Bonding process

No.	Step	Condition	Time
1	Parylene-C thermal bonding	Bake 160°C, Pressure 1.5 MPa, temperature rise rate 30°C/min, N ₂ 3L/min	10 min
2	Releasing from bonded wafer	(1) Immerse wafer in DIW (2) Dry	15 min
3	Spin-coating of gas-reactive film	(1) Bake before coating 110°C (2) Spin-coat PMMA (1st 500, 2nd 3000 rpm) (3) Bake 110°C	90 sec 5, 30 sec 60sec

Appendix C Process chart for cavity-sealed MEMS interferometer with a molecular imprinted polymer film

Table A3. Cavity-sealed MEMS interferometer with a molecular imprinted polymer film

1st wafer (4 inch)

No.	Step	Condition	Time
1	Spin-coating of surfactant	Tween 20, 1st 1000 rpm, 2nd 2000 rpm	5, 30 sec
2	Parylene-C deposition	Parylene-C 100 nm	2 hours
3	Shadow mask formation	OHP sheet, cut by laser	
4	Al electrode sputtering with shadow mask	Minimal sputtering device (1) Vacuum 1 Pa (2) Pre-sputtering (3) Sputtering emission current 50 mA, 3 Pa (4) Vacuum (5) Purge	2 min

2nd wafer (4 inch)

No.	Step	Condition	Time
1	Photolithography for stepper mark (1)	(1) Bake before coating 160°C (2) Spin-coat ip3100 with OAP surfactant (3) Pre-bake 110°C (4) Exposure (5) Developing with NMD-3, rinse with H ₂ O (6) Post-bake 120°C	90 sec 85.5 sec 90 sec 0.28 sec 160 sec 5 min
2	Stepper mark etching	Si-RIE 10 Pa Parameter 6 CF ₄ :15 sccm [cc(cm ³)min]	5 min

3	Resist removal	(1) H ₂ SO ₄ :H ₂ O ₂ =1:3 boil (2) DIW	10 min 10 min
4	Photolithography for sensing area and aligner mark formation (2)	(1) Bake before coating 160°C (2) Spin-coat ip3100 with OAP surfactant (3) Pre-bake 110°C (4) Exposure (5) Developing with NMD-3, rinse with H ₂ O (6) Post-bake 120°C	90 sec 85.5 sec 90 sec 0.28 sec 160 sec 5 min
5	Bulk Si etching	Deep RIE, "honma-RIE_O2_300W" recipe, Coil RF 300W, SF ₆ 130 sccm, C ₄ F ₈ 85 sccm	X cycle
6	Resist removal	(1) O ₂ ashing, RIE mode, RF 200W, O ₂ 40, CF ₄ 10 sccm (2) H ₂ SO ₄ :H ₂ O ₂ =3:1 boil (3) DIW	300 sec 15 min 10 min
7	Silane coupling treatment	(1) IPA:H ₂ O:A-174=100:100:1 (2) IPA (3) Drying at 60~80°C	15 min 2 min 60 min
8	Parylene-C deposition	Parylene-C 100 nm	2 hours
9	Photolithography for parylene etching on cavity pattern (3)	(1) Bake before coating 160°C (2) Spin-coat ip3100 with OAP surfactant (3) Pre-bake 110°C (4) Exposure (5) Developing with NMD-3, rinse with H ₂ O (6) Post-bake 120°C	90 sec 85.5 sec 90 sec 0.28 sec 160 sec 5 min
10	Parylene etching	O ₂ ashing, RIE mode, RF 150 W, O ₂ 40 sccm, 10 Pa	180 sec

11	Resist removal	(1) Acetone (2) IPA (3) DIW	10 min 2 min 5 min
12	Photolithography for dicing line formation (4)	(1) Bake before coating 160°C (2) Spin-coat ip3100 with OAP surfactant (3) Pre-bake 110°C (4) Exposure (5) Developing with NMD-3, rinse with H ₂ O (6) Post-bake 120°C	90 sec 85.5 sec 90 sec 0.28 sec 160 sec 5 min
13	Stealth dicing	ozawa5-P1~P3 recipe	

Dry transfer process

No.	Step	Condition	Time
1	Au/Parylene releasing	(1) Prepare carrier tape (5.5×5.5 cm), stick the tape on sputtered wafer (2) Prepare PTFE (2×3 cm), stick the tape (5×5 mm) on the PTFE and put diced chip on the tape (3) Shave parylene under the tape by tweezers (4) Immerse in DIW	
2	Dry transfer of Au/Parylene	(1) Put PTFE with chip on stage of dry transfer device (2) Fix released film to the stage of dry transfer device by carrier tape (3) Move up the stage (4) Bake 160°C	60 min

3	Polypyrrole formation by electrochemical polymerization	(1) Prepare KCl buffer (0.1 mM) (2) N ₂ blowing to KCl buffer (3) Add pyrrole (10 mM) and dopamine (1 mM) (4) Potential sweeping with 3 electrodes (working, reference, counter)	2 min X Cycle
---	---	--	----------------------

Appendix D Python program to smoothen spectra data

This program operates in the following steps.

1. Divide the spectra data of three sensors obtained by automatic measurement, and saves data as "01_sensor_1~3.csv".
2. Calculate the Q point (the steepest point of spectra) by differential, and save data as "02_differential_results1~3.csv".
3. Smooth the data by applying Fourier transform/inverse transform and low-pass filtering.
4. Draw the original and smoothed spectra, and save data as "03_Smoothing_sensor1~3_after_differential.csv".

```
import numpy as np
import matplotlib.pyplot as plt

# Input wavelength data
xaxis = np.loadtxt('wavelength_axis_T.csv', delimiter=',')
data1 = np.loadtxt('3spectra.csv', delimiter=',')

# Delete the wavelength data exists in the first line.
data1 = np.delete(data1, 0, 1)
dshape = data1.shape

# Define the number of measurement sensors as n
n = 3
sens_number = np.arange(n)
sens_array = np.tile(sens_number, int(dshape[1]/(n)))

# If the number of rows in the repeated array and the number of rows in the
original array are not enough, add the missing array [0,1,2...] to the end.
tarinai = data1.shape[1]-sens_array.shape[0]
add = np.arange(tarinai)
sens_array = np.append(sens_array, add)
```

```

# Add an array with a sensor number on line 0 to the original array.
data1 = np.insert(data1, 0, sens_array, axis=0)

# Generate arrays to store each sensor number according to the number of columns
in the original data.
temp_1 = np.zeros(data1.shape[0]).reshape(data1.shape[0],1)
temp_2 = np.zeros(data1.shape[0]).reshape(data1.shape[0],1)
temp_3 = np.zeros(data1.shape[0]).reshape(data1.shape[0],1)

# In the first row of the data1 array, extract the columns with 0,1,2,3,4,5 and add
them to the first row of the temp array.
for num in range(0, data1.shape[1], 1):
    if data1[0, num] == 0:
        temp_1 = np.insert(temp_1, 0, data1[0:,num], axis = 1)
    elif data1[0, num] == 1:
        temp_2 = np.insert(temp_2, 0, data1[0:,num], axis = 1)
    elif data1[0, num] == 2:
        temp_3 = np.insert(temp_3, 0, data1[0:,num], axis = 1)

# Save the data with the sensor number added to the first line of the original data.
np.savetxt('sensor_number.csv', data1, delimiter=',')

# Delete the data in the first row where the sensor number was added and in the
first column where it was first generated.
temp_1 = np.fliplr(temp_1)
temp_1 = np.delete(temp_1, 0, 0)
temp_1 = np.delete(temp_1, 0, 1)

temp_2 = np.fliplr(temp_2)
temp_2 = np.delete(temp_2, 0, 0)
temp_2 = np.delete(temp_2, 0, 1)

temp_3 = np.fliplr(temp_3)
temp_3 = np.delete(temp_3, 0, 0)

```

```

temp_3 = np.delete(temp_3, 0, 1)

temp_1 = np.insert(temp_1, 0, xaxis.T, axis=1)
temp_2 = np.insert(temp_2, 0, xaxis.T, axis=1)
temp_3 = np.insert(temp_3, 0, xaxis.T, axis=1)
np.savetxt('01_sensor_1.csv', temp_1, delimiter=',')
np.savetxt('01_sensor_2.csv', temp_2, delimiter=',')
np.savetxt('01_sensor_3.csv', temp_3, delimiter=',')

# Differentiation Program↓
xaxis = np.loadtxt('wavelength_axis_T.csv', delimiter=',')
data = np.loadtxt('01_sensor_1.csv', delimiter=',')
data2 = np.loadtxt('01_sensor_2.csv', delimiter=',')
data3 = np.loadtxt('01_sensor_3.csv', delimiter=',')

data = data.T
data = np.delete(data, 0, 0)
motodata = data

data2 = data2.T
data2 = np.delete(data2, 0, 0)
data3 = data3.T
data3 = np.delete(data3, 0, 0)

fig = plt.figure()

# Waveform before differentiation
ax1 = fig.add_subplot(1, 3, 1)
ax1.set_title("Original data")
ax1.set_xlabel("Wavelength (nm)")
ax1.set_ylabel("Reflectance (%)")
for num in range(0, 60, 12):
    ax1.plot(xaxis, motodata[num,:], label = "{0} min".format(num))
ax1.legend()

```

```

# First-order differentiation of data array = extract differences
data = np.diff(data, n = 1)
data2 = np.diff(data2, n = 1)
data3 = np.diff(data3, n = 1)

xshape = xaxis.shape
xaxis = np.delete(xaxis, xaxis[(xshape[0])-1])

# Waveform after differentiation
ax2 = fig.add_subplot(1, 3, 2)
ax2.set_title("Differential data")
ax2.set_xlabel("Wavelength (nm)")
ax2.set_ylabel("")
for num in range(0, 60, 12):
    ax2.plot(xaxis, data3[num,:], label = "{0} min".format(num))
ax2.legend()

data = np.insert(data, 0, xaxis, axis=0)
np.savetxt('02_differential_results1.csv', data.T, delimiter=',')
data2 = np.insert(data2, 0, xaxis, axis=0)
np.savetxt('02_differential_results2.csv', data2.T, delimiter=',')
data3 = np.insert(data3, 0, xaxis, axis=0)
np.savetxt('02_differential_results3.csv', data3.T, delimiter=',')

# Smoothing program↓
xaxis = np.loadtxt('wavelength_axis_T.csv', delimiter=',')
xshape = xaxis.shape
print(xaxis[(xshape[0])-1])
xaxis = np.delete(xaxis, xaxis[(xshape[0])-1])
data = np.insert(data, 0, xaxis, axis=0)
data2 = np.insert(data2, 0, xaxis, axis=0)
data3 = np.insert(data3, 0, xaxis, axis=0)
data = np.loadtxt('02_differential_results1.csv', delimiter=',')
data2 = np.loadtxt('02_differential_results2.csv', delimiter=',')
data3 = np.loadtxt('02_differential_results3.csv', delimiter=',')

```

```

# Transpose a matrix "data"
data = data.T
data2 = data2.T
data3 = data3.T
dshape = data.shape

# Delete the wavelength data exists in the first line.
data = np.delete(data, 0, 0)
data2 = np.delete(data2, 0, 0)
data3 = np.delete(data3, 0, 0)

# Define matrix before smoothing as "motodata" to compare before and after
smoothing waveform.
motodata = data
dshape = data.shape
# Merge arrays horizontally

# Generate a matrix with all zero data.
# Since the Fourier transform must be aligned with the amount of data to the nth
power of 2, if the amount of data is insufficient for 4096, generate an array with
all the missing data as 0 (dummy data generation).
data = np.hstack((data, np.zeros((dshape[0], 4096 - dshape[1]), dtype=np.float))
)
freqdata = np.fft.fft(data)
freqdata[:,10:] = 0
data2 = np.hstack((data2, np.zeros((data2.shape[0], 4096 - data2.shape[1]), dtype=np.float)))
freqdata2 = np.fft.fft(data2)
freqdata2[:,10:] = 0
data3 = np.hstack((data3, np.zeros((data3.shape[0], 4096 - data3.shape[1]), dtype=np.float)))
freqdata3 = np.fft.fft(data3)
freqdata3[:,10:] = 0

```

```

# Fast Inverse Fourier Transform
smoothed = np.fft.ifft(freqdata)
smoothed2 = np.fft.ifft(freqdata2)
smoothed3 = np.fft.ifft(freqdata3)

# Return only the real part after inverse Fourier transform (imaginary part is
truncated)
smoothed = np.real(smoothed)
smoothed2 = np.real(smoothed2)
smoothed3 = np.real(smoothed3)

# Delete dummy data generated when Fourier transform.
smoothed = np.delete(smoothed, np.s_[dshape[1]:4096], 1)
smoothed2 = np.delete(smoothed2, np.s_[dshape[1]:4096], 1)
smoothed3 = np.delete(smoothed3, np.s_[dshape[1]:4096], 1)

# Waveform after smoothing
ax3 = fig.add_subplot(1, 3, 3)
ax3.set_title("Smoothing")
ax3.set_xlabel("Wavelength (nm)")
ax3.set_ylabel("")
for num in range(0, 60, 12):
    ax3.plot(xaxis, smoothed[num,:], label = "{0} min".format(num))
ax3.legend()

plt.show() # Draw graph

# Insert wavelength data "xaxis" in an initial column
smoothed = np.insert(smoothed, 0, xaxis, axis=0)
smoothed2 = np.insert(smoothed2, 0, xaxis, axis=0)
smoothed3 = np.insert(smoothed3, 0, xaxis, axis=0)

np.savetxt('03_Smoothing_sensor1_after_differential.csv', smoothed.T, delimiter
=',')

```

```
np.savetxt('03_Smoothing_sensor2_after_differential.csv', smoothed2.T, delimiter=',')  
np.savetxt('03_Smoothing_sensor3_after_differential.csv', smoothed3.T, delimiter=',')
```

Appendix E Python program for the extraction of Q points from spectra data

This program operates in the following steps.

1. Input smoothed data "03_Smoothing_sensor1~3_after_differential.csv".
2. Calculate the time course of the Q point from the input data, and save data as "04_Peak_spectra_sensor1~3.csv".

```
import numpy as np
import matplotlib.pyplot as plt

data1 = np.loadtxt('03_Smoothing_sensor1_after_differential.csv', delimiter=',')
data2 = np.loadtxt('03_Smoothing_sensor2_after_differential.csv', delimiter=',')
data3 = np.loadtxt('03_Smoothing_sensor3_after_differential.csv', delimiter=',')

dshape = data1.shape
dshape2 = data2.shape
dshape3 = data3.shape

i = 0 # Variable parameter to count Q points
n = 18 # Number of Q points in the prior forecast

time_number_0 = np.zeros(n*2, dtype = float).reshape(n,-1) # Array to store Q
point 1
time_number_1 = np.zeros(n*2, dtype = float).reshape(n,-1) # Array to store Q
point 2
time_number_2 = np.zeros(n*2, dtype = float).reshape(n,-1) # Array to store Q
point 3

lists = list() # Array for temporary storage of Q point values
np.array(lists, dtype = float)
Q_point = np.zeros(0, dtype = int)
Q_point2 = np.zeros(0, dtype = int)
Q_point3 = np.zeros(0, dtype = int)
```

```

# Peak extraction of sensor 1
for hnum in range(1, dshape[1]-1, 1): # Scan horizontally
    for vnum in range(1, dshape[0]-1,1): # Scan vertically
        if data1[vnum, hnum] < data1[vnum+1, hnum] and data1[vnum, hnum] < data1[vnum-1, hnum]: # Extraction of spectral valleys
            lists.append(data1[vnum,0]) # Add the wavelength of the valley of the spectrum in an initial column
            i = i + 1 # Record the number of Q points.
            Q_point = np.insert(Q_point, 0, i, axis = 0) # Store the number of Q-points in an array
            if len(lists) < n: # If the number of arrays is less than the number of Q points, add 0 to the end of the array to adjust the number of arrays.
                for num in range(0, n-len(lists),1):
                    lists.append(0)
            time_number_0 = np.insert(time_number_0, 0, lists, axis = 1) # Add the value of Q point to column 0.
            print(time_number_0)
            lists[:] = [] # Delete the contents of the array that stores the Q points
            i = 0
time_number_0 = np.flipud(time_number_0) # Flip the array upside down
time_number_0 = np.fliplr(time_number_0) # Flip the array left or right
time_number_0 = np.delete(time_number_0, 0, 1) # Delete all columns with zero elements in columns 0 and 1 of the array.
time_number_0 = np.delete(time_number_0, 0, 1)

# Peak extraction of sensor 2
for hnum in range(1, dshape2[1]-1, 1):
    for vnum in range(1, dshape2[0]-1,1):
        if data2[vnum, hnum] < data2[vnum+1, hnum] and data2[vnum, hnum] < data2[vnum-1, hnum]:
            lists.append(data2[vnum,0])
            Q_point2 = np.insert(Q_point2, 0, i, axis = 0)
            if len(lists) < n:
                for num in range(0, n-len(lists),1):
                    lists.append(0)

```

```

time_number_1 = np.insert(time_number_1, 0, lists, axis = 1)
print(time_number_1)
lists[:] = []
i = 0
time_number_1 = np.flipud(time_number_1)
time_number_1 = np.fliplr(time_number_1)
time_number_1 = np.delete(time_number_1, 0, 1)
time_number_1 = np.delete(time_number_1, 0, 1)

# Peak extraction of sensor 3
for hnum in range(1, dshape3[1]-1, 1):
    for vnum in range(1, dshape3[0]-1,1):
        if data3[vnum, hnum] < data3[vnum+1, hnum] and data3[vnum, hnum] < da
ta3[vnum-1, hnum]:
            lists.append(data3[vnum,0])
            i = i + 1
Q_point3 = np.insert(Q_point3, 0, i, axis = 0)
if len(lists) < n:
    for num in range(0, n-len(lists),1):
        lists.append(0)
time_number_2 = np.insert(time_number_2, 0, lists, axis = 1)
print(time_number_2)
lists[:] = []
i = 0

time_number_2 = np.flipud(time_number_2)
time_number_2 = np.fliplr(time_number_2)
time_number_2 = np.delete(time_number_2, 0, 1)
time_number_2 = np.delete(time_number_2, 0, 1)

# Delete useless arrays caused by the difference between the number of Q points
in the set value and in the actual measurement.
for num in range(0, n-max(Q_point)+1,1):
    time_number_0 = np.delete(time_number_0, 0, 0)
    time_number_1 = np.delete(time_number_1, 0, 0)

```

```
time_number_2 = np.delete(time_number_2, 0, 0)

# Add a time term in column 0, depending on the number of columns in the matrix
time = time_number_0.shape[1]
time_number_0 = np.insert(time_number_0,0,np.arange(time),axis = 0)
time = time_number_1.shape[1]
time_number_1 = np.insert(time_number_1,0,np.arange(time),axis = 0)
time = time_number_2.shape[1]
time_number_2 = np.insert(time_number_2,0,np.arange(time),axis = 0)

np.savetxt('04_Peak_spectra_sensor1.csv', time_number_0, delimiter=',')
np.savetxt('04_Peak_spectra_sensor2.csv', time_number_1, delimiter=',')
np.savetxt('04_Peak_spectra_sensor3.csv', time_number_2, delimiter=',')
```

Appendix F Python program for smoothing Raman spectrum data

This program operates in the following steps.

1. Input obtained Raman spectrum data "Spectra.csv" and wavenumber data "wavelength_axis_T.csv".
2. Smooth input Raman data by applying the Savitzky–Golay filter.
3. Draw the original and smoothed Raman spectra, and save data as "smoothing.csv".

```
import numpy as np
import matplotlib.pyplot as plt
from scipy.signal import savgol_filter

# Input wavenumber data
xaxis = np.loadtxt('wavelength_axis_T.csv', delimiter=',')
data = np.loadtxt('Spectra.csv', delimiter=',')

# Transpose a matrix "data"
data = data.T

# Delete the wavenumber data exists in the first line.
data = np.delete(data, 0, 0)

# Define matrix before smoothing as "motodata" to compare before and after
smoothing waveform.
motodata = data

# Moving standard deviation = savgol_filter (input data, the number of
approximate data, index of polynomial, mode="wrap")
smoothed = savgol_filter(data, 121,1, mode="wrap")

# Figure drawing declaration
fig = plt.figure()
```

```
ax1 = fig.add_subplot(1, 2, 1) # Set the left side when drawing in 1 row 2 columns.
ax1.set_title("Original data") # Graph title
ax1.set_xlabel("Raman shift (cm-1)") # X axis label
ax1.set_ylabel("Intensity (a.u.)") # Y axis label
ax1.plot(xaxis, motodata[0])
ax1.legend() # Draw a legend in a graph window

ax2 = fig.add_subplot(1, 2, 2) # Set the right side when drawing in 1 row 2
columns.
ax2.set_title("Smoothing")
ax2.set_xlabel("Raman shift (cm-1)")
ax2.set_ylabel("Intensity (a.u.)")
ax2.plot(xaxis, smoothed[0])
ax2.legend()

plt.show() # Draw graph

# Insert wavenumber data "xaxis" in an initial column
smoothed = np.insert(smoothed, 0, xaxis, axis=0)
np.savetxt('smoothing.csv', smoothed.T, delimiter=',')
```